Fundamental Ways to Probe Gravitational Waves Across Its Spectrum and Propagation

Thesis by
Rhondale Tso

In Partial Fulfillment of the Requirements for the
Degree of
Doctor of Philosophy

CALIFORNIA INSTITUTE OF TECHNOLOGY
Pasadena, California

2022
Defended May 09, 2022

Rhondale Tso
ORCID: 0000-0003-4464-0117

ACKNOWLEDGEMENTS

This work was supported by the National Science Foundation Graduate Research Fellowship Program under Grant No. DGE-1144469, the Ford Foundation Predoctoral Fellowship, and the Gates Foundation. Further thanks provided to the Niels Bohr Institute for its hospitality where part of this work was completed, and acknowledgement to the Kavli Foundation and the DNRF for supporting the 2017 Kavli Summer Program. Further support was provided by the Simons Foundation (Award Number 568762), the Brinson Foundation, and the National Science Foundation (Grants PHY–2011968, PHY–2011961 and PHY–1836809).

Part of the computations were performed on Caltech cluster *Wheeler*, supported by the Sherman Fairchild Foundation and Caltech. Part of the computations were conducted in the Resnick High Performance Computing Center, a facility supported by Resnick Sustainability Institute at the California Institute of Technology.

Additional thanks to Nicolàs Yunes, Scott Perkins, Jose Maria Ezquiaga, Elisa Maggiore, Emanuele Berti, Jonathan Blackman, Neil Cornish, Matthew Evans, Daniel D'Orazio, Matthew Giesler, Zoltan Haiman, Evan Hall, Kevin Kuns, Lionel London, Belinda Pang, Alberto Sesana, Ulrich Sperhake, Salvatore Vitale, T.G.F. Li, Walter D. Pozzo, Kent Yagi, Alan Weinstein, and Rana Adhikari for fruitful discussions and advice.

Further thanks to Yanbei Chen, Yijun (Ali) Wang, Davide Gerosa, Daniel Holz, Jonathan Gair, Joey S. Key, Maximiliano Isi, Leo C. Stein, and Michele Zanolin for collaboration on portions of this thesis.

A special thanks to research advisors on research projects prior to graduate school: Quentin Bailey, Michele Zanolin, V.A. Kosteleckỳ, Janna Levin, and Robert Wald.

Finally special thanks to my PhD advisor Yanbei Chen and members of my defense committee that have included Alan Weinstein, Rana Adhikari, and Mark Wise.

ABSTRACT

In 2015, the detection of gravitational waves (GWs) from merging black holes by the LIGO Scientific Collaboration and the VIRGO Collaboration opened a new era of observational astronomy. This thesis covers a range of topics on how to test the general theory of relativity using current and future GW detectors — both ground- and space-based. Starting from general principles, in Chapter 2, we survey how well the so-called parameterized post-Einstein parameters for binary black hole GWs can be constrained by multi-band GW detection, which employs both ground-based detectors (including Einstein Telescope and Cosmic Explorer) and space-based detectors (including the Laser Interferometer Space Antenna and deci-Hertz detectors).

In Chapter 3, we address the limitations of the Fisher Information Matrix approach in testing relativity. Chapter 4 proposes a novel experimental strategy for multi-band GW observation. More specifically, the detection of a stellar-mass binary from the Laser Interferometer Space Antenna can provide forewarning for ground-based observations, e.g., by third-generation detectors. Adjusting optical configurations of ground-based detectors targeting this particular binary can significantly improving our accuracy in testing the "no-hair theorem" of black holes. In Chapter 5, we establish a systematic framework that describes how the propagation of GWs can differ from predictions of general relativity, incorporating both dispersion and birefringence. In Chapter 6, we focus the specific example of massive gravitons and show how the so-called Vainshtein screening of the graviton's mass, by the host galaxy of the source, the Milky way galaxy — and galaxies in between — can be extracted from an ensemble of signals.

PUBLISHED CONTENT AND CONTRIBUTIONS

[1] R. Tso, Y. Wang, and Y. Chen, To Be Published (2022),
Title: *Probing screened massive gravitons with gravitational wave observations*.
Results discussed in Chapter 5 and 6.
R.T. participated in the conception of the project, solved and analyzed equations, prepared and analyzed data, and helped write the manuscript.

[2] B. P. Abbott *et al.* (LIGO Collaboration), Physical Review Letters **123**, 011102, `10.1103/PhysRevLett.123.011102` (2019),
Title: *Tests of General Relativity with GW170817*.
Preprint: `https://arxiv.org/abs/1811.00364`.
Results discussed in Chapter 7.
R.T. participated in the conception of the project, analyzed data, and helped write the manuscript.

[3] R. Tso, D. Gerosa, and Y. Chen, Physical Review D **99**, 124043, `10.1103/PhysRevD.99.124043` (2019),
Title: *Optimizing LIGO with LISA forewarnings to improve black-hole spectroscopy*.
Preprint: `https://arxiv.org/abs/1807.00075`.
Results in Chapter 4.
R.T. participated in the conception of the project, solved and analyzed equations, prepared and analyzed data, and helped write the manuscript.

[4] R. Tso, M. Isi, Y. Chen, and L. Stein, arXiv e-prints, arXiv:1608.01284 (2016),
Title: *Modeling the Dispersion and Polarization Content of Gravitational Waves for Tests of General Relativity*.
Preprint: `https://arxiv.org/abs/1608.01284`.
Results discussed in Chapter 5.
R.T. participated in the conception of the project, solved and analyzed equations, and helped write the manuscript.

[5] R. Tso and M. Zanolin, PRD **93**, 124033, `10.1103/PhysRevD.93.124033` (2016),
Title: *Measuring violations of general relativity from single gravitational wave detection by nonspinning binary systems: Higher-order asymptotic analysis*.
Preprint: `https://arxiv.org/abs/1509.02248`.
Results discussed in Chapter 3.
R.T. participated in the conception of the project, solved and analyzed equations, prepared and analyzed data, and helped write the manuscript.

TABLE OF CONTENTS

LIST OF ILLUSTRATIONS

LIST OF TABLES

Chapter 1

INTRODUCTION

For over a century, general relativity (GR) has been successful at characterizing gravity. Einstein's theory first accounted for Mercury's anomalous orbital precession, and later led to the famous 1919 light-bending confirmation, measured by Dyson, Eddington, and Davidson [1]. As a theory of spacetime, GR succeeded in correcting Newtonian dynamics wherever the pre-GR theory failed, in regions of strong gravity. As with every subject in physics, gravity has a theoretical component to complement its experimental foundation. Technological advances half a century after GR's discovery has allowed some of the most stringent experiments and observations to determine its validity as an accurate description of gravity. These tests were designed to probe proposed corrections to this already very successful theory of spacetime. Once observational techniques advanced, gravitational field strengths far greater than those of the solar system were examined [2]. The Hulse-Taylor binary pulsar [3] and observations on cosmological scales [4] allowed even further exploration of GR. Binary pulsar tests relied on the nature of the binary's dynamics emitting radiation in the form of gravitational waves (GWs). Predicted by Einstein himself, the essence of GWs rests on the idea that propagating deformations of spacetime, produced from accelerating masses, carry energy away from their sources [5]. As compact objects in a binary orbit, spin, and merge, GWs emanate from their motions. This indirect detection provided the most promising evidence for direct confirmation of GR. To date, GR remains the most successful theory describing gravitation. From incorporating corrections through top-down approaches of some fundamental, or full/exact theory, to a bottom-up approach, with the notion that nature has some separation of scales, GR has been triumphant.

Today the Laser Interferometer Gravitational-wave Observatory (LIGO) [6] and Virgo [7] have labored towards some of the first direct detections of GW transients from black hole (BH) binaries, neutron star (NS) binaries, and BH-NS binaries [8–11]. These observations have allowed the testing of GR in its most extreme environments, which had never been probed before: compact binaries coalescing with orbital velocities comparable to the speed of light [12–15]. The space-based Laser Interferometer Space Antenna (LISA) [16, 17] mission has similar goals but will probe the low-frequency regime of massive BH inspirals and extreme mass ratio binaries. These low-frequency GW sources are in contrast to the high-frequency, stellar-mass BH binaries LIGO can detect. As ground-based GW detectors are upgraded, from LIGO-Virgo observatories to third-generation detectors like Cosmic Explorer (CE) [18], a new era of precision tests of GR at cosmological scales will commence. Combined with LISA, these third-generation detectors will probe GR at scales never before investigated.

Up until now, LIGO's observations have been in agreement with GR, continuing its success after achieving its status as the most favored theory to date [2, 12–15]. From a theory perspective, an area of contention resides in the inability of GR to integrate with the quantum world. From an observational angle, GR cannot explain the late time acceleration of the universe and the rotation curves of galaxies, without adding an unnaturally small cosmological constant or relying on the existence of dark matter. Areas where GR could breakdown include the strong-field regime and very large scales. Study of BHs and their dynamics will probe the former. The latter can be investigated through the propagation of GWs produced by orbiting BHs. Advances are needed in both areas to prepare for third-generation ground-based detectors and space detectors. Developing models for cosmological scale observations and advances in numerical methods are suited to address these topics.

This thesis resides at the boundary of theory and observation, to test various theories of gravity, beyond that of GR, through GW observations. LIGO's first observation run supplied two signals from the inspiral of two binary black hole pairs, gravitational wave events given the names GW150914 and GW151226 (numbers encoding the date of detection UTC time). Each detection gives signals at a scale where GR is still treated classically, yet allows the most relativistic regimes to be probed. Further runs have supplied even more detections, including GW170817 which is the first binary neutron star event, BHs more massive than originally thought, and potentially BH-NS systems. Combining all present and future detections will provide a wealth of information about how black holes behave, the nature of gravitational waves, and astrophysics. Contained within this information are constraints compatible with theories beyond GR.

1.1 Primer on Gravitational Waves

To start, we work in the context of General Relativity, where plenty of resources are available to provide a suitable introduction to the topic [19]. Here we will concentrate primarily on looking at the generation process and useful expressions while using the notation of Ref. [19, 20].

Linearized Einstein Equations

In the linear theory of a weak gravitational field,

$$g_{\alpha\beta} \approx \eta_{\alpha\beta} + h_{\alpha\beta}, \tag{1.1}$$

where $(-,+,+,+)$ is the signature for flat spacetime $\eta_{\alpha\beta}$ and small fluctuations $h_{\alpha\beta}$ ($|h_{\alpha\beta}| \ll 1$). The Riemann tensor $R_{\alpha\beta\mu\nu}$ to leading order in $h_{\alpha\beta}$ is

$$\begin{aligned} R^{\alpha}{}_{\beta\mu\nu} &\approx \Gamma^{\alpha}_{\beta\nu,\mu} - \Gamma^{\alpha}_{\beta\mu,\nu} \\ &= \frac{1}{2}\eta^{\alpha\lambda}\left(h_{\lambda\nu,\beta\mu} + h_{\beta\mu,\lambda\nu} - h_{\beta\nu,\lambda\mu} - h_{\lambda\mu,\beta\nu}\right). \end{aligned} \tag{1.2}$$

From this, the Ricci tensor follows,

$$R_{\beta\nu} = R^{\alpha}{}_{\beta\alpha\nu}. \tag{1.3}$$

Note that in this notation, $h_{\lambda\nu,\beta} = \partial_\beta h_{\lambda\nu}$ so that $h_{\lambda\nu,\beta\mu} = \partial_\mu\partial_\beta h_{\lambda\nu}$. This notation implies $h_{\beta\nu,\alpha}{}^{,\alpha} = \Box h_{\beta\nu}$ while $h = h^{\alpha}{}_{\alpha}$ is the trace. Raising and lowering is done to linear order with $\eta_{\alpha\beta}$ and $\eta^{\alpha\beta}$, thus $\Box = \eta^{\alpha\beta}\partial_\alpha\partial_\beta = \partial^\alpha\partial_\alpha$. This allows the compact expression of the Ricci tensor to be,

$$R_{\beta\nu} = \frac{1}{2}\left(\bar{h}^{\alpha}{}_{\nu,\alpha\beta} + \bar{h}^{\alpha}{}_{\beta,\alpha\nu} - \Box h_{\beta\nu}\right) \tag{1.4}$$

where $\bar{h}^{\alpha}{}_{\beta} = h^{\alpha}{}_{\beta} - h\delta^{\alpha}_{\beta}/2$ for Kronecker delta δ^{α}_{β}.

The above decomposition of $g_{\alpha\beta}$ is not unique. The coordinate system x^α can always be changed by a small vector $\xi^\alpha(x^\mu)$ of the same order as $h_{\alpha\beta}$: $\tilde{x}^\alpha = x^\alpha + \xi^\alpha$. Under such a coordinate change, the metric becomes $\tilde{g}_{\alpha\beta} = \eta_{\alpha\beta} + \tilde{h}_{\alpha\beta}$. Considering transformation of $\tilde{g}^{\alpha\beta}(\tilde{x}^\mu)$ in the new coordinates and a Taylor expansion of $\tilde{g}^{\alpha\beta}(x^\mu)$ in the old coordinates, it can be shown (to leading order) that the new metric can be expressed as,

$$\tilde{g}^{\alpha\beta}(x^\mu) = g^{\alpha\beta}(x^\mu) + \xi^{\alpha}{}_{,\mu}g^{\mu\beta} + \xi^{\beta}{}_{,\nu}g^{\alpha\nu} - \xi^{\mu}g^{\alpha\beta}{}_{,\mu} \tag{1.5}$$

Using the identity,

$$\xi^{\lambda}g^{\mu\nu}{}_{;\lambda} = 0, \tag{1.6}$$

the general transformation of the metric under a small transfromation ξ^μ is,

$$\tilde{g}^{\alpha\beta}(x^\mu) = g^{\alpha\beta}(x^\mu) + \xi^{\mu;\nu} + \xi^{\nu;\mu} \tag{1.7}$$

to linear order (semi-colons represent covariant derivatives). For the small fluctuations $|h_{\alpha\beta}| \ll 1$,

$$\tilde{h}^{\alpha\beta}(x^{\mu}) = h^{\alpha\beta}(x^{\mu}) + \xi^{\mu,\nu} + \xi^{\nu,\mu}, \tag{1.8}$$

where the covariant derivatives are dropped due to linear-order approximations. Here $\xi^{\mu}(x^{\alpha})$ are four arbitrary functions of the same order as $h_{\alpha\beta}$. They can be chosen to satisfy four (gauge) conditions imposed on $\tilde{h}^{\alpha\beta}$. The expression for the Ricci tensor greatly simplifies if we choose the following four Lorentz gauge conditions,

$$\bar{h}^{\alpha}{}_{\beta,\alpha} = 0 \tag{1.9}$$

which allows $R_{\beta\nu} = -\Box h_{\beta\nu}/2$. Note that this gauge does not completely specify $h^{\alpha\beta}$. Choosing such a gauge condition and making the transformation to $\tilde{h}^{\alpha\beta}$ implies that ξ^{α} can be chosen so that $\bar{\tilde{h}}^{\alpha\beta}{}_{,\alpha} = (\tilde{h}^{\alpha\beta} - \eta^{\alpha\beta}\tilde{h})_{,\alpha} = 0$. Expanding this expression results in the additional requirement,

$$\Box\xi^{\alpha} = 0. \tag{1.10}$$

For now, we will shortly discuss gravitational waves in a vacuum,

$$\begin{aligned} R_{\alpha\beta} &= 0 \\ \Box h_{\alpha\beta} &= 0. \end{aligned} \tag{1.11}$$

Solutions for planes waves propagating in the positive z-direction have the form,

$$h_{\alpha\beta} = h_{\alpha\beta}(t - z) \tag{1.12}$$

where we use $c = 1$. Using the Lorentz gauge and the wave equation above the following expression must be satisfied: $\bar{h}^{0\beta} - \bar{h}^{3\beta} =$ constant. Recall the condition of $\Box\xi^{\alpha} = 0$. Any such ξ^{α} can be chosen, so we can do arbitrary transformations within the class of solutions to the wave equation. Here four more conditions can be chosen such that $\Box\bar{h}_{\alpha\beta} = 0$. These are,

$$\begin{aligned} \bar{h}^{0i} &= 0 \\ \bar{h}^{11} + \bar{h}^{22} &= 0 \end{aligned} \tag{1.13}$$

for the wave propagating in the z-direction. This is called the transverse ($h^{3\beta} = 0$) and traceless ($h = -\bar{h} = 0$), i.e., transverse-traceless (TT) gauge. Non-zero components are in the xy-plane.

Effect of Gravitational Waves on Matter

Now let us consider two freely falling test particles separated by a vector $2\vec{S}$. The distance (metric) between the two particles changes as the wave passes between them due to tidal gravity. Considering the geodesic deviation equation, the observed acceleration (in orthonormal tetrad) is

$$\begin{aligned} \partial_t^2 S^\mu &= R^\mu{}_{\nu\rho\sigma} u^\nu u^\rho S^\sigma \\ &= R^\mu{}_{00\nu} S^\nu \end{aligned} \tag{1.14}$$

where four-vector $u^\mu = (1, 0, 0, 0)$ is used for the slow motion $v \ll 1$ of particles experiencing a weak fluctuation. In the chosen gauge, S^μ is purely spatial, and

$$\partial_t^2 S_\mu = \frac{1}{2}\partial_t^2 h_{\mu\nu} S^\nu \tag{1.15}$$

Consider a periodic gravitational wave with angular frequency ω, and using δS_μ to denote the change in separation due to gravitational waves, we have,

$$-\omega^2 \delta S_\mu \approx -\frac{1}{2}\omega^2 h_{\mu\nu} S^\nu \tag{1.16}$$

where $h_{\mu\nu}\delta S^\nu$ is neglected to leading order. Recall that in the above TT-gauge, $h_{11} = -h_{22}$ and $h_{12} = h_{21}$ are the only non-zero components. Conveniently defining $h_+ \equiv h_{11}$ and $h_\times \equiv h_{12}$ leads to,

$$\begin{aligned} \delta S_1 &= \frac{1}{2}\left(h_+ S_1 + h_\times S_2\right) \\ \delta S_2 &= \frac{1}{2}\left(h_\times S_1 - h_+ S_2\right). \end{aligned} \tag{1.17}$$

Note that under a coordinate rotation, the "×" polarization is just the "+" polarization rotated by $\pi/4$. See figure 1.1 for a depiction of these polarizations.

Generation of Gravitational Waves

Using the linear expression for the Ricci tensor in terms of $h_{\alpha\beta}$ and the definition of $\bar{h}_{\alpha\beta}$, one can express the Einstein tensor $G_{\alpha\beta}$ in terms of $\bar{h}_{\alpha\beta}$. Using the Lorenz gauge condition, this is simply $G_{\alpha\beta} = -\Box\bar{h}_{\alpha\beta}/2$, which results in,

$$\Box\bar{h}_{\alpha\beta} = -16\pi T_{\alpha\beta} \tag{1.18}$$

for stress-energy tensor $T_{\alpha\beta}$. Using the Green function,

$$G\left(|\vec{r} - \vec{r}'|, t - t'\right) = \frac{\delta\left(|\vec{r} - \vec{r}'| - (t - t')\right)\Theta(t - t')}{4\pi|\vec{r} - \vec{r}'|} \tag{1.19}$$

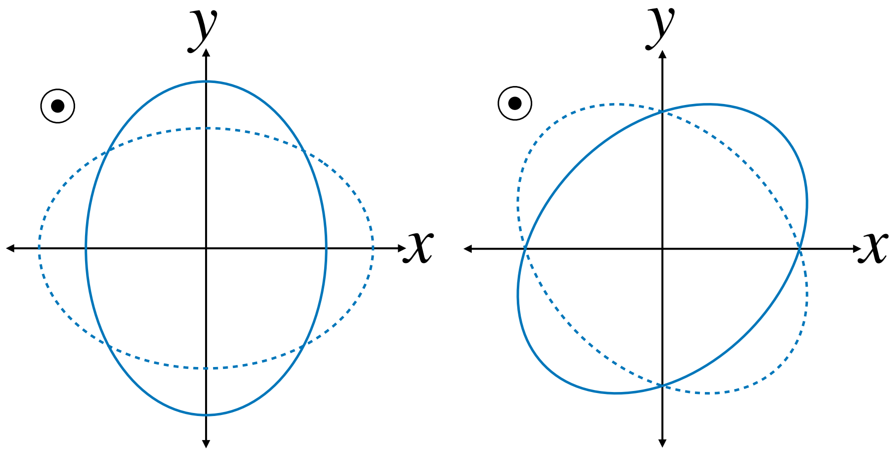

Figure 1.1: Polarization of gravitational waves. Left is "+" polarization and right is "×" polarization, inclined to each other at $\pi/4$. This represents a GW being spin-2, where a spin-S particle is invariant under $2\pi/S$ rotations and has two orthogonal states inclined at $\pi/2S$. The GW propagates along the positive z-axis and the polarizations are transverse.

for solution of the wave equation with source $\delta(\vec{r}')$, then the solution for given $T_{\alpha\beta}(t', \vec{r}')$ is

$$\bar{h}_{\alpha\beta}(t, \vec{r}) = 4 \int d^3\vec{r}' \, \frac{T_{\alpha\beta}\left(t - |\vec{r} - \vec{r}'|, \vec{r}'\right)}{|\vec{r} - \vec{r}'|}. \tag{1.20}$$

We can consider an oscillating stress-energy tensor,

$$T_{\alpha\beta}(t, \vec{r}) = a_{\alpha\beta}(\vec{r}) e^{-i\omega t}. \tag{1.21}$$

A further assumption that matter moves slowly in this region (i.e., stress-energy is non-zero in a region $\ll 1/\omega$) can be made. This results in,

$$\bar{h}_{\alpha\beta} \approx \frac{4e^{i\omega r}}{r} \int d^3\vec{r}' \, T_{\alpha\beta} \tag{1.22}$$

where $r \gg r'$. It is possible to express the oscillating $\int d^3\vec{r}' \, T_{ik}$ in terms of integrals of T_{00} using $T^{\mu\nu}{}_{,\mu} = 0$. This is done by assuming a small $T^{\mu\nu}$ or gravitational field and approximating the spacetime as flat. Here $T^{\mu\nu}{}_{,\mu} = i\omega T^{0\nu} + \partial_l T^{l\nu} = 0$ implies $\partial_l T^{l\nu} = -i\omega T^{0\nu}$ and expanding the following results in,

$$\begin{aligned} \int d^3\vec{r}' \, T^{ik} &= \int d^3\vec{r}' \, \partial_l \left(x^i T^{lk}\right) - \int d^3\vec{r}' \, x^i \partial_l T^{lk} \\ &= i\omega \int d^3\vec{r}' \, x^i T^{0k} \end{aligned} \tag{1.23}$$

where above the first time vanishes by Gauss's theorem and the second term comes from $T^{\mu\nu}{}_{,\mu} = 0$. Note that $\int d^3\vec{r}'\, T^{ik}$ is symmetric, thus so is $\int d^3\vec{r}'\, x^i T^{0k}$. Using additional manipulation along with Gauss's theorem again results in,

$$\int d^3\vec{r}'\, x^i T^{0k} = \frac{i\omega}{2} \int d^3\vec{r}'\, x^i x^k T^{00}. \tag{1.24}$$

Ultimately this leads to

$$\int d^3\vec{r}'\, T^{ij} = -\frac{\omega^2}{2} I^{ij} \tag{1.25}$$

where $I^{ij} = \int d^3\vec{r}'\, x^i x^j T^{00}$. The solution is then

$$\bar{h}^{ij} = -\omega^2 \frac{2e^{i\omega r}}{r} I^{ij} \tag{1.26}$$

which is true for any Fourier mode ω of a general time-dependent source. The inverse Fourier transform provides

$$\bar{h}^{ij} = \frac{2}{r} \ddot{I}^{ij}. \tag{1.27}$$

Note that $\bar{h}^{0\alpha}$ can be found from the gauge condition: $\bar{h}^{0\alpha} = -i\partial_l \bar{h}^{l\alpha}/\omega$. In the TT-gauge, I^{ij} can be replaced by its TT-part,

$$I_{ij}^{\mathrm{TT}} = \left(P^k{}_i P^l{}_j - \frac{1}{2} P_{ij} P^{kl} \right) I_{kl} \tag{1.28}$$

where $P_{ij} = \delta_{ij} - n_j n_j$ and n_i is the unit vector in the wave direction.

1.2 Gravitational Wave Signal

Predicted by General Relativity (GR), the essence of gravitational waves (GWs) rests on the idea that propagating deformations of spacetime, produced from accelerating masses, carry energy away from their sources. Our main focus will be on GWs emanating from binary systems, although plenty of other sources give off GWs at a potentially detectable level (e.g., supernovae bursts, rotating neutron stars, etc). As of now binaries have been the only detected source of GWs. In the remainder of this chapter units of G and c are returned for concreteness.

Decaying Orbit Basics

In Newtonian physics, the energy and angular momentum of a binary system are conserved, and two bodies in a Keplerian motion will perpetually orbit each other. As we had described in Sec. 1.1, in general relativity, an accelerating matter distribution sources gravitational waves, carrying away energy and angular momentum. The waveform is describable by the quadrupole formula mentioned above, while the power radiated can be computed by integrating over all emission angles, as described in details in Ref. [20]. The emission of GWs causes the separation between the two rotating bodies to decrease. To describe this scenario we have the energy balance equation,

$$\dot{E}_{\mathrm{orbital}} = -P \tag{1.29}$$

Assuming a circular orbit and angle averaging the power radiated comes out to,

$$P = \frac{32}{5}\frac{G\eta^{4/5}\mathcal{M}^2 r^4\omega^6}{c^5} \tag{1.30}$$

To leading order for a circular orbit (no eccentricity), $E_{\mathrm{orbital}} = -Gm_1m_2/(2r)$ and $\omega^2 = GM/r^3$. This means $\dot{r} = -(2/3)(r\omega)(\dot{\omega}/\omega^2)$ which is decreasing. If we assume $\dot{\omega}/\omega^2 \ll 1$ (the radial decay is much slower than the orbital rotation) then the orbit can be treated as a slowly decaying *quasi-circular* orbit. The radial decay has been shown to be,

$$r(t) = \left(r_0 - \frac{256}{5}\frac{G^3\eta^{-4/5}\mathcal{M}^3}{c^5}t\right)^{1/4} \tag{1.31}$$

with r_0 being the initial radial separation. The point at which $r(t_c) = 0$ is when the binaries have coalesced and that time is labeled as coalescence time t_c which can be solved from the above to be,

$$t_c = \frac{5}{256}\frac{r_0^4 c^5}{G^3\eta^{-4/5}\mathcal{M}^3} \tag{1.32}$$

Furthermore if we define $f_{\mathrm{GW}} = 2\omega$ (the GW frequency is twice the orbital frequency) then from the energy balance equation we get how the frequency evolves as a function of time,

$$\dot{f}_{\mathrm{GW}} = \frac{96}{5}\pi^{8/3}\left(\frac{G\mathcal{M}}{c^3}\right)^{5/3} f_{\mathrm{GW}}^{11/3} \tag{1.33}$$

Integrating this from some time t up to coalescences t_c and solving for f_{GW} results in,

$$f_{\mathrm{GW}} = \left(\frac{5}{256}\right)^{3/8} \pi^{-1}\left(\frac{G\mathcal{M}}{c^3}\right)^{-5/8} (t_c - t)^{-3/8} \tag{1.34}$$

This provides a frequency starting point given some time prior to coalescences. For example if we want to know the “start” frequency of a long-lived binary days, months, or years prior to merging we can just specify $\tau = t_c - t$. For example a GW150914-like system with masses $m_1 = 36M_\odot$ and $m_2 = 29M_\odot$ at $\tau = 4$ years (or 1.261×10^8 seconds) prior to merging will be at $f_{\rm GW} = 1.4 \times 10^{-2}$ [Hz]. This is in the centihertz range and will evolve over the years into the decihertz before merging in LIGO's bandwidth. Note that at large distances redshift factor z is important in distinguishing source vs. observer frames. This translates as,

$$\begin{aligned} t_{\rm obs} &= (1+z)t_{\rm source} \\ f_{\rm obs} &= \frac{f_{\rm source}}{(1+z)} \\ \lambda_{\rm obs} &= (1+z)\lambda_{\rm source} \end{aligned} \tag{1.35}$$

Inspiral Post-Newtonian Waveform

Analysis of a binary inspiral is primarily accomplished through a combination of analytic, semi-analytic, and numerical methods in solving the dynamical equations of GR. The predominant semi-analytic approach in the inspiral regime is the Post-Newtonian (PN) formalism. This is an approximative method which ultimately surfaces as the sequential appending of corrections to conventional Newtonian dynamics. Although successful in describing the inspiral phase of a binary, this approximation breaks down as merging is approached, where orbital velocities approach the speed of light and spacetime curvature increases rapidly. That is when an approximate cutoff frequency $f_{\rm cut}$ is introduced, generally this is,

$$f_{\rm cut} = \frac{1}{12\pi\sqrt{6}}\frac{c^3}{G(m_1+m_2)} \tag{1.36}$$

This is set by approximately mapping the binary motion to a point particle orbiting a Schwarzschild black hole, and taking the Inner-most Stable Circular Orbit (ISC) of the Schwarzschild as the end of the inspiral.

In this thesis, we shall only consider quasi-circular orbits, since eccentric orbits usually circularize before their orbital frequency enters the detection band of ground-based detectors. Up to Post-Newtonian (PN) Order 2.0 in the phase of the waveform and leading order in the amplitude [1] the inspiral in the stationary phase approximation

[1] Considering higher-order PN terms in the amplitude will require higher harmonics which makes the calculation much more complicated but to leading order is fine for us.

can be approximated as:

$$\begin{aligned}
\tilde{h}_{+,\times}(f) &= A(f) q_{+,\times}(\iota) e^{i(2\pi t_c + \Psi_c + \Psi(f) \mp \pi/4)}, \ f < f_{\text{cut}} \\
A(f) &= \sqrt{\frac{5}{24}} \pi^{-2/3} \frac{(1+z)c}{d_L} \left(\frac{G\mathcal{M}}{c^3}\right)^{5/6} f^{-7/6} \\
\Psi(f) &= \Psi_0 + \Psi_{0.5} + \Psi_{1.0} + \Psi_{1.5} + \Psi_{2.0}
\end{aligned} \tag{1.37}$$

which follows the treatment of Ref. [20, 21] using what is called the stationary phase approximation. To PN-Order 2.0 the phase comes out to be,

$$\begin{aligned}
\Psi_0 &= \frac{3}{128} \left(\frac{G\mathcal{M}\pi f}{c^3}\right)^{-5/3} \\
\Psi_{0.5} &= 0 \\
\Psi_{1.0} &= \frac{3}{128} \left(\frac{3715}{756} + \frac{55\eta}{9}\right) \eta^{-2/5} \left(\frac{G\mathcal{M}\pi f}{c^3}\right)^{-1} \\
\Psi_{1.5} &= -\frac{3}{8} \pi \eta^{-3/5} \left(\frac{G\mathcal{M}\pi f}{c^3}\right)^{-2/3} \\
\Psi_{2.0} &= \frac{3}{128} \left(\frac{15293365}{508032} + \frac{27145\eta}{504} + \frac{3085\eta^2}{72}\right) \eta^{-4/5} \left(\frac{G\mathcal{M}\pi f}{c^3}\right)^{-1/3}
\end{aligned} \tag{1.38}$$

where spin terms are ignored since we assume a non-spinning, circular binary.

For $h_\times(f)$ the polarization is $\pi/2$ out of phase from $h_+(f)$ so the "+" polarization uses the $-\pi/4$ and the "$\times$" polarization uses the $+\pi/4$ in the phase. Here $q(\iota)$ is an inclination factor as a function of ι for each polarization. Note: $\cos\iota = \hat{L} \cdot \hat{n}$ where $\hat{L}$ is a unit vector along the total angular momentum of the binary and $\hat{n}$ is the direction from the source to the observer. Here,

$$\begin{aligned}
q_+(\iota) &= \frac{1}{2}(1 + \cos^2 \iota) \\
q_\times(\iota) &= \cos\iota
\end{aligned} \tag{1.39}$$

For "edge-on" binaries $\iota = \pm\pi/2$ so that $\cos\iota = 0$ and the observer only has access to the "+" polarization content. When $\cos\iota$ goes from positive values to negative values the the sign of the "$\times$" polarization changes sign. Switching signs signifies its shift between "left" and "right" polarization. Basically a signal face-on to the observer will have an equal combination of both polarization states that will create a circular polarization pattern. How these interact the the detector, or network of detectors, is important but to simplify our work we will average out all angular dependence in this analysis.

1.3 Gravitational Wave Analysis

Using the technique of matched filtering, it is possible to extract signals with known shapes from noise that has much higher amplitude.

Signal and Noise

Starting with the GW detector output as a time series which is a combination of signal and noise. To understand how signal and noise combine, view the GW detector as a linear system, where H is a linear operator:

$$H : x(t) \longmapsto y(t) \tag{1.40}$$

Here $x(t)$ is the input and $y(t)$ is the output. The detector input is the GW strain $h(t) = D^{ij}h_{ij}(t)$, where D^{ij} is the detector tensor that encodes the geometry (i.e., antenna pattern) of the detector. This is constant for the duration of the GW signal, which is valid for ground-based detectors. For a linear system, the output of the detector is a linear function in frequency space of the input $h(t)$. In the absence of noise $n(t) = 0$,

$$\tilde{h}_{\text{out}}(f) = T(f)\tilde{h}(f) \tag{1.41}$$

where $T(f)$ is the transfer function of the system (referring to different stages of detection). In a real GW detector the output, with noise, would be,

$$s_{\text{out}}(t) = n_{\text{out}}(t) + h_{\text{out}}(t) \tag{1.42}$$

A real-world detector can be modeled as a linear system composed of many stages: $T(f) = \Pi_{i=1}^{N} T_i(f)$. It's better to write things in terms of input stages, rather than dealing with $T(f)$ for each stage. Refer noise $n(t)$ to input stage,

$$\tilde{n}(f) = T^{-1}(f)\tilde{n}_{\text{out}}(f) \tag{1.43}$$

with $n_{\text{out}}(t)$ as the total noise measured at the output. Basically, $n(t)$ is a "fictitious noise," which if injected at the input it would generate $n_{\text{out}}(t)$ at the output that is actually observed (given no other noise inside the detector). This ultimately means $n(t)$ is what we want to directly compare to $h(t)$. We then define,

$$s(t) = n(t) + h(t) \tag{1.44}$$

as the detector output (although referenced to at the input). The detection problem is how to distinguish $h(t)$ from $n(t)$.

Random Variables and Random Processes

Broadly speaking the noise $n(t)$ is a random process; a series of random variables indexed by t. A random variable is a variable subject to variations due to chance, i.e., randomness. The random variable can take on a set of possible values, each associated with a probability. Here random variable X is a map (measurable function) from the set of possible outcomes Ω to the real numbers $\Re$,

$$X: \quad \Omega \longmapsto \Re \tag{1.45}$$

$$\omega \longmapsto X(\omega) = x \tag{1.46}$$

where the set of outcomes (events) Ω is equipped with a probability measure P. The probability that X takes a numerical value $\leq c$ is denoted by $P(X \leq c)$. It is the measure of the set of outcomes Ω,

$$\{\omega \in \Omega : X(\omega) \leq c\} \tag{1.47}$$

Random variables can be discrete or continuous. For continuous variables, the probability measure is given by a probability density function (PDF), which describes the distribution of the random variable and assigns probabilities to intervals. Let X be a continuous random variable and $f(x)$ its PDF. Then the probability of the value of X to fall in a given interval $[a, b]$ is given by $P(a \leq x \leq b) = \int_a^b dx\, f(x)$. Two primary set of parameters needed to characterize a random variable is its expectation value and variance. The expectation value of a continuous random variable x with PDF $f(x)$ is $\langle x \rangle := \int_{\Re} dx\, x f(x)$. Its variance is $\mathrm{Var}(x) := \langle (x - \langle x \rangle)^2 \rangle$, where this is often denoted as $\mathrm{Var}(x) = \sigma_x^2$ for standard deviation σ_x.

The joint probability distribution of two continuous random variables x, y gives the probability that x, y fall into a range of values specified for that variable. The two continuous random variables x, y are independent if the joint PDF is,

$$f_{XY}(x, y) = f_X(x) f_Y(y) \tag{1.48}$$

Correlation refers to a class of statistical relationships involving dependence. Formally, this refers to random variables that are not independent and the degree of correlation is measured by correlation coefficients. One example is the Pearson product-moment correlation coefficient,

$$\mathrm{corr}(x, y) = \frac{\mathrm{cov}(x, y)}{\sigma_x \sigma_y} = \frac{\langle (x - \langle x \rangle)(y - \langle y \rangle) \rangle}{\sigma_x \sigma_y} \tag{1.49}$$

Above is the covariance, which is a measure of how much two random variables change together. If two random variables are independent, their covariance vanishes, and $\langle xy \rangle = \langle x \rangle \langle y \rangle$.

Functions that describe correlation are a statistical correlation between random variables at different points in space or time, e.g.,

$$\langle n(t_1)n(t_2) \rangle = \int dy_1 dy_2 \, y_1 y_2 f_{y_1 y_2}(t_1, y_2; t_2, y_2) \tag{1.50}$$

where as an example $n(t_i)$ can be noise measurements and $f_{y_1 y_2}(t_1, y_2; t_2, y_2)$ is a joint PDF. Auto-correlation: same variable at different point. Cross-correlation: different variables at same point. A stationary random process is a stochastic process whose joint probability distribution is unchanged,

$$f(t_1, y_1; t_2, y_2; \dots) \equiv f(t_1 - \tau_1, y_1; t_2 - \tau_2, y_2; \dots) \tag{1.51}$$

In this thesis we shall model the detector noise as a stationary, Gaussian random process. Gaussian random processes are stochastic processes in time and space, where every random variable is normally distributed. A Gaussian random process is completely described by their one-point (mean value) and two-point (power spectrum) correlation functions.

To determine amount of power in each frequency bin we first consider stationary noise $n(t)$ with zero mean ($\langle n(t) \rangle = 0$). By the Wiener–Khinchin theorem, a stationary random process has its PSD twice the Fourier transform of the autocorrelation function,

$$R_n(\tau) = \langle n(t)n(t + \tau) \rangle \tag{1.52}$$

It can be shown,

$$S_n(f) = 2 \int_{-\infty}^{\infty} d\tau \, R_n(\tau) e^{2\pi i f \tau} \tag{1.53}$$

Alternatively, one can consider the expected value of the frequency components $\tilde{n}(f)$. It can be shown after setting $t = t' + \tau$,

$$\langle \tilde{n}(f) \tilde{n}^*(f') \rangle = \frac{1}{2} S_n(f) \delta(f - f') \tag{1.54}$$

which is what most papers start with. If S_n is independent of f, this is white noise, i.e., a flat PSD (each frequency bin has the same amount of power in it). If S_n depends on f, then it is colored noise (certain frequency bins have more or less power).

Matched Filtering

Matched filtering is used to help distinguish between the signal and noise. In general, $|h(t)| \ll |n(t)|$, but we can detect $h(t)$ if we have some prior knowledge of $h(t)$. Let $s(t) = n(t) + h(t)$ be the recorded strain and define,

$$\hat{s} := \int_{-\infty}^{\infty} dt\, K(t)s(t) \tag{1.55}$$

where $K(t)$ is called the filter function. Assume the signal $h(t)$ is known. The filter function $K(t)$ that maximizes the signal-to-noise ratio (SNR) in $\hat{s}$ can be determined. Since the filter $K(t)$ is chosen to "match" the signal, the technique is called "matched filtering." Note we restrict ourselves to linear filters since $\hat{s}(t)$ is linear in $s(t)$.

The SNR is defined as S/N, where S is the expected value of $\hat{s}$ when $h(t)$ is present and N is the root-mean-squared (RMS) value of $\hat{s}$ when $h(t)$ is absent from $\hat{s}$. When $\langle n(t)\rangle = 0, h(t) \neq 0$,

$$S = \int_{-\infty}^{\infty} dt\, h(t)K(t) = \int_{-\infty}^{\infty} df\, \tilde{h}(f)\tilde{K}^*(f) \tag{1.56}$$

When $\langle n(t)\rangle = 0, h(t) \neq 0$, it can be shown,

$$N^2 = \langle s^2(t)\rangle - \langle s(t)\rangle^2 = \frac{1}{2}\int_{-\infty}^{\infty} df\, S_n(f)|\tilde{K}(f)|^2 \tag{1.57}$$

The inner product of two real functions $A(t), B(t)$, is,

$$(A|B) = 4\Re \int_0^{\infty} df\, \frac{\tilde{A}(f)\tilde{B}^*(f)}{S_n(f)} \tag{1.58}$$

which implies $S/N = (u|h)/(u|u)$, where $u(t)$ is such that $\tilde{u}(f) = S_n(f)\tilde{K}(f)/2$. To maximize $\tilde{u}(f) \propto \tilde{h}(f)$ the matched (Wiener) filter is defined

$$\tilde{K}(f) = \text{const.}\frac{\tilde{h}(f)}{S_n(f)} \tag{1.59}$$

This allows us to define the (optimal) SNR, often denoted as ρ,

$$\rho^2 = 4\int_0^{\infty} df\, \frac{|\tilde{h}(f)|^2}{S_n(f)} \tag{1.60}$$

Here we discuss optimal detection statistic while not knowing where a signal is present. Starting with the null hypothesis $\mathcal{H}_0$ (just noise $s(t) = n(t)$) and the alternative hypothesis $\mathcal{H}_1$ (GW is present $s(t) = n(t) + h(t)$). We wish to distinguish between the two hypotheses. This is done by computing the odds ratio,

$$O = \frac{P(\mathcal{H}_1|s)}{P(\mathcal{H}_0|s)}. \tag{1.61}$$

Recalling conditional probability,

$$P(A|B) = \frac{P(A,B)}{P(B)}, \tag{1.62}$$

where $P(A,B)$ is the joint probability that both A and B are true and $P(B)$ is the probability that B is true. Bayes theorem states,

$$P(B|A) = \frac{P(B)P(A|B)}{P(A)}, \tag{1.63}$$

in which $P(B|A)$ is the posterior probability of B given A, $P(B)$ is the prior, $P(A)$ is the evidence, and $P(A|B)$ is the conditional probability. From the completeness relation the likelihood ratio is,

$$\Lambda(B|A) = \frac{P(A|B)}{P(A|\bar{B})}, \tag{1.64}$$

where $\bar{B}$ means B is not true, which then implies,

$$O(B|A) = O(B)\Lambda(B|A). \tag{1.65}$$

Here $O(B)$ is the prior odds ratio of B being true. In terms of the hypotheses testing,

$$\Lambda(\mathcal{H}_1|s) = \frac{P(s|\mathcal{H}_1)}{P(s|\mathcal{H}_0)}. \tag{1.66}$$

Using Gaussian noise $s(t) = n(t)$ the PDF is,

$$f(s|\mathcal{H}_0) = f_n\left(s(t)\right) \propto e^{-(s|s)/2}. \tag{1.67}$$

For the alternative hypothesis $n(t) = s(t) - h(t)$, thus,

$$f(s|\mathcal{H}_1) = f_n\left(s(t) - h(t)\right) \propto e^{-(s-h|s-h)/2}. \tag{1.68}$$

This results in the likelihood ratio,

$$\Lambda\left(\mathcal{H}_1|s\right) = e^{(s|h)}e^{-(h|h)/2}, \tag{1.69}$$

where $(s|h)$ only depends on $s(t)$ through the inner product and $(h|h)$ is constant. The above likelihood is a monotonically increasing function of the inner product $(s|h)$, it defines the optimal detection statistic.

Sky-averaging

The full response on a detector is basically a dimensionless strain on the detector,

$$\Delta L(t)/L = F_+(\theta,\phi,\psi)h_+(t,\iota) + F_\times(\theta,\phi,\psi)h_\times(t,\iota), \tag{1.70}$$

where L is the length of the detector and the $\Delta L(t)$ is the time variation differential length in the detector arm. Recall ι is the inclination of the binary relative to the observer. Here $F_{+,\times}(\theta,\phi,\psi)$ are the detector *antenna patterns* which, in the detector frame, depend on polar angles θ,ϕ and the *polarization* angle ψ references the GW's frame of reference rotated from the detector frame. To refer these *wave frame* angles to the binary source frame both ι and ψ can be transformed to the source frame. Explicitly the patterns are,

$$\begin{aligned} F_+(\theta,\phi,\psi) &= \frac{1}{2}\left(1+\cos^2\theta\right)\cos 2\phi\cos 2\psi - \cos\theta\sin 2\phi\sin 2\psi, \\ F_\times(\theta,\phi,\psi) &= \frac{1}{2}\left(1+\cos^2\theta\right)\cos 2\phi\sin 2\psi + \cos\theta\sin 2\phi\cos 2\psi, \end{aligned} \tag{1.71}$$

for detector arms that are perpendicular to each other. These detectors are the interferometers and would extend along the x-axis and the y-axis. To visualize the antenna pattern we can plot both $F_{+,\times}$ setting $\psi = 0$ (this means we're referring the antenna pattern to the detector's own axis). The left panel of figure 1.2 is the pattern for the $+$-pattern which is in orange and $\times$-pattern which is in blue. This shows how the detector can access both polarization strains yet not disentangle them. The right panel is averaged over the polarization angle so is the unpolarized pattern.

We can perform an averaging scheme to not have to worry about the angles. Averaging over the angles in spherical coordinates results in some function $x(\theta,\phi,\psi,\iota)$ being averaged as,

$$\langle x(\theta,\phi,\psi,\iota)\rangle = \frac{1}{16\pi^2}\int_0^{\pi}\int_0^{\pi}\int_0^{2\pi}\int_0^{2\pi} x(\theta,\phi,\psi,\iota)\sin\iota\,\sin\theta\, d\phi\, d\psi\, d\iota\, d\theta. \tag{1.72}$$

Note the factor of $16\pi^2$ is just a normalization factor. Now we can rewrite the strain as,

$$h(t) = w(\theta,\phi,\psi,\iota)\zeta(t), \tag{1.73}$$

where,

$$w(\theta,\phi,\psi,\iota) = F_+(\theta,\phi,\psi)\frac{1+\cos^2\iota}{2} + F_\times(\theta,\phi,\psi)\cos\iota, \tag{1.74}$$

and $\zeta(t)$ is just the oscillating factor. Note that although both polarizations will technically have different $\zeta(t)$ they still have the same amplitude (absent of angles)

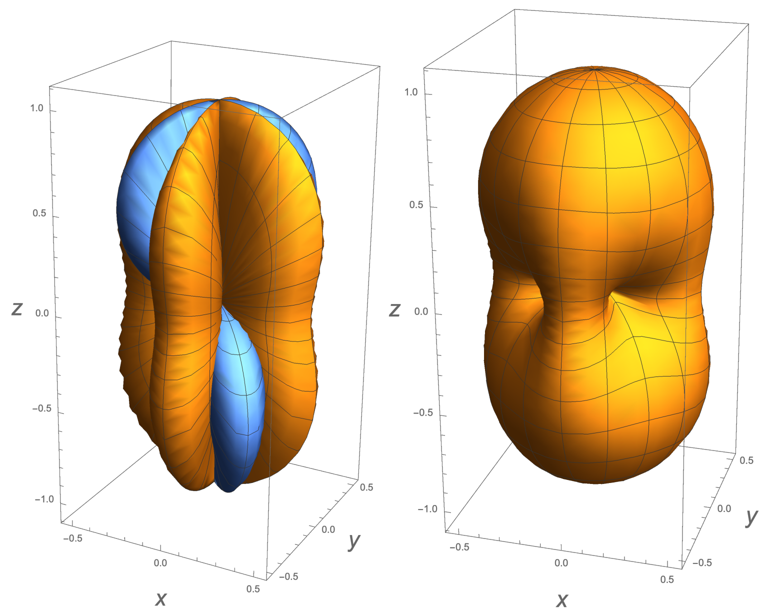

Figure 1.2: Antenna pattern distributions with detector arms extending along the postive x- and y-axis. Left is the pattern for the "+"-pattern (orange) and "×"-pattern (blue). Right is averaged over the polarization angle so is the unpolarized distribution.

and just out of phase by $\pi/2$, analogous to how sin and cos are just out of phase. If you angle average both independently you get the same result as to what is being done here. Here $0 \leq w(\theta, \phi, \psi, \iota) \leq 1$ where the optimal configuration has $w = 1$ when $\iota = 0$ and $\theta = 0$. The $\iota = 0$ case means you have both polarizations emitted in equal amplitude and is the "face-on" binary system and from the antenna pattern distribution we see $\theta = 0$ (or along the z-axis) as the optimal direction a GW would hit the detector. Technically,

$$w(\theta = 0, \phi, \psi, \iota = 0) = \cos\left(2(\phi + \psi)\right) + \sin\left(2(\phi + \psi)\right), \tag{1.75}$$

but ϕ, ψ can be chosen so that $w = 1$. Averaging the values gives,

$$\begin{aligned}
\langle F_+(\theta, \phi, \psi)^2 \rangle &= \frac{1}{5}, \\
\langle F_\times(\theta, \phi, \psi)^2 \rangle &= \frac{1}{5}, \\
\langle F_+(\theta, \phi, \psi) F_\times(\theta, \phi, \psi) \rangle &= 0, \\
\langle w(\theta, \phi, \psi, \iota)^2 \rangle &= \left(\frac{2}{5}\right)^2, \\
\langle w(\theta, \phi, \psi, \iota) \rangle &= 0.
\end{aligned}$$

Note that we work in frequency space, our averaging scheme will work in either frequency or time space because here the angles will not be time-dependent.

We noted that $w = 1$ is our optimal configuration. Here $\rho_{\rm opt}$ is the optimal SNR and in the configuration,

$$\rho^2 = 4w(\theta, \phi, \psi, \iota)^2 \Re \int_0^\infty \frac{|\tilde{\zeta}(f)|^2}{S(f)} df, \tag{1.76}$$

where $\tilde{\zeta}(f) = \mathcal{F}[\zeta(t)](f)$ then the angle-averaging gives us,

$$\rho_{\rm ave} = \frac{2}{5}\rho_{\rm opt}, \tag{1.77}$$

since $\sqrt{\langle w(\theta, \phi, \psi, \iota)^2 \rangle} = 2/5$. This averaging method works for any form of the noise-weighted inner product since the the angles are separate from the frequency domain. For non-orthogonal detectors and detectors that vary rapidly compared to the duration of the waveform other methods are needed. Technically speaking this method should only work for orthogonal ground-based detectors since the waveform duration for signals considered in the analysis is $\sim 1 - 10$ [s]. The Earth still stays relatively motionless in that time. A more thorough approach would be to look at how the space-based detectors' angles vary for a year and develop a separate averaging scheme for them (detectors in the deci-hertz and milli-hertz range will all be space-based). Basically this "tumbling" of the detectors in space complicates things for the long-duration signals and is still being addressed thoroughly.

1.4 Current Detectors, Future Detectors, and Prospects of Multi-Band GW Astronomy

Direct detections of gravitational waves (GWs) by the LIGO Scientific Collaboration [11, 26–34] are historic. As detector upgrades come online next generation 3G detectors, such as Cosmic Explorer (CE) [18, 22, 35, 36] and Einstein Telescope (ET) [37, 38], are planned to probe the cosmic horizon of GW events. Figure 1.3 displays the range to which future detectors such as CE and ET can observe. To demonstrate 3G detectors' level of sensitivity, compared to current detectors, figure 1.4 displays detector noise curves with GW signals simulated from IMRPhenomD using PyCBC [39]. Planned upgrades, e.g., A+ and Voyager, are also shown. These GW events are sampled from two different mass distributions, where the sampling procedure will be discussed in the next section.

The surprisingly high masses of kilohertz signals observed so far have provided interesting prospects of multi-band GW astronomy. Some of the systems observed by

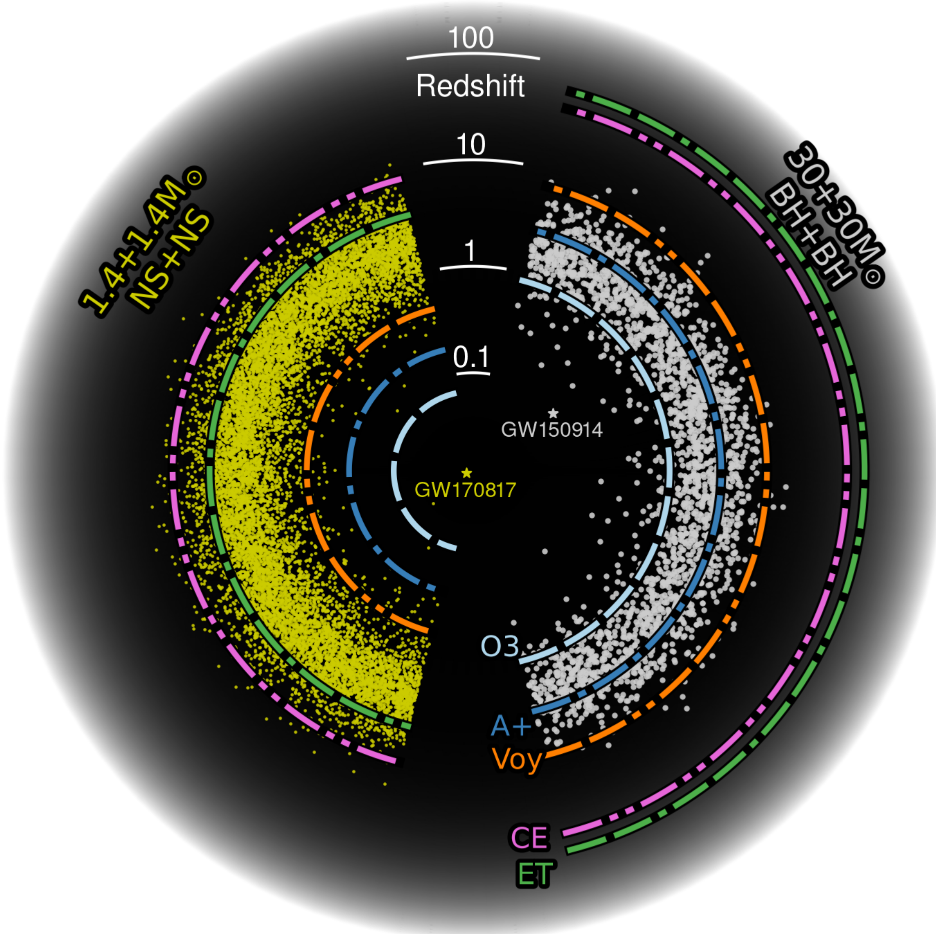

Figure 1.3: Horizon of current and future GW detectors for compact binaries. Dotted lines are detectors, white lines marking the redshift, and dots represent binary sources (yellow for NS-NS and white for BH-BH). The sources are equal mass systems with a merger of 100 Myrs. Image take from Ref [18, 22].

LIGO to date would also have been observable by a space-based Laser Interferometer Space Antenna (LISA) [40]. Given space-based detectors, observing in conjunction with Adv. LIGO, GW150914-like systems will be detectable in the centihertz range, merging in Adv. LIGO's band on a timescale of less than a decade [40]. In December of 2015, the European Space Agency launched LISA Pathfinder, a technology demonstration mission that has been a great success [41]. The results have also provided updated noise curves for a new LISA design set to launch in the next 20 years [17]. One of the science objectives for LISA is to keep a GW150914-like system detectable in the LISA band with a (signal-to-noise) SNR threshold $\rho_{\text{LISA}} \geq 7$ during the four year space mission. This would advance GW astronomy to begin observing GW signals across multiple bandwidths. Once a GW150914-

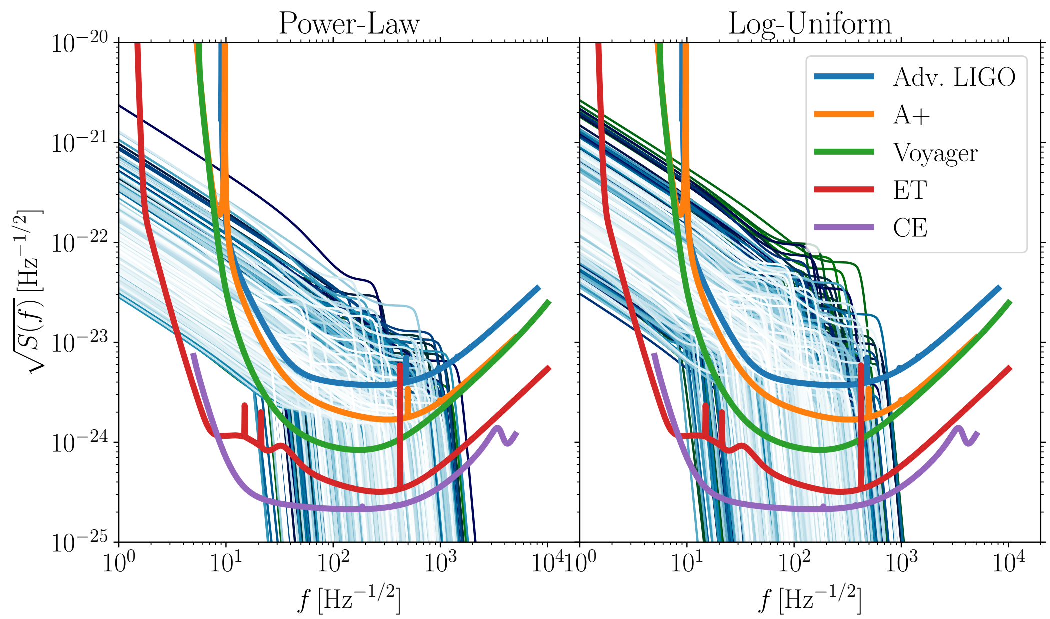

Figure 1.4: Current and next generation detectors. For each detector the curves represent the noise PSD $\sqrt{S_n}$ where n representing the noise curve for LIGO, A+, Voyager, Einstein Telescope, and Cosmic Explorer. A realization of 1000 sources $\sqrt{S_h} = 2|\tilde{h}|\sqrt{f}$ are sampled from an optimally oriented power-law (left panel) and log-uniform (right panel) mass distribution. Total mass of the systems are restricted to $\leq 100 M_{\odot}$. Here z is sampled from a uniform comoving volume without a specific star formation assumed. No SNR restrictions are imposed on the displayed source signals (implemented via IMRPhenomD).

like system advances to 1 decihertz, the signal will enter Adv. LIGO's band on a timescale of two weeks. This advance warning allows electromagnetic observers to concentrate on the source's sky location for any (although rare) EM counterpart and perform additional tests of GR. This prospect of multi-band GW astronomy also has a promising future in the decihertz regime with latest proposed TianGO [23] and other proposed detectors [24, 25].

One major advantage to multi-band observations is the accurate sky-localization, which, along with an identified host galaxy [42], will give an independent measurement of the luminosity distance and redshift. This will also allow accurate study of GW cosmology and the possibility of studying weak-lensing potentials. At cosmological distances every GW source will be gravitationally lensed, causing a magnification or demagnification of the observed shear signal at the detector. The presence of this signal can be inferred statistically. Ref. [43] analyzed precision measurements of fundamental cosmological parameters, including measuring the

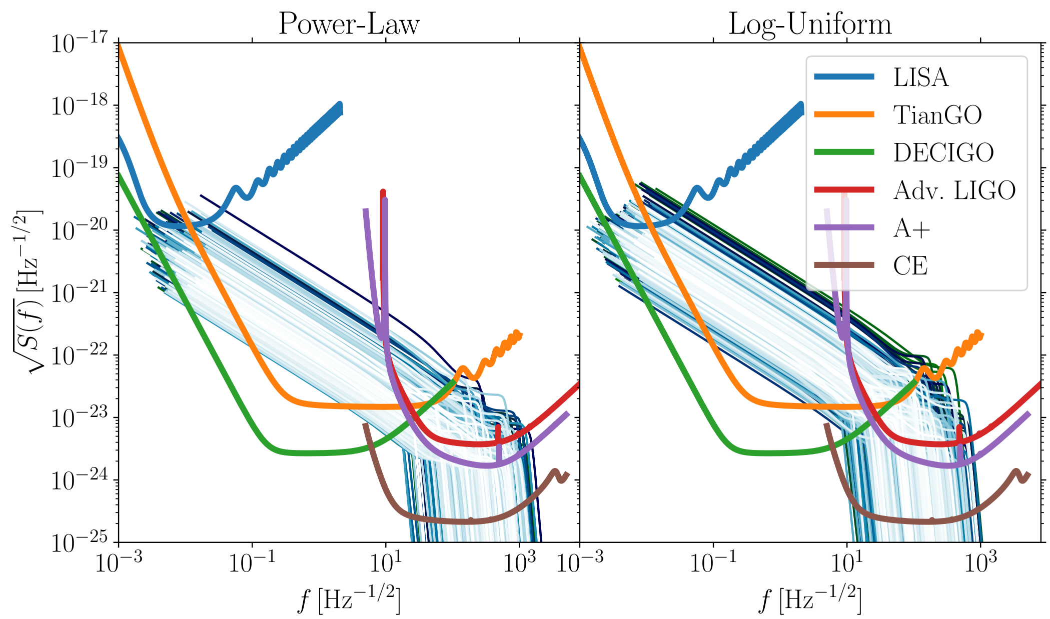

Figure 1.5: Demonstration of multiband GW astronomy. This is the same sampling procedure of Figure 1.3 where noise curves $\sqrt{S_n}$ for Voyager and Einstein Telescope are excluded. Millihertz and decihertz space-based detectors LISA, TianGO [23], and DECIGO [24, 25] are added. This example of multiband GW astronomy restricts each source to merge on a timescale of 10 years.

gravitational-lensing convergence power spectrum, in which errors on the absolute luminosity distance is dominated by effects of gravitational lensing magnification. Here the power spectrum from weak lensing shear is not only sensitive to distances between the observer, lens, and source, but also to the distribution of lenses. Measuring this distribution of lens and mapping the weak lensing potential will provide insight to growth of density perturbations. Ch. 2 will further investigate prospects of testing GR in the decihertz range.

To demonstrate, during the early inspiral of binary black holes (BBHs) Keplerian motion can, to zeroth order, be used to describe their motion and come to a description of the leading order evolution of the binary due to GW emission [44]. Here the orbital period P of the binary is related to the semi-major axis a as $P^2 \propto a^3$. The dominant GW frequency f is twice the orbital frequency of the binary, thus we can say $a \propto f^{-2/3}$. Ref. [44] provides a description of the time evolution of a circular binary due to GW emission, inspiraling and coalescing on a timescale $T_c(a) \propto a^4$.

Between two frequencies $f_{\rm low}$ and $f_{\rm up}$ this explicitly comes out as,

$$T = \frac{5}{256\eta}\frac{GM}{c^3}\left(\left(\frac{GM}{c^3}\pi f_{\rm low}\right)^{-8/3} - \left(\frac{GM}{c^3}\pi f_{\rm up}\right)^{-8/3}\right) \tag{1.78}$$

In this interval, the SNR accumulated is integrated from $f_{\rm low}$ to $f_{\rm up}$. For example, all detections with Adv. LIGO have had T_c varying from less than a second to a little under two seconds while accumulating an $\rho \sim 10 - 30$ at O1/O2 sensitivities. The most massive, GW150914, would have advanced from 1.7 to 10 centihertz in 4 years. The inspiral-merger-ringdown waveform, from the early inspiral to coalescence, of a GW150914-like system has $\rho_{\rm LISA} = 7$ and at design $\rho_{\rm LIGO} = 97$. Here the lower frequency of the IMR waveform is set so that $f_{\rm up} = 10$ Hz when calculating $\rho_{\rm LISA}$. The observing time is then set to LISA's space mission of $T = 4$ years. Then, using (1.78) we can estimate what the lower frequency is, which comes out to 1.7 centihertz for a $(36, 29)M_\odot$ system. The total time to coalesce from 1.7 centihertz is 4.03 years. This exemplifies the type of system expected to be observed in both bands. More massive systems will have lower $f_{\rm low}$ when $f_{\rm up} = 10$ Hz and $T = 4$ years are fixed, allowing more SNR to be accumulated while still merging on a time scale of ~ 4 years. Figure 1.5 extends the signals observed in figure 1.4 to where $f_{\rm low}$ is chosen so that the binaries coalesce in exactly 10 years.

1.5 Rates and Horizon

Provided an overall rate density, R, for the number of BBH mergers $\rm yr^{-1}Gpc^{-3}$, from some model, we assume a probability density for the intrinsic masses of the black hole binaries in the population. The probability densities are a log-uniform distribution $p \propto m_1^{-1}m_1^{-2}$ and a power-law (Salpeter) distribution $p \propto m_1^{-2.35}$, which is uniform in m_2. Here m_1 is treated as the primary with $m_1 \in (m_{\rm min}, m_{\rm max})$ and $m_2 \in (m_{\rm min}, m_1)$ where $m_{\rm min} = 5M_\odot$ and $m_1 + m_2 \leq 100M_\odot$. Figures 1.4 and 1.5 use this mass sampling range. The rate density R is take as the median estimated rates based on LIGO events and population models consistent with the log-uniform distribution, $R = 30\,\rm yr^{-1}Gpc^{-3}$, and the power-law distribution, $R = 100\,\rm yr^{-1}Gpc^{-3}$.

The total number N of BBHs expected to be observed per year by any given detector is calculated with,

$$N = \int_{m_{\rm min}}^{m_{\rm max}}\int_{m_{\rm min}}^{m_1}\int R\tilde{V}_c p\; dm_2 dm_1 \tag{1.79}$$

in which we take an observer time-weighted co-moving volume within which a

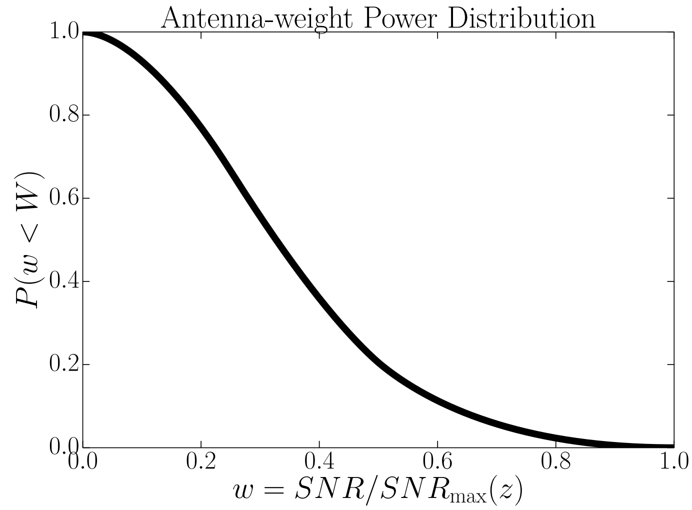

Figure 1.6: Antenna-weight power distribution implemented in integrating Eq. (1.80). This is equivalent to weighing the horizon distance by a "peanut" factor of 1/2.26 (MCMC methods evaluate a 1/2.26 weight factor in the antenna power distribution).

source of intrinsic masses can be observed,

$$\tilde{V}_c(m_1, m_2) = \int_0^{z_{\max}(m_1,m_2)} dz\, \frac{1}{(1+z)} \frac{dV_c}{dz} \tag{1.80}$$

Above, a cosmology is specified, characterized by the resulting differential co-moving volume density, dV_c/dz. Here $\tilde{V}_c$ depends on the maximal redshift that a source can be seen given intrinsic masses (m_1, m_2), set by an SNR threshold, which is set to $\rho_{\text{th}} = 8$ for Adv. LIGO. Methods to calculate $z_{\max}(m_1, m_2)$ involve: 1) a method of bisection that iteratively solves for $z_{\max}$ for each (m_1, m_2) in our grid, or 2) working with redshifted masses, then performing a coordinate transformation to get $\tilde{V}_c(m_1, m_2)$. Choosing the former, the result $d\tilde{V}_c$ is then integrated to $z_{\max}$ while being weighted by the antenna-weight power distribution plotted in figure 1.6. Summing over this weighting factor is equivalent to taking into account the antenna "peanut" factor 1/2.26 calculated via MCMC methods, e.g., see antenna power for single Adv. LIGO detector in figure 1.2.

Assuming Adv. LIGO at design, we calculate $z_{\max}, \tilde{V}_c$, and N over a grid of masses set by $m_1 \in (m_{\min}, m_{\max})$ and $m_2 \in (m_{\min}, m_1)$ with $m_{\min} = 5M_\odot$ and $m_1 + m_2 \leq 100M_\odot$. The mass spacing in this grid is set to $0.5M_\odot$. In the top left panel of figure 1.7, the maximal redshift $z_{\max}$ for each set of masses is calculated

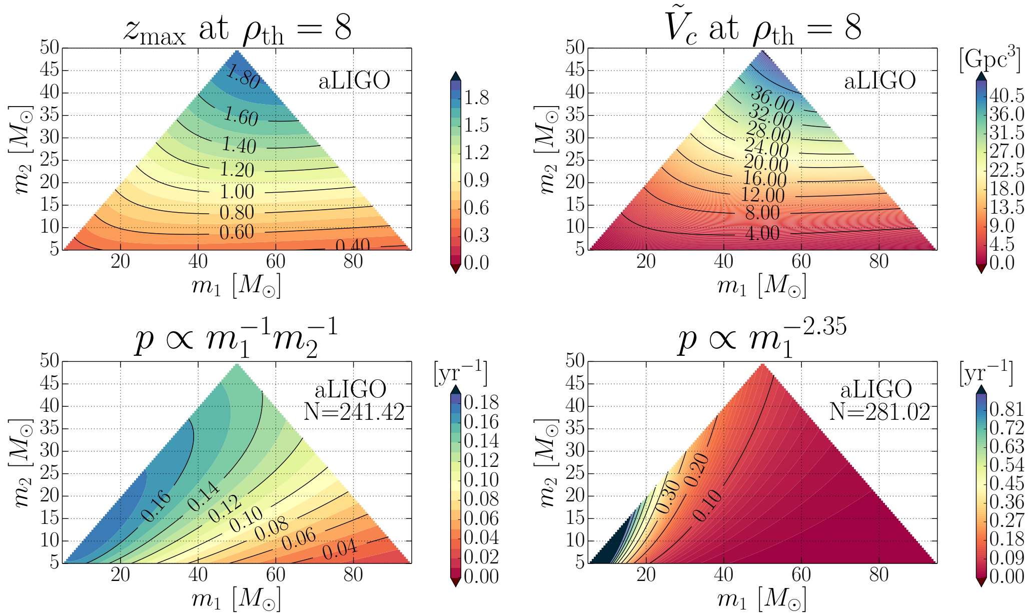

Figure 1.7: Horizon redshift, comoving volume, and rates for both power-law (Salpeter) and log-uniform distributions. Top Left: Maximal redshift evaluated via an iterative method of bisection for each pair of component masses $m_{1,2}$ on the mass grid. Top Right: Time-weighted comoving volume as a function of $m_{1,2}$. Bottom Left: Distribution of N over the mass grid for the log-uniform distribution. Bottom Right: Distribution of N over the mass grid for the power-law distribution. All grid spacings are set by $0.5 M_\odot$ and total N for each mass distribution are displayed. Adv. LIGO design noise curves are assumed and evaluated with IMRPhenomD.

via an iterative process by specifying component masses $m_{1,2}$ and method of bisection. Next $\tilde{V}_c$ is calculated after weighted by the antenna-weight power distribution displayed in figure 1.6. Using these primary ingredients we then use normalized probability densities p for the masses of the BBH in the population. In this analysis we use a log-uniform distribution $p \propto m_1^{-1} m_1^{-2}$ and a power-law (Salpeter) distribution $p \propto m_1^{-2.35}$, which is uniform in m_2. The results for the log-uniform distribution are displayed in the bottom left panel of figure 1.7 and the power-law distribution results are the bottom right panel of figure 1.7.

Summing all over mass bins we get $N = 241$, for the log-uniform, and $N = 281$, for the power-law. We can also perform partial sums, where for the log-uniform we get the following rates in the specified mass ranges,

$$\begin{aligned} N &= 1.9, m_1 \in (5, 10)M_\odot \\ N &= 92.5, m_1 \in (5, 40)M_\odot \\ N &= 148.9, m_1 \in (40, 100)M_\odot \end{aligned}$$

and for the power-law,

$$\begin{aligned} N &= 57.5, m_1 \in (5, 10)M_\odot \\ N &= 221.0, m_1 \in (5, 40)M_\odot \\ N &= 60.0, m_1 \in (40, 100)M_\odot \end{aligned}$$

For a LISA analysis on N, some caveats exist. To perform the analysis for LISA the SNR accumulated is restricted by the space missions duration (4 years). We need to accumulate the SNR over the full observation time so conversion between number of events with SNR above a threshold and the rate is not just a case of multiplying by the mission duration. Given that the signals duration is much longer than the detector's relative orientation during observation, the antenna-weight power distribution also needs to be reevaluated. See Ref. [45] for event rates estimates with LISA multiband events. For detectors like Cosmic Explorer rates estimates have been evaluated to ~ 1000 events per year with this method.

References

[1] F. W. Dyson, A. S. Eddington, and C. Davidson, Philosophical Transactions of the Royal Society of London Series A **220**, 291–333 (1920).

[2] C. M. Will, LRR **17**, 4, `10.12942/lrr-2014-4` (2014).

[3] R. A. Hulse and J. H. Taylor, ApJL **195**, L51–L53 (1975).

[4] M. Ishak, LRR **22**, 1, `10.1007/s41114-018-0017-4` (2019).

[5] S. Husa, General Relativity and Gravitation **41**, 1667–1669 (2009).

[6] *LIGO*, https://www.ligo.caltech.edu/.

[7] *Virgo*, https://www.virgo-gw.eu/.

[8] B. P. Abbott *et al.* (LIGO Collaboration) (LIGO Scientific Collaboration and Virgo Collaboration), PRX **9**, 031040, `10.1103/PhysRevX.9.031040` (2019).

[9] B. P. Abbott *et al.* (LIGO Scientific Collaboration and Virgo Collaboration), PRX **11**, 021053, `10.1103/PhysRevX.11.021053` (2021).

[10] B. P. Abbott *et al.* (LIGO Collaboration) (LIGO Scientific Collaboration and Virgo Collaboration), ApJL **915**, L5, `10.3847/2041-8213/ac082e` (2021).

[11] B. P. Abbott *et al.* (LIGO and Virgo Scientific Collaboration), arXiv e-prints, arXiv:2108.01045 (2021).

[12] B. P. Abbott *et al.* (LIGO Collaboration) (LIGO Scientific Collaboration and Virgo Collaboration), PRD **100**, 104036, `10.1103/PhysRevD.100.104036` (2019).

[13] B. P. Abbott *et al.* (LIGO Scientific Collaboration and Virgo Collaboration), PRL **123**, 011102, `10.1103/PhysRevLett.123.011102` (2019).

[14] B. P. Abbott *et al.* (LIGO Collaboration) (LIGO Scientific Collaboration and Virgo Collaboration), PRD **103**, 122002, `10.1103/PhysRevD.103.122002` (2021).

[15] B. P. Abbott *et al.* (LIGO Collaboration), arXiv e-prints, arXiv:2112.06861 (2021).

[16] *LISA*, https://lisa.nasa.gov/.

[17] P. Amaro-Seoane, H. Audley, S. Babak, J. Baker, E. Barausse, P. Bender, E. Berti, P. Binetruy, M. Born, D. Bortoluzzi, J. Camp, C. Caprini, V. Cardoso, M. Colpi, J. Conklin, N. Cornish, C. Cutler, K. Danzmann, R. Dolesi, L. Ferraioli, V. Ferroni, E. Fitzsimons, J. Gair, L. Gesa Bote, D. Giardini, F. Gibert, C. Grimani, H. Halloin, G. Heinzel, T. Hertog, M. Hewitson, K. Holley-Bockelmann, D. Hollington, M. Hueller, H. Inchauspe, P. Jetzer, N. Karnesis, C. Killow, A. Klein, B. Klipstein, N. Korsakova, S. L. Larson, J. Livas, I. Lloro, N. Man, D. Mance, J. Martino, I. Mateos, K. McKenzie, S. T. McWilliams, C. Miller, G. Mueller, G. Nardini, G. Nelemans, M. Nofrarias, A. Petiteau, P. Pivato, E. Plagnol, E. Porter, J. Reiche, D. Robertson, N. Robertson, E. Rossi, G. Russano, B. Schutz, A. Sesana, D. Shoemaker, J. Slutsky, C. F. Sopuerta, T. Sumner, N. Tamanini, I. Thorpe, M. Troebs, M. Vallisneri, A. Vecchio, D. Vetrugno, S. Vitale, M. Volonteri, G. Wanner, H. Ward, P. Wass, W. Weber, J. Ziemer, and P. Zweifel, arXiv e-prints, arXiv:1702.00786 (2017).

[18] *Cosmic Explorer*, https://cosmicexplorer.org/.

[19] S. M. Carroll, *Spacetime and Geometry* (Cambridge University Press, July 2019), ISBN: 978-1-108-48839-6.

[20] M. Maggiore, *Gravitational Waves. Vol. 1: Theory and Experiments*, Oxford Master Series in Physics (Oxford University Press, 2007), ISBN: 978-0-19-857074-5.

[21] C. Cutler and É. E. Flanagan, PRD **49**, 2658–2697 (1994).

[22] M. Evans, R. X. Adhikari, C. Afle, S. W. Ballmer, S. Biscoveanu, S. Borhanian, D. A. Brown, Y. Chen, R. Eisenstein, A. Gruson, A. Gupta, E. D. Hall, R. Huxford, B. Kamai, R. Kashyap, J. S. Kissel, K. Kuns, P. Landry, A. Lenon, G. Lovelace, L. McCuller, K. K. Y. Ng, A. H. Nitz, J. Read, B. S. Sathyaprakash, D. H. Shoemaker, B. J. J. Slagmolen, J. R. Smith, V. Srivastava, L. Sun, S. Vitale, and R. Weiss, arXiv e-prints, arXiv:2109.09882 (2021).

[23] K. A. Kuns, H. Yu, Y. Chen, and R. X. Adhikari, PRD **102**, 043001, `10.1103/PhysRevD.102.043001` (2020).

[24] S. Sato, S. Kawamura, M. Ando, T. Nakamura, K. Tsubono, A. Araya, I. Funaki, K. Ioka, N. Kanda, S. Moriwaki, M. Musha, K. Nakazawa, K. Numata, S.-i. Sakai, N. Seto, T. Takashima, T. Tanaka, K. Agatsuma, K.-s. Aoyanagi, K. Arai, H. Asada, Y. Aso, T. Chiba, T. Ebisuzaki, Y. Ejiri, M. Enoki, Y. Eriguchi, M.-K. Fujimoto, R. Fujita, M. Fukushima, T. Futamase, K. Ganzu, T. Harada, T. Hashimoto, K. Hayama, W. Hikida, Y. Himemoto, H. Hirabayashi, T. Hiramatsu, F.-L. Hong, H. Horisawa, M. Hosokawa, K. Ichiki, T. Ikegami, K. T. Inoue, K. Ishidoshiro, H. Ishihara, T. Ishikawa, H. Ishizaki, H. Ito, Y. Itoh, N. Kawashima, F. Kawazoe, N. Kishimoto, K. Kiuchi, S. Kobayashi, K. Kohri, H. Koizumi, Y. Kojima, K. Kokeyama, W. Kokuyama, K. Kotake, Y. Kozai, H. Kudoh, H. Kunimori, H. Kuninaka, K. Kuroda, K.-i. Maeda, H. Matsuhara, Y. Mino, O. Miyakawa, S. Miyoki, M. Y. Morimoto, T. Morioka, T. Morisawa, S. Mukohyama, S. Nagano, I. Naito, K. Nakamura, H. Nakano, K. Nakao, S. Nakasuka, Y. Nakayama, E. Nishida, K. Nishiyama, A. Nishizawa, Y. Niwa, T. Noumi, Y. Obuchi, M. Ohashi, N. Ohishi, M. Ohkawa, N. Okada, K. Onozato, K. Oohara, N. Sago, M. Saijo, M. Sakagami, S. Sakata, M. Sasaki, T. Sato, M. Shibata, H. Shinkai, K. Somiya, H. Sotani, N. Sugiyama, Y. Suwa, R. Suzuki, H. Tagoshi, F. Takahashi, K. Takahashi, K. Takahashi, R. Takahashi, R. Takahashi, T. Takahashi, H. Takahashi, T. Akiteru, T. Takano, K. Taniguchi, A. Taruya, H. Tashiro, Y. Torii, M. Toyoshima, S. Tsujikawa, Y. Tsunesada, A. Ueda, K.-i. Ueda, M. Utashima, Y. Wakabayashi, H. Yamakawa, K. Yamamoto, T. Yamazaki, J. Yokoyama, C.-M. Yoo, S. Yoshida, and T. Yoshino, in Journal of physics conference series, Vol. 840, Journal of Physics Conference Series (May 2017).

[25] S. Kawamura, T. Nakamura, M. Ando, N. Seto, T. Akutsu, I. Funaki, K. Ioka, N. Kanda, I. Kawano, M. Musha, K. Nakazawa, S. Sato, T. Takashima, T. Tanaka, K. Tsubono, J. Yokoyama, K. Agatsuma, K.-S. Aoyanagi, K. Arai, A. Araya, N. Aritomi, H. Asada, Y. Aso, D. Chen, T. Chiba, T. Ebisuzaki, S. Eguchi, Y. Ejiri, M. Enoki, Y. Eriguchi, M.-K. Fujimoto, R. Fujita, M. Fukushima, T. Futamase, R. Gondo, T. Harada, T. Hashimoto, K. Hayama, W. Hikida, Y. Himemoto, H. Hirabayashi, T. Hiramatsu, F.-L. Hong, H. Horisawa, M. Hosokawa, K. Ichiki, T. Ikegami, K. T. Inoue, H. Ishihara, T. Ishikawa, H. Ishizaki, H. Ito, Y. Itoh, K. Izumi, S. Kanemura, N. Kawashima, F. Kawazoe, N. Kishimoto, K. Kiuchi, S. Kobayashi, K. Kohri, H. Koizumi, Y. Kojima, K. Kokeyama, W. Kokuyama, K. Kotake, Y. Kozai, H. Kunimori, H. Kuni-

naka, K. Kuroda, S. Kuroyanagi, K.-I. Maeda, H. Matsuhara, N. Matsumoto, Y. Michimura, O. Miyakawa, U. Miyamoto, S. Miyoki, M. Y. Morimoto, T. Morisawa, S. Moriwaki, S. Mukohyama, S. Nagano, K. Nakamura, H. Nakano, K. Nakao, S. Nakasuka, Y. Nakayama, E. Nishida, A. Nishizawa, Y. Niwa, T. Noumi, Y. Obuchi, N. Ohishi, M. Ohkawa, K. Okada, N. Okada, K. Okutomi, K. Oohara, N. Sago, M. Saijo, R. Saito, M. Sakagami, S.-I. Sakai, S. Sakata, M. Sasaki, T. Sato, M. Shibata, K. Shibata, A. Shimo-Oku, H. Shinkai, A. Shoda, K. Somiya, H. Sotani, A. Suemasa, N. Sugiyama, Y. Suwa, R. Suzuki, H. Tagoshi, F. Takahashi, K. Takahashi, K. Takahashi, R. Takahashi, R. Takahashi, H. Takahashi, T. Akiteru, T. Takano, N. Tanaka, K. Taniguchi, A. Taruya, H. Tashiro, Y. Torii, M. Toyoshima, S. Tsujikawa, A. Ueda, K.-I. Ueda, T. Ushiba, M. Utashima, Y. Wakabayashi, K. Yagi, K. Yamamoto, T. Yamazaki, C.-M. Yoo, S. Yoshida, and T. Yoshino, International Journal of Modern Physics D **28**, 1845001, `10.1142/S0218271818450013` (2019).

[26] B. P. Abbott *et al.* (LIGO and Virgo Scientific Collaboration), ApJL **851**, L35, `10.3847/2041-8213/aa9f0c` (2017).

[27] B. P. Abbott *et al.* (LIGO and Virgo Scientific Collaboration), Physical Review X **9**, 031040, `10.1103/PhysRevX.9.031040` (2019).

[28] B. P. Abbott *et al.* (LIGO and Virgo Scientific Collaboration), ApJL **892**, L3, `10.3847/2041-8213/ab75f5` (2020).

[29] B. P. Abbott *et al.* (LIGO and Virgo Scientific Collaboration), PRD **102**, 043015, `10.1103/PhysRevD.102.043015` (2020).

[30] B. P. Abbott *et al.* (LIGO and Virgo Scientific Collaboration), ApJL **896**, L44, `10.3847/2041-8213/ab960f` (2020).

[31] B. P. Abbott *et al.* (LIGO and Virgo Scientific Collaboration), PRL **125**, 101102, `10.1103/PhysRevLett.125.101102` (2020).

[32] B. P. Abbott *et al.* (LIGO and Virgo Scientific Collaboration), Physical Review X **11**, 021053, `10.1103/PhysRevX.11.021053` (2021).

[33] B. P. Abbott *et al.* (LIGO and Virgo Scientific Collaboration), ApJL **915**, L5, `10.3847/2041-8213/ac082e` (2021).

[34] B. P. Abbott *et al.* (LIGO and Virgo Scientific Collaboration), arXiv e-prints, arXiv:2111.03606 (2021).

[35] D. Reitze, R. X. Adhikari, S. Ballmer, B. Barish, L. Barsotti, G. Billingsley, D. A. Brown, Y. Chen, D. Coyne, R. Eisenstein, M. Evans, P. Fritschel, E. D. Hall, A. Lazzarini, G. Lovelace, J. Read, B. S. Sathyaprakash, D. Shoemaker, J. Smith, C. Torrie, S. Vitale, R. Weiss, C. Wipf, and M. Zucker, in Bulletin of the american astronomical society, Vol. 51 (Sept. 2019).

[36] D. H. Shoemaker, S. Ballmer, M. Barsuglia, E. Berger, E. Berti, D. A. Brown, P. Chandra, M. Evans, K. Fang, W.-f. Fong, A. Freise, P. Fritschel, J. Greene, C. J. Horowitz, J. Kissel, B. Lantz, P. D. Lasky, H. Lueck, M. C. Miller, A. H. Nitz, D. Ottaway, H. V. Peiris, M. Punturo, D. H. Reitze, G. H. Sanders, B. S. Sathyaprakash, D. Sigg, B. Slagmolen, S. J. Smartt, J. R. Smith, A. W. Steiner, E. Troja, V. A. Villar, R. Weiss, S. C. Wolff, and J. Yeck, arXiv e-prints, arXiv:2112.12718 (2021).

[37] M. Punturo et al., CQG **27**, 194002, 10.1088/0264-9381/27/19/194002 (2010).

[38] B. Sathyaprakash et al., CQG **29**, 124013, 10.1088/0264-9381/29/12/124013 (2012).

[39] *PyCBC*, https://pycbc.org/.

[40] A. Sesana, PRL **116**, 231102, 10.1103/PhysRevLett.116.231102 (2016).

[41] M. Armano, H. Audley, G. Auger, J. T. Baird, M. Bassan, P. Binetruy, M. Born, D. Bortoluzzi, N. Brandt, M. Caleno, L. Carbone, A. Cavalleri, A. Cesarini, G. Ciani, G. Congedo, A. M. Cruise, K. Danzmann, M. de Deus Silva, R. De Rosa, M. Diaz-Aguiló, L. Di Fiore, I. Diepholz, G. Dixon, R. Dolesi, N. Dunbar, L. Ferraioli, V. Ferroni, W. Fichter, E. D. Fitzsimons, R. Flatscher, M. Freschi, A. F. Garcıa Marın, C. Garcıa Marirrodriga, R. Gerndt, L. Gesa, F. Gibert, D. Giardini, R. Giusteri, F. Guzmán, A. Grado, C. Grimani, A. Grynagier, J. Grzymisch, I. Harrison, G. Heinzel, M. Hewitson, D. Hollington, D. Hoyland, M. Hueller, H. Inchauspé, O. Jennrich, P. Jetzer, U. Johann, B. Johlander, N. Karnesis, B. Kaune, N. Korsakova, C. J. Killow, J. A. Lobo, I. Lloro, L. Liu, J. P. López-Zaragoza, R. Maarschalkerweerd, D. Mance, V. Martın, L. Martin-Polo, J. Martino, F. Martin-Porqueras, S. Madden, I. Mateos, P. W. McNamara, J. Mendes, L. Mendes, A. Monsky, D. Nicolodi, M. Nofrarias, S. Paczkowski, M. Perreur-Lloyd, A. Petiteau, P. Pivato, E. Plagnol, P. Prat, U. Ragnit, B. Raıs, J. Ramos-Castro, J. Reiche, D. I. Robertson, H. Rozemeijer, F. Rivas, G. Russano, J. Sanjuán, P. Sarra, A. Schleicher, D. Shaul, J. Slutsky, C. F. Sopuerta, R. Stanga, F. Steier, T. Sumner, D. Texier, J. I. Thorpe, C. Trenkel, M. Tröbs, H. B. Tu, D. Vetrugno, S. Vitale, V. Wand, G. Wanner, H. Ward, C. Warren, P. J. Wass, D. Wealthy, W. J. Weber, L. Wissel, A. Wittchen, A. Zambotti, C. Zanoni, T. Ziegler, and P. Zweifel, PRL **116**, 231101, 10.1103/PhysRevLett.116.231101 (2016).

[42] H.-Y. Chen and D. E. Holz, arXiv e-prints, arXiv:1612.01471 (2016).

[43] C. Cutler and D. E. Holz, PRD **80**, 104009, 10.1103/PhysRevD.80.104009 (2009).

[44] P. C. Peters, Phys. Rev. **136**, B1224–B1232 (1964).

[45] D. Gerosa, S. Ma, K. W. K. Wong, E. Berti, R. O'Shaughnessy, Y. Chen, and K. Belczynski, PRD **99**, 103004, 10.1103/PhysRevD.99.103004 (2019).

Chapter 2

TESTING GR WITH GRAVITATIONAL WAVES

2.1 Introduction to Testing GR

General relativity has had its foundations in theory and experimentation. Its foundation has relied heavily on these pillars of testing relativity, yet in its early creation the theory was not stringently tested. Apart from a few constraints, the bounds placed on the theory were limited. As the 20th century progressed, GR has proven to consistently be the correct descriptor of gravitational phenomena. Figure 2.1 catalogues tests of GR for nearly a century.

In the weak-field regime the parameterized post-Newtonian description (ppN) has provided a consistent framework for testing relativity in the slow-motion, weak-field regime. The ppN has been paramount in tests of GR, especially as the dynamical features of GR presented itself in the first binary neutron star detection featuring the non-linear dynamics of the theory [1]. The slow decay of the Hulse-Taylor binary's orbit due to GW emission provided the first indirect measurement of GWs and a picture of GR in its extreme environment. Since 2015 the direct observation of GW emission, as described by GR, has transformed the landscape of testing relativity [2–5]. Systems studied have advanced to violent encounters with binaries' orbital velocities approaching a fraction the speed of light. This has included low-mass, high-curvature binaries and high-mass, mid-curvature binaries. Even binary neutron stars with an EM counterpart provided some of the first realizations of multi-messenger GW astronomy [6, 7]. The most recent observation run from the LIGO Scientific Collaboration has completed and recent testing GR results are currently available [5]. From Ref. [5], figures 2.2 and 2.3 provide a sample of important results. Here A_α is a GW dispersion parameter: $E^2 = p^2 + p^\alpha A_\alpha$. All tests performed to date, in all areas, have confirmed GR as the best description of gravity.

2.2 Generation vs Propagation

Modifications of GR results occur in a variety of regions and stages of the GW emission and propagation process. On a timescale of $\lesssim$ 1 [s] a kilohertz GW signal is generated from high curvature black holes from the binary's dynamics in the strong-field region. A binary neutron star lasts $\sim$ 10 [s] in this frequency

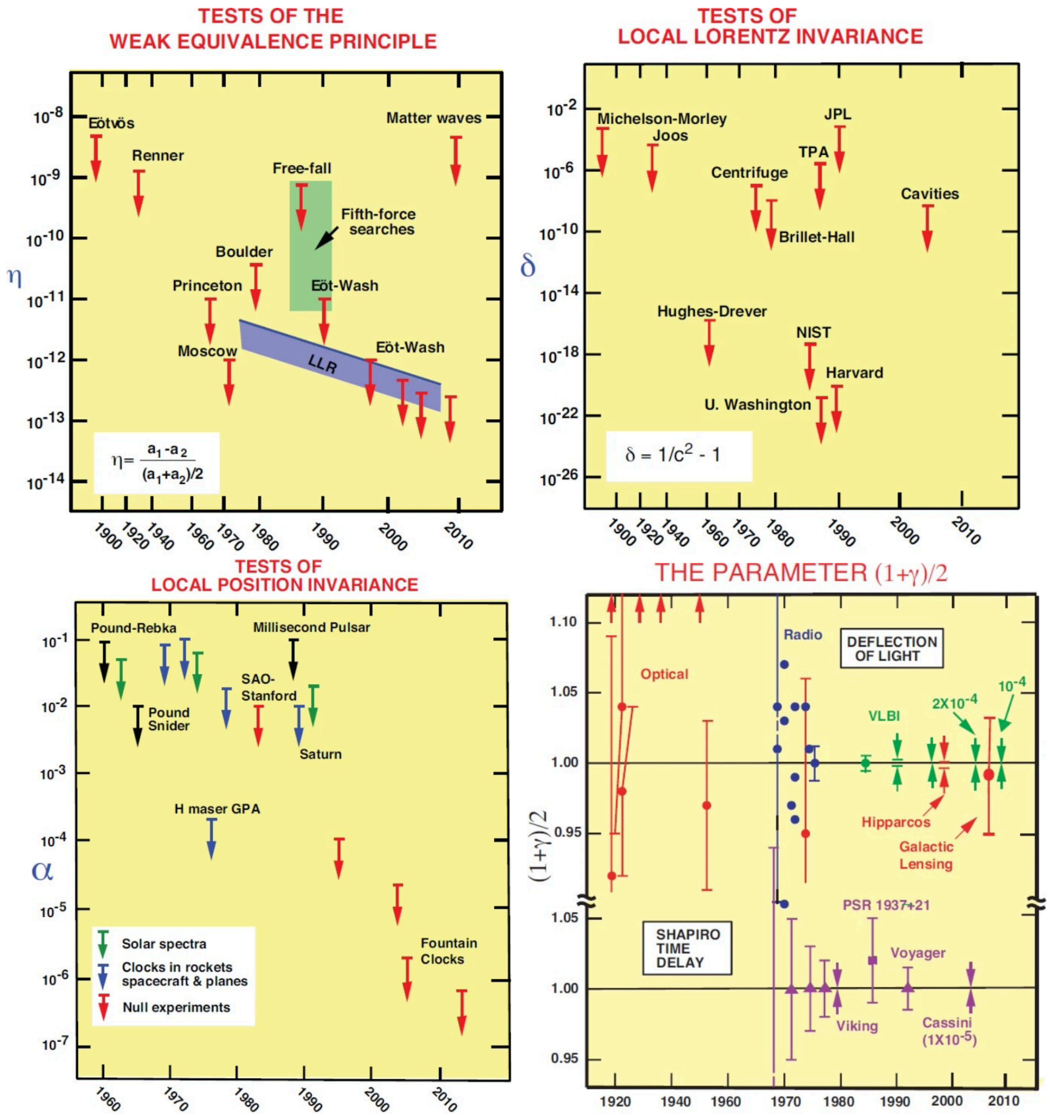

Figure 2.1: Catalogue of experiments and constraints placed on relativity (taken from Ref. [8]). Top left: limits of fractional differences placed on the acceleration between two bodies (the Eövös ratio). Top right: EM tests of Lorentz invariance measuring the speed of light. Top right: EM Lorentz invariance tests of relativity with EM style "clocks." Bottom left: gravitational redshift experiments via timing experiments. Bottom right: classical and modern light bending experiments including Shapiro time delay tests. All these tests probe the ppN parameter space, where $\eta = \delta = \alpha = 0$ and $\gamma = 1$ are the GR limit.

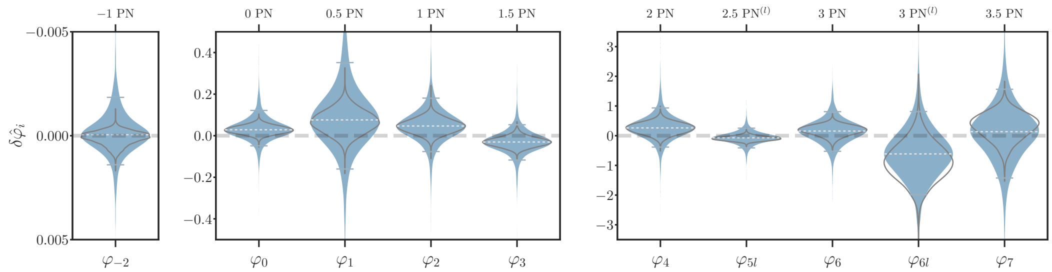

Figure 2.2: GWTC-3 combined results of parameterized deviation coefficients at various PN-orders. Filled regions are results obtained from hierarchically combined events. This allows the coefficients to assume different values for different events. Unfilled (black) curves are distributions obtained from 90% upper bound results, by assuming constant values of the deviation parameters across all events. Horizontal ticks are 90% credible intervals and white dashed are median values obtained with the hierarchical analysis. See Ref. [5].

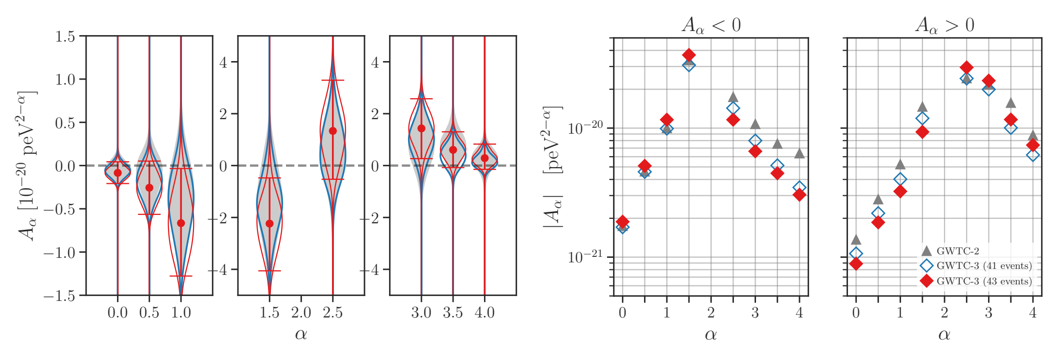

Figure 2.3: Generic dispersion modification results. Left: red violin plots show combined posteriors of beyond-GR parameter A_α measure from GWTC-3 events. Error bars are 90% credible intervals. Blue violin plots are combined posteriors after excluding events GW200219_094415 and GW200225_060421. Gray background plots are combined posteriors from GWTC-2. Right: scatter plot of 90% credible upper bounds on $|A_\alpha|$. Bounds are computed for positive and negative values of the parameters. Filled diamond markers are GWTC-3 bounds represent the GWTC-3 bounds including GW200219_094415 and GW200225_060421, the open diamonds exclude them. Gray markers are result from previous studies. See Ref. [5] for more discussion and details.

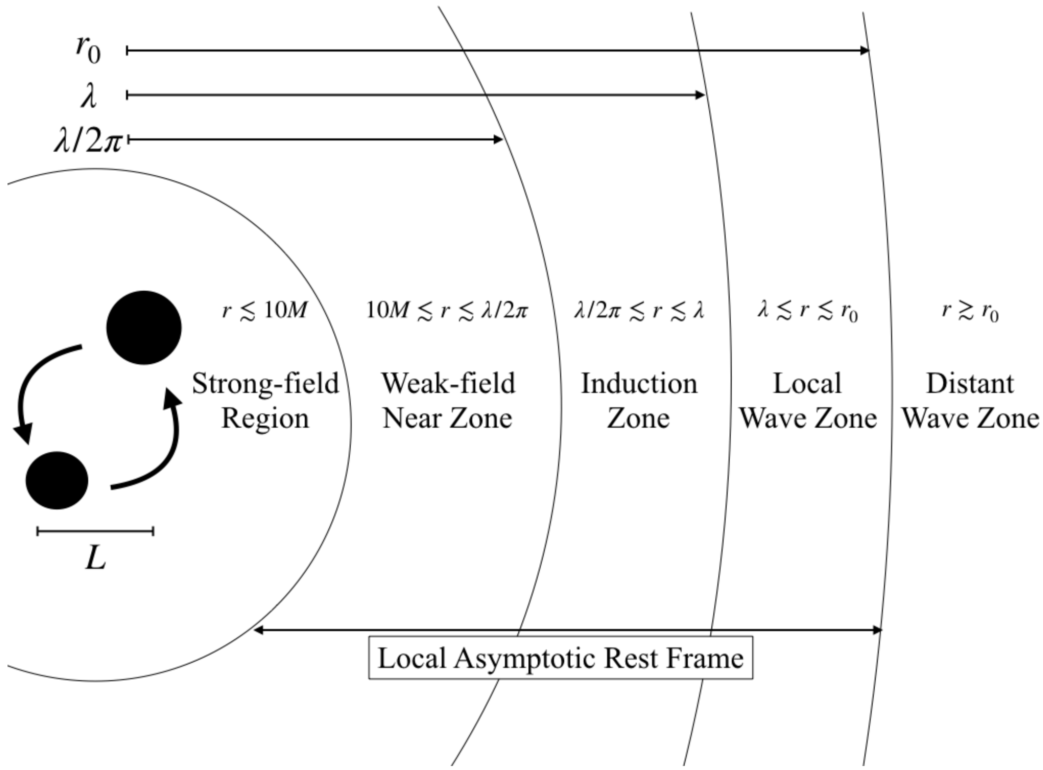

Figure 2.4: Separation of regions around a binary system. The total mass $M = m_1 + m_2$ and GW wavelength λ are used to separate length scales. The radial term r_0 can be left open for interpretation. For example r_0 can be a distance where local curvature does not influence propagation, where large scale curvature begins to influence propagation, or a screening radius for beyond GR effects as will be discussed in Ch. 6.

range. After the full inspiral-merger-ringdown (IMR) signal is generated the GW propagates through the weak-field near zone, the induction zone, and finally the wave zone (see figure 2.4). The final stage of the wave zone, i.e., the distant wave zone, is where the GW spends the majority of its time propagating to the observer [9].

To find deviations of GR, theory agnostic and theory specific models have been extensively developed and continue to be designed and improved [8, 10, 11]. When suppressing polarization dynamics, the general modifications occur to its amplitude and phase: $h = h_{\rm GR} A_{\rm bGR} e^{i\Psi_{\rm bGR}}$, where $A_{\rm bGR}$ and $\Psi_{\rm bGR}$ are beyond-GR enhancements extending the theory. Modifications to the GW's amplitude and phase occur from modifying, either both or individually, its generation and propagation dynamics. For example, changes to a binary's energy flux $\dot{E}_{\rm GR} \to \dot{E}_{\rm GR} + \delta\dot{E}_{\rm bGR}$ and the binary's energy $E_{\rm GR} \to E_{\rm GR} + \delta E_{\rm bGR}$ are examples of modifying the genera-

Table 2.1: Mapping ppE parameters to classes and specific beyond-GR theories. First row can encapsulate theories like Brans-Dicke and Einstein-dilaton Gauss-Bonnet (EDGB) gravity. Second row can describe massive graviton theories. Third row includes dynamical Chern-Simmons and fourth is parity violation. See Ref [11] on further discussion of these parameters.

a_{ppE}	b_{ppE}	Description
-	-7	Dipole GW Radiation, Dipole Scalar Radiation.
-	-3	Modified GW Disperson/Propagation.
$\propto$ spins	-1	Quadrupole Moment Correction, Scalar Dipole Force.
1	-	Parity violation.

tion process due to some theory beyond GR. This can lead to both amplitude and phase modulations. Pure modification to its propagation, e.g., extra compact dimensions [7, 12], can lead to both beyond GR effects in the phase and amplitude. Conversely, massive graviton theories with Vainshtein screening [13, 14] can lead to propagation dynamics surfacing purely in the phase in some massive graviton theories.

2.3 Parameterized Post-Einsteinian Framework

A common approach to encapsulate these dynamics is to consider parameterized models such as the parameterized post-Einsteinian (ppE) framework [10, 11], where generic modifications occur as,

$$
\begin{aligned}
A &= A_{\mathrm{GR}}\left(1+\delta A_{\mathrm{ppE}}\right), \\
\Psi &= \Psi_{\mathrm{GR}}+\delta\Psi_{\mathrm{ppE}},
\end{aligned}
\tag{2.1}
$$

in which the parameterized deviations in the phase and amplitude are expressed as,

$$
\begin{aligned}
\delta A_{\mathrm{ppE}} &= \alpha\left(\pi\mathcal{M}f\right)^{a}, \\
\delta\Psi_{\mathrm{ppE}} &= \beta\left(\pi\mathcal{M}f\right)^{b}.
\end{aligned}
\tag{2.2}
$$

Here the parameters (a, b) determine what post-Newtonian order the effects surface at, for example $b = -7$ is a weak-field PN-order -1.0 effect, $b = -3.0$ is PN-order 1.0, and $b = -1$ is PN-order 2.0 in the phase. See Table 2.1 for examples. The study performed here will reference this parameterization routinely, with later results concentrating primarily on the propagation effects rather than generation.

2.4 Tests with Kilohertz and Decihertz Detection

Considering current and future GW detectors discussed a look at beyond GR consistency tests of GR will be demonstrated. In this initial analysis two probabil-

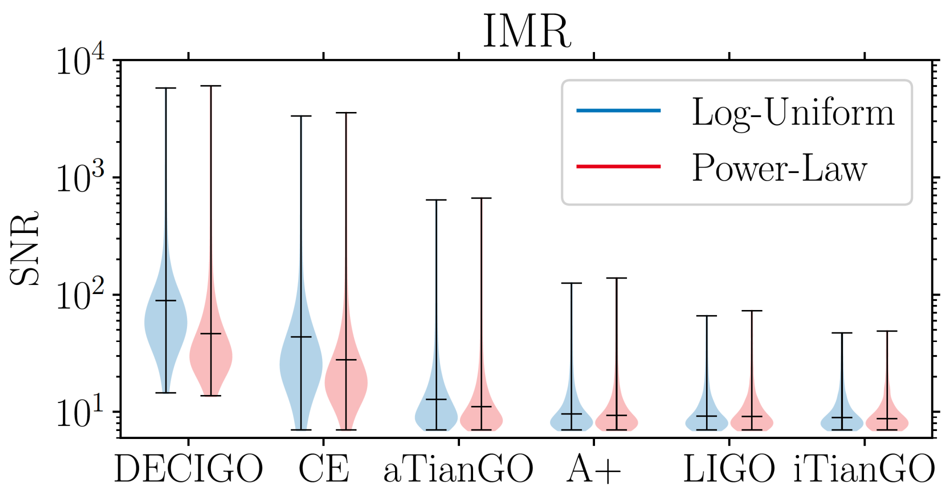

Figure 2.5: Sky-averaged SNR distributions for the IMR signal for detectors DECIGO, CE, TianGO (initial and advanced), A+, and LIGO. Horizontal lines centered on violin distributions represent medians.

ity densities for the intrinsic masses of the black hole binaries is assumed. The probability densities are a log-uniform distribution $p \propto m_1^{-1} m_2^{-1}$ and a power-law (Salpeter) distribution $p \propto m_1^{-2.35}$, which is uniform in m_2. Here m_1 is treated as the primary with $m_1 \in (m_{\min}, m_{\max})$ and $m_2 \in (m_{\min}, m_1)$ where $m_{\min} = 5 M_\odot$ and $m_1 + m_2 \leq 100 M_\odot$. The signal-to-noise ratio (SNR) is restricted to a cutoff of 7. The redshift z is sampled from a uniform comoving volume without a specific star formation rate assumed and all binaries are coalescing in 10 years. Figure 2.5 represents IMR SNR distributions for this sampling with $\sim 10^6$ realizations.

Weak-Field and Dispersion Constraints

The analysis employs the Fisher matrix approach, where the covariance matrix is the inverse of the Fisher matrix: $\Gamma_{ij} = (\partial h/\partial\theta_i|\partial h/\partial\theta_j)$. The parentheses representing the noise-weighted inner-product with respect to the spectral noise density of each detector. Here the parameter space is a combined physical parameter space $\vec{\theta}_{\text{phys}} = \{\mathcal{M}, \eta, d_L, t_c\}$ and a beyond-GR (bGR) parameter that can be mapped to a particular theory: Brans-Dicke (BD) parameter ω_{BD}, graviton mass m_g, and Einstein-Dilaton-Gauss-Bonnet (EDGB) parameter α. In a theory agnostic approach the GR correction is varied from Post-Newtonian (PN) order -1.0 to 3.0 with a general parameterized post-Einstenian (ppE) parameter β as the GR correction. Implementation of the Fisher approach is implemented acknowledging its limitations, e.g., the contributions of higher-order derivative terms in low-SNR detections that are sensitive to the asymmetries and side lobes of the estimator distribution. A more detailed study of this effect in the context of testing relativity will be addressed in Ch. 3. Note that all estimates and SNR calculations are sky-averaged as discussed in Ch. 1.

In this study the amplitude modification is fixed $A_{\mathrm{bGR}} = 0$ and considers dephasing only. Such beyond-GR models can include massive graviton, BD, and the even-parity sector of quadratic modified gravity, where EDGB is used. For each case,

$$\Psi_{\mathrm{MG}} = \bar{m}_g^2 \frac{\pi}{(1+z)f}, \tag{2.3}$$

$$\Psi_{\mathrm{BD}} = -\frac{5}{3584} S^2 \eta^{2/5} \omega_{\mathrm{BD}}^{-1} (\pi \mathcal{M} f)^{-7/3}, \tag{2.4}$$

$$\Psi_{\mathrm{EDGB}} = -\frac{5\pi}{448} \mathcal{M}^{-4} \eta^{-6/5} (1-4\eta) \alpha^2 (\pi \mathcal{M} f)^{-7/3}. \tag{2.5}$$

Including factors of h and c the effective graviton mass is $\bar{m}_g^2 = cD_0/\lambda_g^2$ or $E_g = hc/\lambda_g$, where λ_g is the graviton wavelength and E_g its associated energy. Here D_0 is the modified distance measure that scales the effective mass of the graviton constraint which also differs from the luminosity distance by a weighted redshift factor. In the BD correction there are additional "sensitivity parameters" where $S^2 = (s_1 - s_2)^2$. Each $s_{1,2}$ measures the body's inertial mass variation with the local value of the effective gravitational constant. For BHs $s_{\mathrm{BH}} = 0.5$ and for NSs $0.2 \leq s_{\mathrm{NS}} \leq 0.3$. Thus, implementing theory agnostic ppE parameters means the translation to theory specific models entirely depends on the system simulated. For example two black holes cannot constrain BD dephasing in this binary. Similarly, equal mass systems cannot constrain EDGB gravity.

In this first study of a $(\beta_{\mathrm{ppE}}, b_{\mathrm{ppE}})$ parameter space, the value of b_{ppE} is varied and β_{ppE} is fixed to its GR value of $\beta_{\mathrm{ppE}} = 0$. Figures 2.6 and 2.7 display the results for the same $\sim 10^6$ realizations of the same mass distribution models for DECIGO, CE, and TianGO as simulated in figure 2.5. Solid lines in the cumulative distribution functions (CDF) represent power-law mass sampling while dashed lines represent log-uniform mass sampling. Generally, at low PN-orders the ground-based detector CE performs poorly at constraining ppE parameter β_{ppE}. Transitioning from PN-order 0.0 to 0.5 the errors impact the distributions of chirp mass $\mathcal{M}$, which accounts for the growing separting between kilohertz and decihertz constraints on β_{ppE}. As the PN-order correction grows the trend from PN-orders 1.5 to 3.0 result in decihertz detectors outperforming ground-based detector CE despite the separation in the SNR distributions between CE and TianGO displayed in figure 2.5.

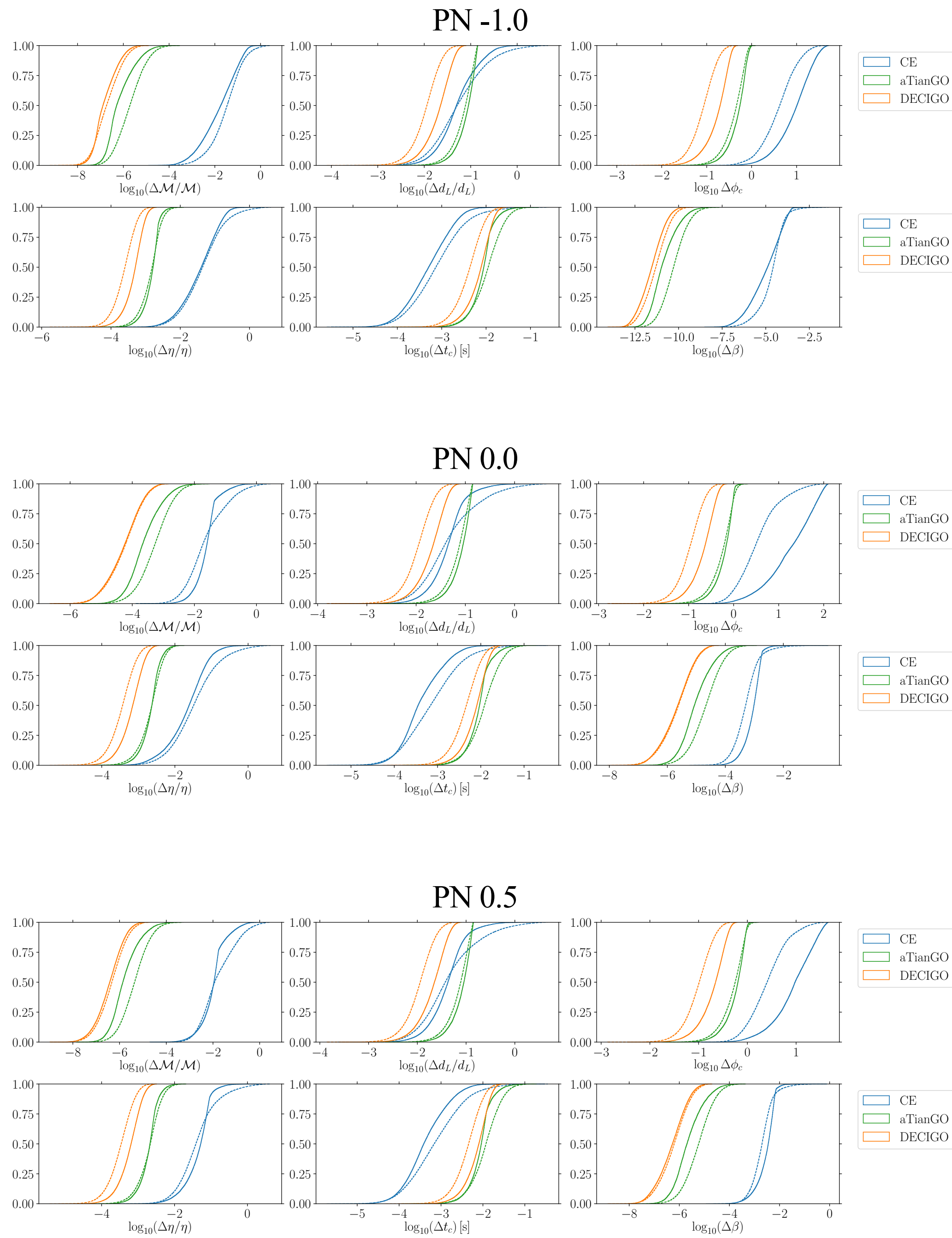

Figure 2.6: Cumulative distribution functions (CDF) plots of Fisher error estimates for physical parameters and ppE parameter β at PN-order $-1.0, 0.0$ and 0.5. Solid lines are sampled from a power-law (Salpeter) mass distribution and dashed are from a log-uniform mass distribution. All estimates are sky-averaged.

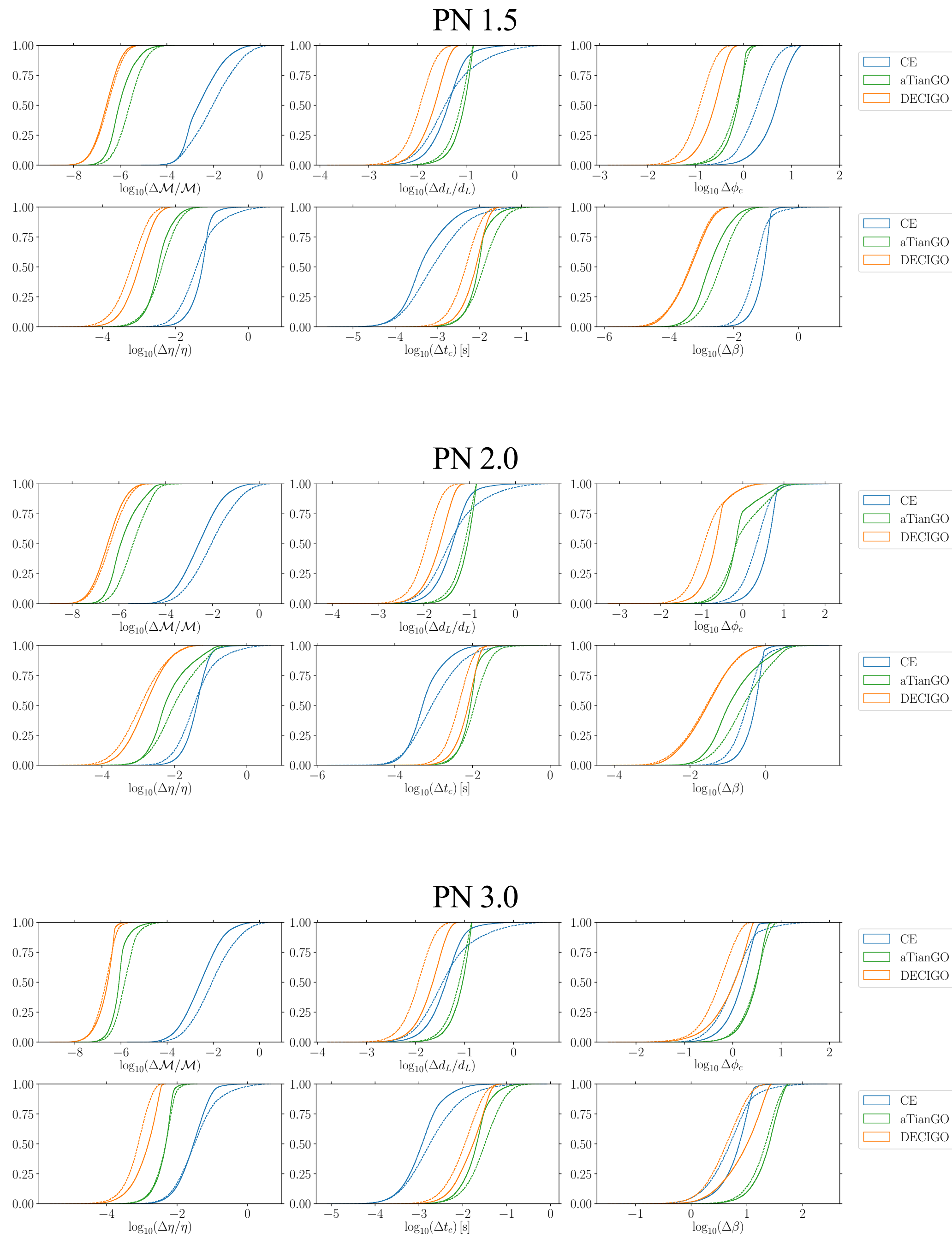

Figure 2.7: Cumulative distribution functions (CDF) plots of Fisher error estimates for physical parameters and ppE parameter β at PN-order $1.5, 2.0$ and 3.0. Solid lines are sampled from a power-law (Salpeter) mass distribution and dashed are from a log-uniform mass distribution.

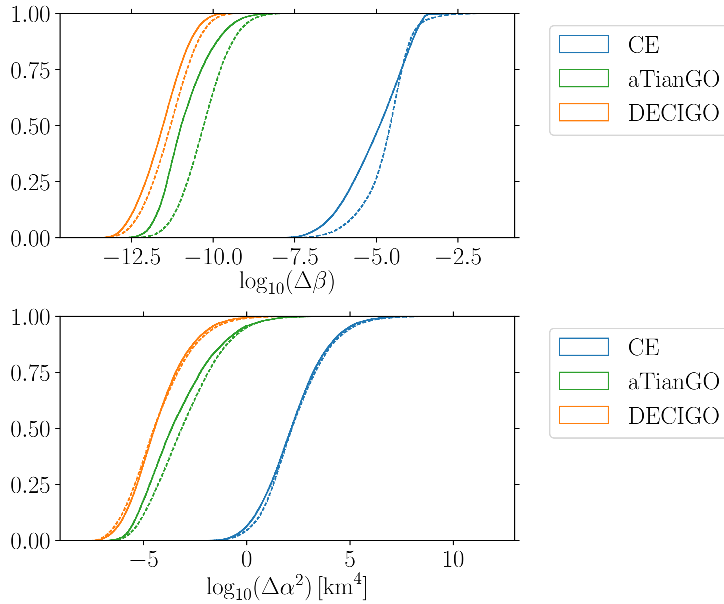

Figure 2.8: Cumulative distribution functions (CDF) of direct translation of PN-order -1.0 dephasing constraint to a theory specific parameter. Top panel is ppE parameter β at $b = -7$. Bottom panel is EDGB parameter α is computed for this term. Again, solid lines are sampled from a power-law (Salpeter) mass distribution and dashed are from a log-uniform mass distribution.

For direct translation to theory specific models in this example figure 2.8 displays the particular PN-order -1.0 distribution with a direct conversion to an EDGB constraint. As displayed in figures 2.6 and 2.7 decihertz detectors outperform ground-based detectors at low-PN orders. This is a common feature, where high-curvature black holes dynamics perform well at high-PN orders but their performance underperform at low-PN orders. Note that PN-order 1.0 distributions are not displayed, they will be used and interpreted further in Ch. 6. Their absence does not takeaway from the analysis of the trend observed in figures 2.6 and 2.7. Ch. 3 further investigates the error analysis routine implemented in this study, particularly results with low-SNR detection.

References

[1] R. A. Hulse and J. H. Taylor, ApJL **195**, L51–L53 (1975).

[2] B. P. Abbott *et al.* (LIGO and Virgo Scientific Collaboration), PRL **116**, 221101, `10.1103/PhysRevLett.116.221101` (2016).

[3] B. P. Abbott *et al.* (LIGO Collaboration) (LIGO Scientific Collaboration and Virgo Collaboration), PRD **100**, 104036, `10.1103/PhysRevD.100.104036` (2019).

[4] B. P. Abbott *et al.* (LIGO Collaboration) (LIGO Scientific Collaboration and Virgo Collaboration), PRD **103**, 122002, `10.1103/PhysRevD.103.122002` (2021).

[5] B. P. Abbott *et al.* (LIGO Collaboration), arXiv e-prints, arXiv:2112.06861 (2021).

[6] B. P. Abbott *et al.* (LIGO Collaboration), ApJL **848**, L13, `10.3847/2041-8213/aa920c` (2017).

[7] B. P. Abbott *et al.* (LIGO Scientific Collaboration and Virgo Collaboration), PRL **123**, 011102, `10.1103/PhysRevLett.123.011102` (2019).

[8] C. M. Will, LRR **17**, 4, `10.12942/lrr-2014-4` (2014).

[9] C. W. Misner, K. S. Thorne, and J. A. Wheeler, *Gravitation* (1973).

[10] N. Yunes and F. Pretorius, PRD **80**, 122003, `10.1103/PhysRevD.80.122003` (2009).

[11] N. Yunes and X. Siemens, LRR **16**, 9, `10.12942/lrr-2013-9` (2013).

[12] A. Nishizawa, PRD **97**, 104037, `10.1103/PhysRevD.97.104037` (2018).

[13] C. de Rham, LRR **17**, 7, `10.12942/lrr-2014-7` (2014).

[14] S. Perkins and N. Yunes, CQG **36**, 055013, `10.1088/1361-6382/aafce6` (2019).

Chapter 3

APPLICATIONS AND LIMITATIONS OF FISHER ERROR ESTIMATION WITH APPLICATION TO BEYOND-GR THEORIES

In this chapter we quantify the capability of laser interferometers to detect violations of general relativity (GR), with a single detection of a compact binary coalescence signal, by assessing if the minimal error on the parameterized post-Einsteinian (ppE) parameters are larger than the separation of modified gravity values with respect to standard GR values. Error bounds are computed with the most accurate frequentist approach to date by computing the errors as inverse power series in the signal-to-noise ratio (SNR), where the first order is the inverse of the Fisher information matrix [1–3]. In this chapter we model GR violations with the ppE framework [4–8], which produces parametrized extensions of GR GW signals for the inspiral phase only of a binary compact coalescence in the absence of spin (similar extensions are currently not available for the merger and ringdown phase).

The square root of the inverse Fisher matrix diagonal elements, also known as the Cramér-Rao Lower Bound (CRLB), is a lower limit in the error of any unbiased estimator in the absence of prior knowledge. In this regard the CRLB is a statement about the amount of information available in the data regardless of the specific parameter estimation scheme. There is however no guarantee that any estimator is capable to actually attain the CRLB for part or the whole range of values the physical parameters can assume. Also, the CRLB only takes into account the curvature of the probability distribution of the data around the true value of the parameters and therefore does not include the role of secondary maxima in the calculation of the variance or mean square error of the estimators. The improved bound adopted here (based on second order asymptotics) is larger than the inverse Fisher matrices, known to underestimate errors in low-SNR detections. Second-order bounds have been previously used for compact binary coalescence waveforms in quantifying the accuracy in intrinsic parameters as well as the direction of arrival for a network of laser interferometers [1–3].

The benefits of using the second order of the expansions is in the fact that they depend up to the fourth derivative of the likelihood function and, therefore, are sensitive to asymmetries and side lobes of the estimator probability distribution (similar to the change in the accuracy of a Taylor expansion when extended to higher orders). Also, in the past [1–3], the comparison of the second order with the first order provided an analytical understanding of the reasons the CRLB could not be met (for example, in Ref. [1], a novel relationship between the Kurtosis of the probability distribution of the estimator and the SNR was derived to understand when the CRLB could be met).

Bayesian methods were recently applied to test modified GR signals through consistency tests [9, 10], and the ppE framework [11]. Refs. [9, 10] developed a framework to detect GR violations without modeling the violation, this works in the limit of large number of detections. Bayesian selection methods were also used in Ref. [11] and Ref. [12] to constrain the range of ppE parameter values, provided that priors are adopted.

When Bayesian uncertainties are smaller than the frequentist bounds, it means that the parameter estimation errors depend critically on the priors. This issue can be an artifact if the prior is not based on previous detections or no robustness studies were performed with respect to the choice of the priors. In this chapter, we show that this instance happens for an equal-mass binary black hole system in the massive graviton case. This example illustrates how the present work provides a unique understanding of the parameter estimation errors. Although GW150914 had a SNR~ 24, its inspiral stage falls within the prescribed study of SNR< 20. [1]

In addition, this work extends the Fisher information based results of Ref. [6–8], which perform error estimations by modifying PN coefficients. We also extend Fisher-based assessments of specific alternative theories [13–17]. Specifically, this chapter considers phase modification in the *restricted* ppE framework [5], considering the ppE framework as a general enhancement to existing `TaylorF2` GR templates in a three detector LIGO-Virgo network. Calculations in this limit were chosen since deformations to the GW's phase are expected to be more resolvable [11, 18] and complements recent Bayesian methods testing deviations from GR [9, 10]. Second-order frequentist constraints produced in this chapter are at the same order of magnitude as the Bayesian model selection's errors in Ref. [11], where our errors are quantified at the one sigma level. As error estimates of ppE parameters grow, second-order errors of parameters such as the chirp mass, symmetric mass ratio, and time of coalescence also inflate. The results presented here, and the rescaled

[1] GW150914 has inspiral SNR~ 12.

bonds which can be simply derived by changing the SNR, will be important benchmarks for any parameter estimation scheme which will be used in existing and future interferometer data, including Bayesian parameter estimation algorithms.

3.1 Three Detector Network

Masses of each compact body are labeled as $m_{1,2}$, the total mass being $M = m_1 + m_2$ with $v = (\pi M f)^{1/3}$ and $\eta = m_1 m_2 / M^2$ as the reduced mass frequency and symmetric mass ratio, respectively. The usual chirp mass is $\mathcal{M} = \eta^{3/5} M$. Geometrized units ($G = c = 1$) are also employed. Terms labeled with I indicate a particular quantity for that I-th detector, e.g., s^I is a signal received at some I-th detector, ρ^I is a detector-dependent SNR, etc. Finally, the detectors considered are those for Adv. LIGO and Adv. Virgo, so we have $I = H, L, V$ for the respective advanced interferometers in Hanford USA, Livingston USA, and Cascina Italy. Quantities summed over I indicate the total network contribution of that term, e.g., network SNR, network Fisher matrix.

To discuss some of the terms appearing later: τ_I is a time lag parameter accounting for the delay in the waveform's propagation from the I-th detector frame (IDF) to some fiducial frame (FF),[2] with μ^I and Φ_0^I being coefficients that depend on the inclination angle ϵ of the binary system and the generalized antenna patterns $\mathcal{F}^I_{+,\times}$ of each detector. These are represented by,

$$\tau_I = \hat{\mathbf{n}} \cdot (\mathbf{r}_I - \mathbf{r}_{FF}), \tag{3.1}$$

$$\mu^I = \left(\left(\frac{1}{2} \mathcal{F}^I_+ (1 + \cos^2 \epsilon) \right)^2 + \left(\mathcal{F}^I_\times \cos \epsilon \right)^2 \right)^{1/2}, \tag{3.2}$$

$$\Phi_0^I = \arctan \frac{2 \mathcal{F}^I_\times \cos \epsilon}{\mathcal{F}^I_+ (1 + \cos^2 \epsilon)}, \tag{3.3}$$

with $\hat{\mathbf{n}}$ the direction of travel of the waveform, $\mathbf{r}_I$ the distance to the I-th detector (i.e., the IDF origin), and $\mathbf{r}_{FF}$ the distance to the FF origin. Reasons for construction of a frame of common origin is due to the feasibility and efficiency displayed in calculations of quantities in particular frames. Notion of a common origin between the frames is valid since approximative measures[3] allow the origins of the coordinate systems to coincide. With respect to Ref. [3] the frames are established as the already

[2] FF is the frame in which the origins are referenced to coincide.

[3] Through reasonable assumption of zero curvature over the course of the GW's propagation and introduction of time lag τ_I.

mentioned IDF and FF, with a third frame called the wave-frame (WF).[4] In producing calculable quantities the frames are then fixed to values of that in the Earth frame (EF).

Since the origins of the frames coincide transformation between the frames is feasible through simple Eulerian angles with the usual ZXZ convention. From this, a set of Euler angles (ϕ, θ, ψ) converts a quantity from the FF into the WF and another set $(\alpha^I, \beta^I, \gamma^I)$ converts from the FF into the IDF through the usual rotation matrices. Here angle ψ is the polarization angle. A variety of relations can be uncovered after defining a few new angles. Let angle pairs (Φ, Θ) and (long, lat) describe the sources location in the sky (the former being in spherical coordinates and the latter in longitude-latitude coordinates), let (Ξ, ζ) be defined from projections of $\hat{\mathbf{n}}$ onto the FF's axis, define angles (Ω^I, Υ^I) so that they prescribe the location of the I-th detector with respect to the FF, and allow angle Δ^I to span the region between the first detector arm (in the IDF) and the local northern direction. These relations are summarized as follows:

$$\begin{aligned} \phi &= \Phi - \frac{\pi}{2} = \text{long} - \frac{\pi}{2} = \Xi + \frac{\pi}{2} \\ \theta &= \pi - \Theta = \frac{\pi}{2} + \text{lat} = \zeta \end{aligned} \tag{3.4}$$

and

$$\alpha^I = \Omega^I + \frac{\pi}{2}, \quad \beta^I = \frac{\pi}{2} - \Upsilon^I, \quad \gamma^I = \Delta^I + \frac{\pi}{2}. \tag{3.5}$$

Formulation of $\mathcal{F}^I_{+,\times}$ into a symmetric-trace-free base has been performed, with respect to the Eulerian angle dependence, and what surfaces in the frequency represented signal are the two generalized antenna patterns:

$$\begin{aligned} \mathcal{F}^I_+ &= \frac{1}{2}\Big(T_{2s}(\alpha^I, \beta^I, \gamma^I) + T_{-2s}(\alpha^I, \beta^I, \gamma^I)\Big) \\ &\quad \times\Big(T^*_{2s}(\phi, \theta, \psi) + T^*_{-2s}(\phi, \theta, \psi)\Big) \end{aligned} \tag{3.6}$$

$$\begin{aligned} \mathcal{F}^I_\times &= \frac{i}{2}\Big(T_{2s}(\alpha^I, \beta^I, \gamma^I) + T_{-2s}(\alpha^I, \beta^I, \gamma^I)\Big) \\ &\quad \times\Big(T^*_{2s}(\phi, \theta, \psi) - T^*_{-2s}(\phi, \theta, \psi)\Big) \end{aligned} \tag{3.7}$$

where T_{mn} are second-order Gel'fand functions (T^*_{mn} being their complex conjugates). Function statements, such as $f(\alpha^I, \beta^I, \gamma^I)$ and $g(\phi, \theta, \psi)$, represent their

[4] Determined through the GW's direction of travel and orthonormal WF unit vectors along its axis, where dominant harmonic polarizations in the waveform is assumed

dependencies on Euler angle rotations from $FF \to IDF$ and $FF \to WF$, respectively. See Ref. [3] for exemplary calculations. Note that an auxiliary ppE template has been developed that considers extra polarizations of waveforms produced in non-GR gravity, incorporating additional propagating degrees of freedom in the ppE framework [19]. Although it is of interest to measure extra polarizations expected in a variety of alternative theories of gravity, these extra modes lead to more complex models. For initial analysis of modified gravity through the asymptotic maximum likelihood estimator approach a ppE template, with only the standard two propagating modes, is considered both sufficient and satisfactory for now. Ref. [20] investigated methods to test non-GR polarizations via continuous waveforms from asymmetric pulsars.

3.2 Inspiral Signal with ppE

The waveforms are assumed to be produced by a nonspinning binary system with all orbital eccentricity information lost when entering the frequency bandwidth of Adv. LIGO and Adv. Virgo. Fourier transform of the signal, through stationary phase, becomes,

$$s^I_{\mathrm{GR}}(f) = A^I_{\mathrm{GR}}(f) e^{i\left(\psi_{\mathrm{GR}}(f) - 2\pi f \tau_I - \Phi^I_0\right)}, \quad f < f_{\mathrm{merg}} \tag{3.8}$$

for the inspiral stage of the compact binaries. For the phase $\psi_{\mathrm{GR}}(f)$ and amplitude $A^I_{\mathrm{GR}}(f)$ the standard `TaylorF2` model is used.

The signal of a collection of alternative theories of gravity is modelled as (3.8) modulated in the phase and amplitude as:

$$\begin{aligned} A^I_{\mathrm{GR}}(f) &\to A^I_{\mathrm{GR}}(f)\,(1 + \delta A(f)), \\ \psi_{\mathrm{GR}}(f) &\to \psi_{\mathrm{GR}}(f) + \delta\psi(f), \end{aligned} \tag{3.9}$$

where $\delta A(f)$ and $\delta\psi(f)$ are a general series of scaling parameters $\alpha_i, \beta_i \in \Re$ and in some instances arguments call for integer exponentials of $v\eta^{1/5}$ [19, 21], where $v = (\pi M f)^{1/3}$ for total mass M and $\eta = m_1 m_2/M^2$. Here the analysis is done at leading order in the ppE parameters,

$$\begin{aligned} \delta A_{\mathrm{ppE}}(f) &= \alpha(v\eta^{1/5})^a, \\ \delta\psi_{\mathrm{ppE}}(f) &= \beta(v\eta^{1/5})^b, \end{aligned} \tag{3.10}$$

At each interferometer the signal is assumed to be recorded with additive noise as in Ref. [3]. Frequency dependent noise for Adv. LIGO and Virgo are interpolated from the official power spectral density. For error analysis, and upcoming integrations, the lower cutoff frequency is set to $f_{\rm low}$ and the upper cutoff is set to the upper limit for reliability in the inspiral of the waveform template, i.e., the innermost stable circular orbit (ISCO) frequency,

$$f_{\rm low} = 20 \text{ Hz} \ , \quad f_{\rm up} = f_{\rm ISCO} \approx (6^{3/2}\pi M)^{-1}.$$

For non-spinning systems thirteen parameters are necessary in the description of the inspiral of two coalescing binaries: two mass terms, four angles (two source location and two waveform angles), two coalescence parameters, distance to the source, and four ppE parameters in the leading order approximation. Singular Fisher matrices might appear [1, 22], indicating that the resolvable parameter space is smaller (where the Fisher matrix approach can still be used).

The distance D_L is excluded from the error estimates because the amplitude has a dependency on both mass and distance parameters, and the independent treatment of both is unresolvable as already indicated in Ref. [3]. The coalescence phase is also not included because estimations of ϕ_c is relevant only when a full waveform (inspiral, merger, and ringdown) is implemented. The polarization ψ is excluded because results tend to be independent of it [3].

Derivatives of the fitting factor (FF) [18],

$$FF = \max_{\vec{\zeta}} \left(\frac{\langle s_1(\vec{\lambda}) | s_2(\vec{\zeta}) \rangle}{\sqrt{\langle s_1(\vec{\lambda}) | s_1(\vec{\lambda}) \rangle} \sqrt{\langle s_2(\vec{\zeta}) | s_2(\vec{\zeta}) \rangle}} \right) \tag{3.11}$$

with respect to the binary's inclination ϵ evaluated at, or in a neighborhood of, $\epsilon = 0$ are roughly zero leading to impossibility to estimate ϵ and singular Fisher matrices. Here the $\langle \cdot | \cdot \rangle$ represent noise weighted inner products and $s_{1,2}$ are GW signals controlled by general parameter space vectors $\vec{\lambda}$ and $\vec{\zeta}$. Keeping other parameters fixed and varying only ϵ produces change in the SNR equivalent to the rescaling of the distance, which affects GW plus-cross polarizations similarly. Top panel in figure 3.1 shows the sky-averaged SNR plotted as a function of inclination ϵ (only the GR polarizations are considered). Also, sky patterns of the errors remain consistent when varying ϵ. Therefore, since ϵ is degenerate with D_L it is also excluded from our resolvable parameter space, which becomes $\theta^i_{\rm phys} = \{\eta, \log \mathcal{M}, t_c, \text{lat}, \text{long}\}$.

Throughout this chapter amplitude modulations are to be held fixed to that of GR: $\alpha = 0$, because the same effect could be produced by changing physical parameters

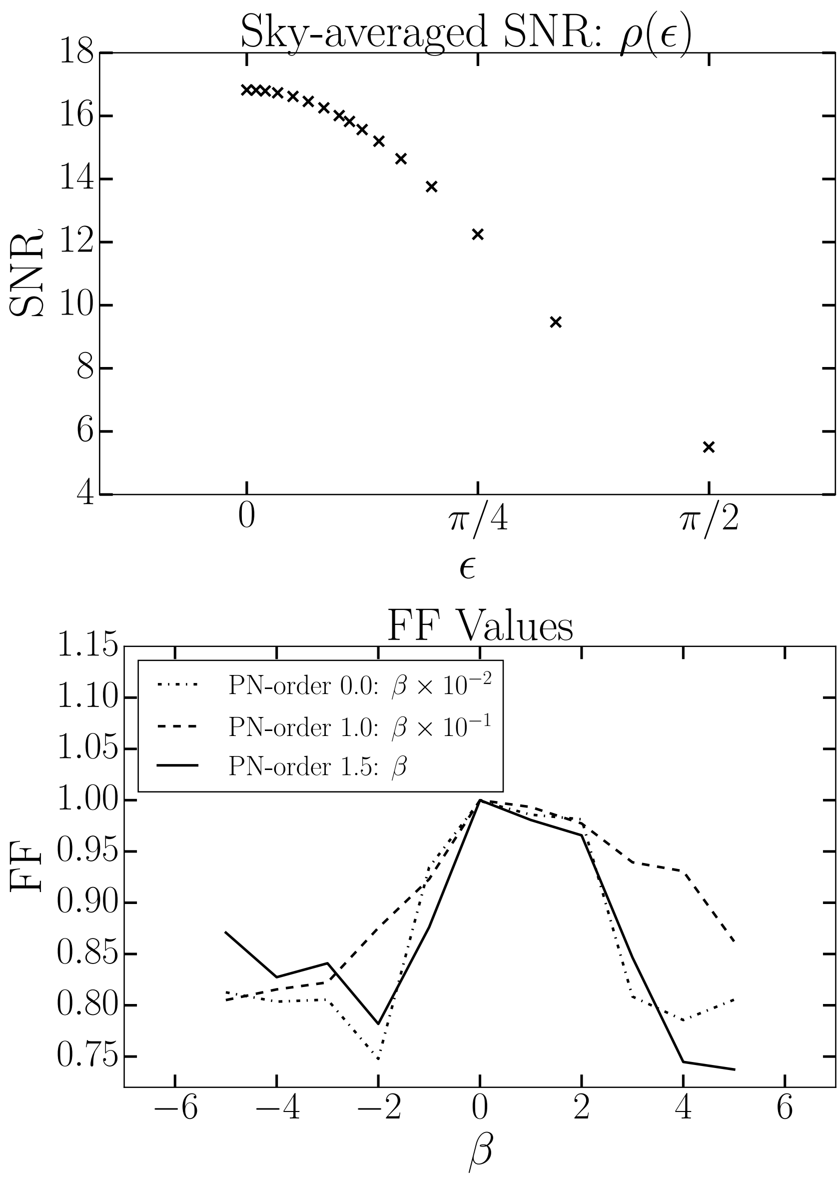

Figure 3.1: Inspiral SNR and Fitting factor calculations. Top: Sky-averaged SNR plotted with inclination varied for system parameters: $m_1 = m_2 = 10M_\odot, t_a = \phi_a = 0, \beta = -0.2, D_L = 1100$ Mpc, and $b = -3$ in the three detector network. Bottom: Fitting factors (3.11) for a range of β with b fixed to produce PN-order 0.0, 1.0, and 1.5 modifications for a system of: $m_1 = m_2 = 10M_\odot$ and $t_a = \phi_a = 0$. Adv. LIGO noise is assumed. Since the range of β-values scale differently at each PN-order, each β-interval is scaled (as labeled in the legend). For example, in the PN-order 0.0 modification the β values in the domain are each scaled by 10^{-2}.

like distance or mass. Such an approach supposes that GR-violating amplitudes in the waveform are suppressed or modifications manifest only in waveform propagation.[5] Also, recent work suggests that GR modifications produced during the generation of a waveform can be disentangled from that produced during propagation [19], thus, in the event that phase deformation dominates GR-violating effects, amplitude modifications can be disregarded. Calculations in this restricted framework are performed with modifications at various PN-orders in the phase, where in the strong-field regime discrete values of b controls what PN-order correction is constituted for free parameter β (GR result: $\beta = 0$).

A qualitative way to study the influence of ppE parameters (β, b) on a GR signal can be obtained through the correlation of the signals by means of the fitting factor (3.11). Each integration is done from 20 Hz to f_{ISCO} with the noise curve of Adv. LIGO. Our exact waveform s_1 is represented by a `TaylorF2` waveform, whereas, a modified-`TaylorF2`, formed through (3.9) and (3.10), acts as s_2. So $\vec{\lambda}$ is the GR-limit parameter space vector and $\vec{\zeta}$ is that of the ppE parameter space. The inner products are maximized over evenly spaced parameters $\vec{\zeta}$ to provide a FF-value, where $FF = 1$ represents an exact match between signals. Both `TaylorF2` models are kept to PN-order 3.5 in the phase. In the denominator of (3.11), amplitude parameters normalize to leave $f^{-7/3}/S_h$ in each integrand. The numerator retains integrand $(f^{-7/3}/S_h)e^{i\Delta\psi(f;\vec{\lambda},\vec{\zeta})}$, where,

$$\Delta\psi(f;\vec{\lambda},\vec{\zeta}) = \psi(f;\vec{\lambda}) - \psi(f;\vec{\zeta}) - \delta\psi_{\mathrm{ppE}}(f)$$

and, in fixing b and varying β, the parameters needing to be maximized over are $\vec{\zeta} = \{t_c, \phi_c, \eta, M_{\mathrm{tot}}\}$. Parameters are evenly spaced, in a $30 \times 30 \times 30 \times 30$ grid, within intervals: $0.05 \le \eta \le 0.25$, $0.5M_{\mathrm{tot}} \le M_{\mathrm{tot}} \le 1.5M_{\mathrm{tot}}, -\pi \le \phi_c \le \pi$, and $-1.3 \times 10^{-2} \le t_c \le 1.3 \times 10^{-2}$.

Figure 3.1 displays the results for an equal-mass system of $m_1 = m_2 = 10M_{\odot}$ and $t_a = \phi_a = 0$ for PN-order 0.0, 1.0, and 1.5 modifications in the waveform. Parameters $\vec{\zeta}$ are maximized over for a variety of β-values. Note that at lower PN-orders the interval of β is scaled differently than the $-5 \le \beta \le 5$ depicted, an interval valid for PN-order 1.5 modifications. The general trend is that the fitting factor is less affected by β for larger PN-order with a skew in the FF-distribution towards the positive domain of β-values.

[5] Modifications to just propagation could surface through alterations in the dispersion of the GW, with alterations stemming from waveform generation excluded [14, 17]. Past studies also indicate modulations are most sensitive to phase modulations [11, 18].

3.3 Restricted ppE Template

As stated, variations of β are restricted to fixed PN-order corrections in the phase. For the two-dimensional study b is fixed to induce modifications at (separately) PN-orders 0.0, 0.5, 1.0, 1.5, 2.0, and 3.0 which acts as a demonstration to the error estimation procedure. Higher-dimensional studies specifically target a PN-order 1.0 modification and a weak-field $b = -7$ modification to address dispersion modification and dipole gravitational radiation. From this reason β is varied with error estimations performed at each β-value. In Ref. [23] an analysis of binary pulsar PSR J0737-3039 [24] placed bounds on ppE parameters (for this binary $4\eta \approx 1$ as determined from radio pulsar measurements [24]). At PN-order 2.5 ($b = 0$) degeneracies occur with other fiducial parameters, thus is not considered in the analysis. In some theories constraints for $b = -7$ cannot be implemented from pulsar measurements, due to β's dependence on mass differences of the system and other theoretical parameters which will be discussed shortly. With the exception of $b = -7$, parameters that probe weak-field ($b < -5$) are not considered since they are better constrained via binary pulsar measurements [11].

At $b = -7$, the even-parity sector of quadratic modified gravity (QMG), an example being Einstein-Dilation-Gauss-Bonnet (EDGB) gravity, can be explored. For even-parity QMG, the violating term for a BBH system depends on the mass differences of the BHs: $\beta \propto \zeta_3 \eta^{-18/5}(1 - 4\eta)$, unresolvable for equal-mass systems [25]. For BHNS systems, the violating coefficients depend on the ratio of the two bodies: $\beta \propto \zeta_3 \eta^{-8/5}(m_{\rm NS}/m_{\rm BH})^2$ due to the 'scalar charge' vanishing in NSs [25, 26]. With this same $b = -7$ correction, examples of dipole gravitational radiation, like Brans-Dicke (BD), can also be assessed. Here BD-like modifications further depend on the difference of parameters which measure the body's inertial mass variations with respect to the local background value of the effective gravitational constant. These so-called 'sensitivity parameters' $s_{\rm BH,NS}$ are generally set to 0.5 for black holes, so their difference vanish for a BBH system. Only a BHNS system would allow constraints of BD-like modifications since $0.2 \leq s_{\rm NS} \leq 0.3$ [27–30].

For corrections at $b \neq -7$, most existing modifying coefficients depend on parameters that either vanish in the non-spinning model (3.8) or contribute beyond PN-order 3.5. This is the case in specific models of QMG, e.g., the odd-parity sector and dynamical Chern-Simons (CS) gravity [25]. As an example, in the circular inspiral of two comparable mass BHs the GR-deviating term of dynamical CS has dependencies on the BH spins $\hat{S}_{1,2}$ and their relations to their orbital angular momentum $\hat{L}$: $\delta C = \delta C(m_{1,2}, \hat{S}_{1,2}, \hat{L})$ [31]. When the binary system is non-spinning, modifications are beyond PN-order 3.5.

Beyond modifications during waveform generation, two propagating effects are massive graviton (MG) and simplified versions of Lorentz-violating (LV) theories [14, 17]. Parameters to constrain are the graviton Compton wavelength λ_g and $\lambda_{\rm LV} = 2\pi\mathbb{A}^{1/(\gamma-2)}$. Here $\mathbb{A}$ is a phenomenological parameter modifying the gravitational waveform's dispersion relation. The γ-dependent distance measure D_γ (see Ref. [17] for exact formula) further depends on known astrophysical parameters (Hubble parameter, matter density parameter, etc.). Parameter γ governs the order of correction and $\gamma = 0$ (PN-order 1.0) is what we're limited to since this is the only value contained in the ppE framework for the PN-order 3.5 `TaylorF2` model. Such MG-LV interpretations are generic models modifying the dispersion of a GW with more specific generation mechanism still yet to be explored. Ref. [9] notes some limitations in prescribing MG effects as modifications of the dispersion of the waveform. In LV-type modification further work in existing, model-independent approaches, e.g., the Standard Model Extension [32, 33], could be interesting (see for example Ref. [34]).

Constraints have been imposed on the wavelength of the graviton. The detection of GW150914 and binary-pulsar constraint serve as dynamical bounds while solar-system constraints, serving as static bounds, provide the most reliable estimates [35]. So, parameters are represented by,

$$\lambda_{\rm LV} = 2\pi\mathbb{A}^{-1/2}, \quad \lambda_g \geq \begin{cases} 10^{13}[\text{km}], & \text{dynamic (GW)}, \\ 1.6\times10^{10}[\text{km}], & \text{dynamic (pulsars)}, \\ 2.8\times10^{12}[\text{km}], & \text{static}. \end{cases}$$

For EDGB gravity, the constraint parameter is $|\alpha_{\rm EDGB}|$. Here $\zeta_3 = \xi_3 M^{-4} = 16\pi\alpha_{\rm EDGB}^2 M^{-4}$, with $\beta_{\rm BBH} \propto \zeta_3\eta^{-18/5}(1-4\eta)$ and $\beta_{\rm BHNS} \propto \zeta_3\eta^{-8/5}(m_{\rm NS}/m_{\rm BH})^2$. In Brans-Dicke theory $\beta \propto (s_{\rm BH,NS} - s_{\rm BH,NS})^2\omega_{\rm BD}^{-1}$. From measurements of the Cassini spacecraft [36, 37] bounds on EDGB and Brans-Dicke parameters are,

$$\begin{aligned} |\alpha_{\rm EDGB}|^{1/2} &\leq 8.9\times10^6 \text{ km}, \\ \omega_{\rm BD} &> 4\times10^4. \end{aligned}$$

With other suggested constraints [26, 38] giving,

$$\begin{aligned} |\alpha_{\rm EDGB}|^{1/2} &< 1.9 \text{ km}. \\ |\alpha_{\rm EDGB}|^{1/2} &< 9.8 \text{ km}, \end{aligned}$$

GW150914 results have allowed studies to infer the theoretical significance of the testing GR study in various specific models, see for example Refs. [39, 40].

3.4 Asymptotic Expansions

Similar to Ref. [3], we reasonably assume only Gaussian noise at time of the signal and that the noise is uncorrelated at different interferometers. Here we use the analytic asymptotic expansion of the variance and bias developed in Refs. [1–3],

$$\sigma^2_{\vartheta^i} = \sigma^2_{\vartheta^i}[1] + \sigma^2_{\vartheta^i}[2] + \cdots , \tag{3.12}$$

$$b_{\vartheta^i} = b_{\vartheta^i}[1] + b_{\vartheta^i}[2] + \cdots , \tag{3.13}$$

with $\sigma^2_{\vartheta^j}$ being the diagonal elements of the covariance matrix, where

$$\begin{aligned} \sigma_{\vartheta^j}[1], b_{\vartheta^j}[1] &\propto \rho^{-1}, \\ \sigma_{\vartheta^j}[2], b_{\vartheta^j}[2] &\propto \rho^{-2}, \end{aligned}$$

for network SNR ρ. This inverse proportionality continues at higher orders in similar fashion. Here the network SNR is the sum over the square of the optimal SNR ρ^I of the signal at the I-th detector,

$$\rho^2 = \sum_I \left(\rho^I\right)^2, \quad \rho^I = \langle s^I | s^I \rangle^{1/2} \tag{3.14}$$

Notice that ρ increases for a fixed source by increasing the number of detectors. The first-order term of the expansion of the variance, the diagonal components of the inverse Fisher matrix, dominates the bound on the error in the limit of large SNR, while higher order terms become more important for medium to low SNR.

What is usually regarded as the error in a lab measurement is the square root of the mean-squared error (MSE), where the MSE is the sum of the variance (3.12) and square of the bias (3.13): $MSE_{\vartheta^i} = \sigma^2_{\vartheta^i} + b^2_{\vartheta^i}$. Since this analysis computes errors at second-order of $1/\rho$, the expression above only requires first-order of the bias which is negligible as already discussed in Ref. [3]. We estimate uncertainties of the two-dimensional ppE parameter space $\theta^i_{\rm ppE}$ for different β at a fixed exponential b. In addition, the inclusion of $\theta^i_{\rm ppE}$ to a signal's extrinsic and intrinsic parameter space $\theta^i_{\rm phys}$ is also assessed.

Finally, error bounds are indicated with,

$$\begin{aligned} \Delta\vartheta_i[1] &= \sqrt{\sigma^2_{\vartheta^i}[1]}, \qquad \Delta\vartheta_i[2] = \sqrt{\sigma^2_{\vartheta^i}[2]} \\ \Delta\vartheta_i[1+2] &= \sqrt{\sigma^2_{\vartheta^i}[1] + \sigma^2_{\vartheta^i}[2]}. \end{aligned} \tag{3.15}$$

Error Bounds (System)	PN-order 0.0	PN-order 0.5	PN-order 1.0
$\Delta\beta[1]$ (BBH 1:1)	2.70×10^{-4}	1.36×10^{-3}	6.59×10^{-3}
$\Delta\beta[1]$ (BNS)	1.29×10^{-5}	1.24×10^{-4}	1.14×10^{-3}
	PN-order 1.5	PN-order 2.0	PN-order 2.5
$\Delta\beta[1]$ (BBH 1:1)	3.07×10^{-2}	1.39×10^{-1}	2.66
$\Delta\beta[1]$ (BNS)	9.78×10^{-3}	7.93×10^{-2}	4.49

Table 3.1: Constant slopes of first-order error bound estimates of the BBH 1:1 (for SNR $\rho = 14.6$) and BHNS systems for all β values. Here percent errors [%] follow a $1/\beta$ relationship for $\Delta\beta[1]$ represented above for respective PN-orders.

For example first-order errors of the symmetric mass ratio η are marked by $\Delta\eta[1]$, second-orders are marked by $\Delta\eta[2]$, and total error with the inclusion of second-order contributions as $\Delta\eta[1+2]$.

3.5 Results

In this section we explore the error bounds both as a function of the SNR and sky location of the source. The asymptotic expansion approach is first applied to a two-dimensional ppE parameter space (when the physical parameters are known) of equal-mass systems. Only phase corrections are assumed through unknown ppE parameters (β, b), while b probes modifications at PN-orders 0.0-3.0 of the `TaylorF2` model (of a PN-order 3.5 phase). Based on Ref. [1–3] this approach is expected to give overly optimistic errors. The Fisher information error estimates presented here for the ppE parameters are at least an order of magnitude smaller than results with Bayesian model selection [11].

To identify SNR dependencies and regions of lowest error estimates the sky dependencies of errors are observed through a 289-point sky grid. A point $(\text{lat}_i, \text{long}_j)$ in latitude-longitude coordinates (of the Earth frame) on the sky grid follows from the procedure of Ref. [3] (detector coordinates also follow Ref. [3], which are fixed in the Earth Frame as given in Ref. [41, 42]).

As discussed in Section 3.2, $\epsilon = \pi/6$ is a fixed value and excluded in error analysis. Parameter ψ is also fixed and arbitrary values can be chosen for fiducial parameters ϕ_c and t_c. The sky-averaged SNR is restricted to an inspiral phase $\rho < 20$ to focus on the more likely advanced interferometer scenarios. For each system considered, the distance of the resolved signal in the network is varied to keep a fixed SNR. For a three-detector network $(I = H, L, V)$ the following is chosen for the equal-mass binary systems:

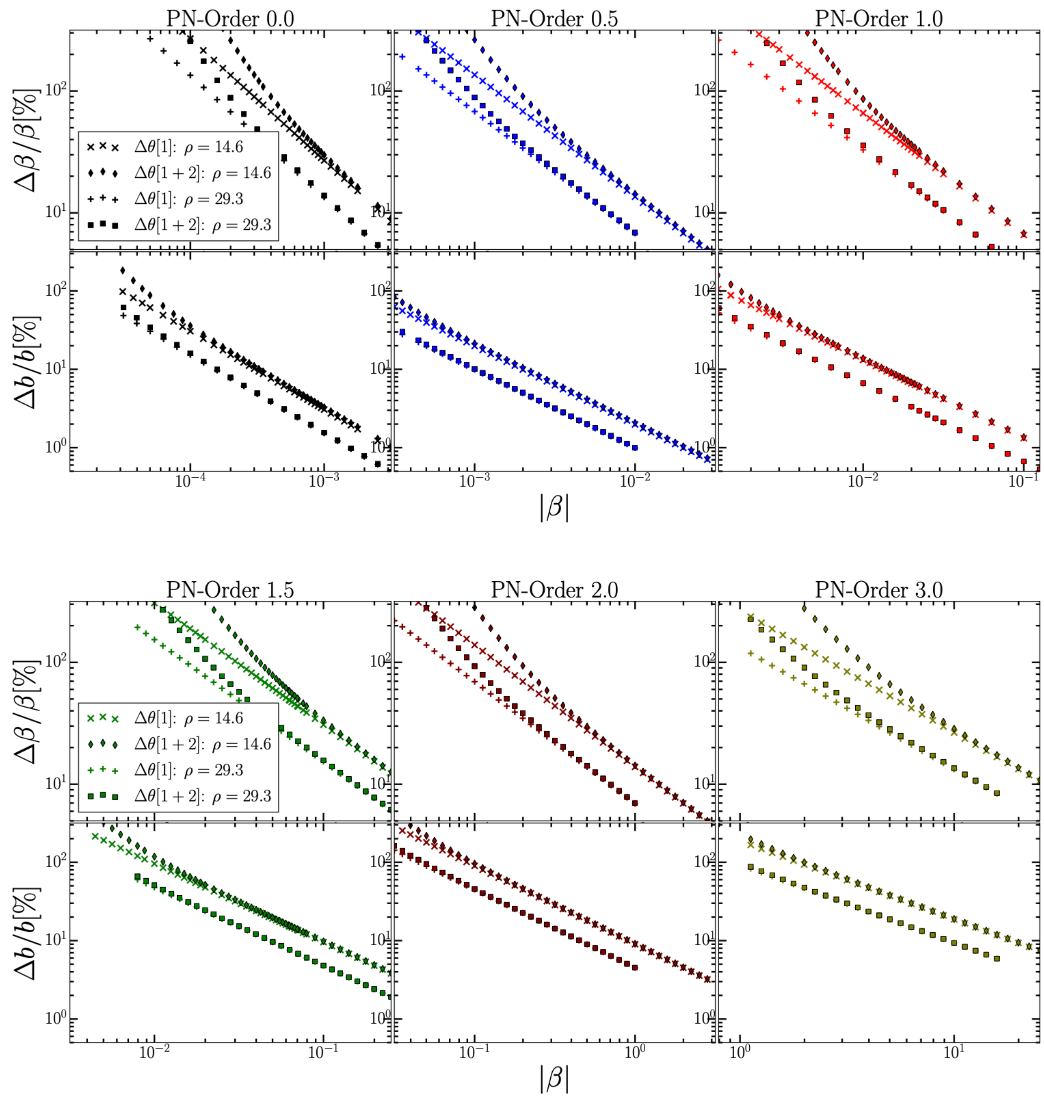

Figure 3.2: Sky-averaged errors as a function of β for a two-dimensional ppE parameter space for the BBH 1:1 system of averaged network SNR $\rho = 14.6$. SNR results of $\rho = 29.3$ are also showed by setting the distance to $D_L = 550$ Mpc. As noted in Ref. [3] error estimates are rescaled as $\sigma[1](\rho^*/\rho)$ and $\sigma[2](\rho^*/\rho)^2$, where ρ^* is the SNR that error estimates are originally calculated from. In the top panel the far left column represents each system for a PN-order 0.0 modification ($b = -5$), the center column is a PN-order 0.5 modification ($b = -4$), and far right column is for PN-order 1.0 modifications ($b = -3$). Similarly, the bottom panels are resulting modifications at PN-order 1.5 ($b = -2$), 2.0 ($b = -1$), and 3.0 ($b = +1$). β is more tightly constrained at lower PN-orders and the inclusion of second-order errors for (β, b) drastically diverge from Fisher estimates as $\beta \to 0$.

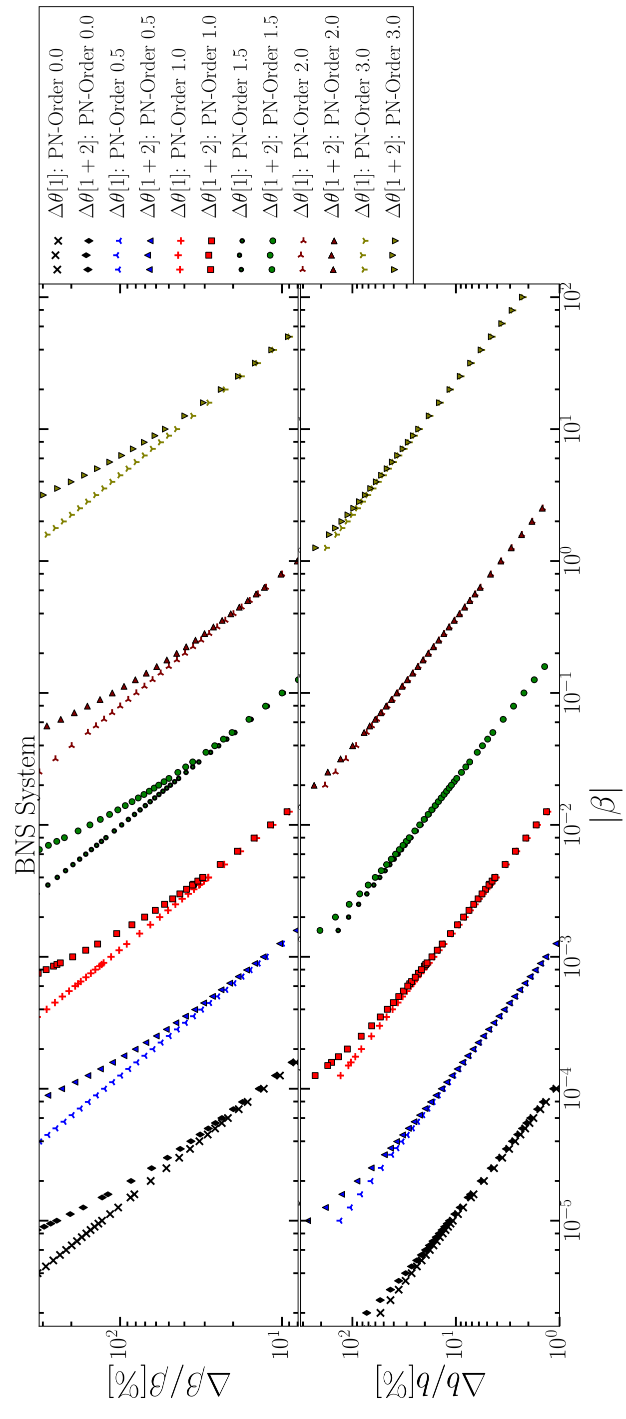

Figure 3.3: Sky-averaged errors, similar to figure 3.2, for a BNS system of averaged SNR $\rho = 17.0$.

- BBH 1:1- $(m_1, m_2) = (10, 10)M_\odot$, $D_L = 1100$Mpc,
- BNS- $(m_1, m_2) = (1.4, 1.4)M_\odot$, $D_L = 200$Mpc.

Here the constructed binary black hole (BBH) and binary neutron star (BNS) system leaves the network with an averaged SNR of $\rho = 14.6$ and $\rho = 17.0$, respectively. For unequal mass systems we choose a BBH system with a 1:2 mass ratio and a black hole neutron star (BHNS) binary with the following:

- BBH 1:2- $(m_1, m_2) = (5, 10)M_\odot$, $D_L = 850$Mpc.
- BHNS- $(m_1, m_2) = (1.4, 10)M_\odot$, $D_L = 450$Mpc.

which respectively give SNRs of $\rho = 14.9$ and $\rho = 15.8$. For direction reconstruction and related extrinsic parameters the network geometry is important; however, for intrinsic parameters (as with the ppE parameters) SNR gains and losses have a larger impact [3].

In the seven-dimensional study, β is varied along $b = -3, -7$ for a BBH 1:1, 1:2, and BHNS systems. The reason for $b = -3$ is that it simulates modifications to the dispersion of a GW (e.g., massive gravitons or Lorentz violations [14, 17]). Also, $b = -7$ simulates weak-field modifications for dipole gravitational radiation (e.g., Brans-Dicke [5, 13]) and the non-spinning, even-parity sector of quadratic modified gravity (e.g., Einstein-Dilation-Gauss-Bonnett, or EDGB, gravity [25]). Distinguishability from GR is denoted as the condition that errors are smaller than the separation between parameters of the GR-limit and that of some alternative theory.

Two-dimenstional Study: Equal Mass

In this subsection uncertainties for a two-dimensional parameter space are computed for both the BBH 1:1 and BNS systems, marked by $\Delta\theta^i_{\text{ppE}}$. Parameter b is chosen at a fixed PN-order correction with PN-order 0.0, 0.5, 1.0, 1.5, 2.0, and 3.0 (i.e., $b = -5, -4, -3, -2, -1, +1$) while β is varied at each PN order. Here β probes values small enough to induce a sky-averaged error larger than 100% in b and large enough for $\lesssim$ 10% sky-averaged error in β. Errors for the BBH 1:1 system are depicted in figure 3.2, each labeled column representing a particular PN-order modification. Furthermore, to demonstrate the SNR dependence the BBH 1:1 system contains values for the scenario in which the SNR is doubled, for this the

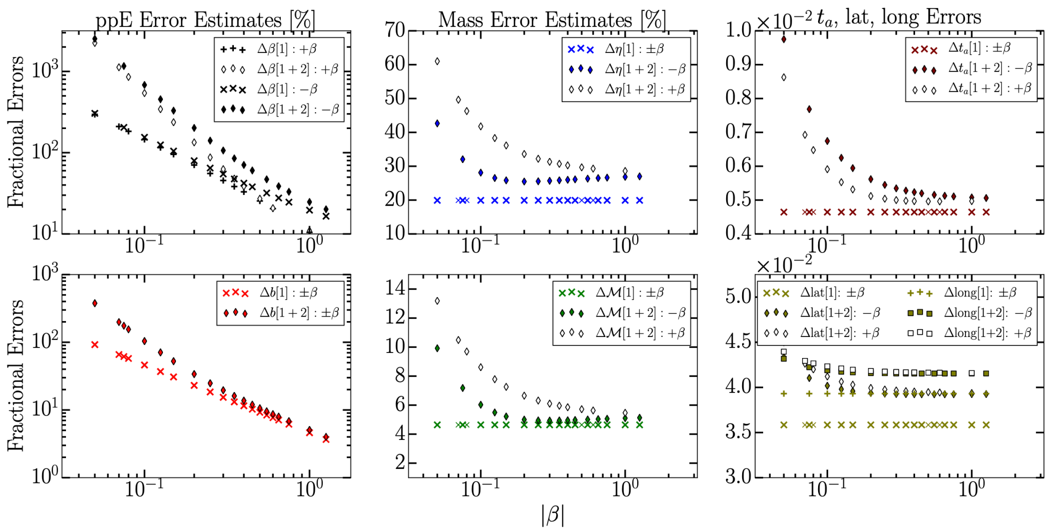

Figure 3.4: Sky-averaged uncertainties for the equal-mass BBH 1:1 system for a PN-order 1.0 modification of the seven dimensional parameter space (ppE parameters $\{\beta, b\}$ and physical parameters $\{\eta, \log\mathcal{M}, t_c, \text{lat}, \text{long}\}$). In the left column the top panel displays $\Delta\beta$ percent errors as a function of β (the sign of β provides different error estimates) and below that are Δb errors as a function of β (the sign of β does not play a role in these error estimates). In the middle and to the right are the physical parameters' errors, where the constraint of β primarily affects the second-order contributions. Enlarging the parameter space increases error estimates from those computed in figure 3.2 at PN-order 1.0, thus weakening constraints on β. For negative β, the full-dimensional study states $\Delta\beta[1] = 100\%$ at $\beta = -0.16$ and $\Delta\beta[1+2] = 100\%$ at $\beta = -0.32$.

distance is decreased to $D_L = 550$ Mpc. Figure 3.3 illustrates similar results for the BNS system.

The constant slopes of errors at first-order are catalogued in Table 3.1 for each PN-order. The computed first-order errors are consistent with statements of Ref. [11] which demonstrate that different PN-order corrections lead to different feasible constraints on β-values. BNS systems offer tighter constraints on β at each chosen b. It is interesting to observe that scaling parameters controlling propagating modifications, e.g. the graviton wavelength $\beta_{\rm MG} \propto \lambda_g^{-2}$, are not more tightly constrained with BNS systems at shorter distances than BBH systems at larger distances. Rather, parameters like $\beta_{\rm MG}$, also depend on a distance measure and masses of the compact objects that adversely affect constraints at shorter distances and smaller masses.

The smaller β, the more second-order effects in the errors contribute. Second-order effects on the errors of b are less significant, and only errors $> 100\%$ on β force

ppE β-value	Error Estimations	$\rho_{\max} = 20.8$	$\rho_{\min} = 7.0$
-0.25			
(a)	$\Delta b[2]/\Delta b[1]$	0.55	1.67
	$\Delta b[1]$	12.1 [%]	36.2 [%]
	$\Delta b[1+2]$	13.8 [%]	70.5 [%]
	$\Delta\beta[2]/\Delta\beta[1]$	1.19	3.57
	$\Delta\beta[1]$	42.7 [%]	126.4 [%]
(b)	$\Delta\beta[1+2]$	66.4 [%]	468.7 [%]
-0.35			
	$\Delta b[2]/\Delta b[1]$	0.43	1.28
	$\Delta b[1]$	8.7 [%]	25.8 [%]
	$\Delta b[1+2]$	9.4 [%]	42.0 [%]
	$\Delta\beta[2]/\Delta\beta[1]$	0.91	2.72
(c)	$\Delta\beta[1]$	31.4 [%]	92.9 [%]
(d)	$\Delta\beta[1+2]$	42.4 [%]	269.1 [%]
-0.55			
	$\Delta b[2]/\Delta b[1]$	0.32	0.99
	$\Delta b[1]$	5.5 [%]	16.4 [%]
	$\Delta b[1+2]$	5.8 [%]	23.2 [%]
(e)	$\Delta\beta[2]/\Delta\beta[1]$	0.65	1.96
	$\Delta\beta[1]$	21.1 [%]	62.4 [%]
(f)	$\Delta\beta[1+2]$	25.2 [%]	137.3 [%]

Table 3.2: Maxima and minima of estimates depicted in the sky-map plot (figure 3.5) for respective β-values of figure 3.4. Errors are the smallest for $\rho_{\max} = 20.8$ and largest for $\rho_{\min} = 7.0$. Terms labeled with (a), (b)..., (f) correspond to respective color bars in figure 3.5. Values are chosen because they offer the most insight.

sizeable second-order contributions in b. If b is near distinguishable, $\Delta b[1+2] \lesssim 100\%$, $\Delta\beta[1+2]$ are much larger than $\Delta\beta[1]$. Only when $\Delta b[1+2] \lesssim 10\%$ do $\Delta\beta[1]$ and $\Delta\beta[1+2]$ converge to similar estimates. Simulations producing the results of figures 3.2 and 3.3 used both $\pm\beta$ values and the skewed representation of figure 3.1 is not apparent. Note that the range of β values, in which error bounds are $\leq 100\%$ (figures 3.2 and 3.3), are orders of magnitude smaller than the β-value ranges considered in previous studies based on Bayesian methods [11].

Full Parameter Space: Equal Mass

The most realistic results come from the study of the largest resolvable parameter space. In this subsection, first- and second-order uncertainties $\Delta\vartheta^i$ of a full 7-dimensional parameter space are calculated for the equal-mass BBH 1:1 system, where $\vartheta = \{\theta_{\text{ppE}}, \theta_{\text{phys}}\}$. Here b is fixed to induce a PN-order 1.0 modification

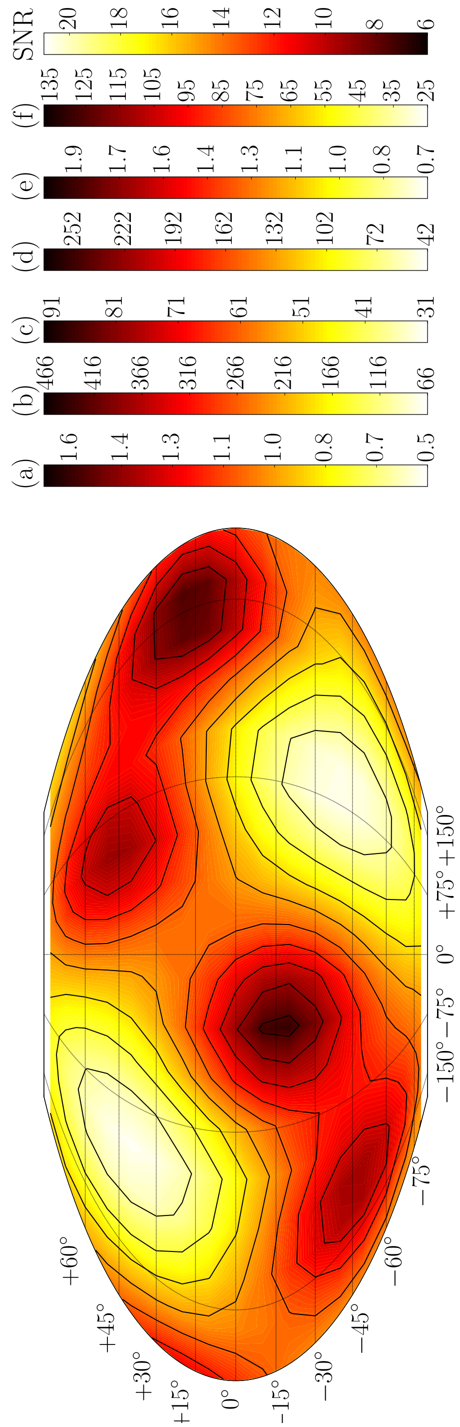

Figure 3.5: Sky distribution of error estimates. Color bars represent range of ppE quantities labeled (a), (b). . . , (f) in Table 3.2. This demonstrates the correlation of the SNR and ppE error estimation over the sky. See text for discussion.

($b = -3$). Such corrections simulate effects produced by modifying the GW dispersion relation [5, 17]. Unlike the two-dimensional cases, the errors (first- and second-order) are effected by the sign of β, where sky-averaged errors for the ppE parameter pair (β, b) are displayed in the left column of figure 3.4. Errors of physical parameters affected by varying β are depicted in the middle and right column of figure 3.4. The skewed behavior of $\pm\beta$ results are representative of fitting factor results of figure 3.1.

For β the first-order errors are not at a constant slope. $\Delta\beta[1]$ approximately follows linear relationship: $\Delta\beta[1] \approx 0.046|\beta| + 0.15$, for negative β. Here a 100% threshold error occurs at $\beta = -0.16$, for $\Delta\beta[1]$, and $\beta = -0.32$, for $\Delta\beta[1+2]$. In this more realistic scenario, it can be seen that for extremely small β values b falls within its own uncertainty. Yet, analogous to the two parameter space, a 100% error in $\Delta b[1+2]$ requires large errors in $\Delta\beta[1+2]$. Furthermore, error estimates are at least an order of magnitude larger. Another aspect of considering a full-dimensional parameter space are the additional error trends imparted on physical parameters (masses, arrival time, etc) when β is varied, see the middle and right column of figure 3.4.

The sky distributions of the errors and the SNR are shown in figure 3.5. Table 3.2 catalogs this for $-\beta = 0.25, 0.35, 0.55$. This SNR dependence is similar to intrinsic parameters for GWs. The β values, being a PN-order 1.0 correction characterizing massive graviton dispersion tests, are chosen for the following reasons:

1. At $\beta = -0.25$, figure 3.4 identifies the conditions: $\Delta b[2]/\Delta b[1] \approx 1$ with $\Delta\beta[1] < 100\% < \Delta\beta[1+2]$. Sky averages are performed before computing the ratios. In SNR $\gtrsim 15$, we have $\Delta b[2]/\Delta b[1] \lesssim 1$, as seen in (a). (b) diplays $\Delta\beta[1+2]$, which ranges from 66.4% to 468.7%. $\Delta\beta[2]$ dominates the error budget.

2. For $\beta = -0.35$, sky-averaged $\Delta\beta[1] < \Delta\beta[1+2] \approx 100\%$. Although $\Delta b[2]/\Delta b[1] > 1$, in limited portions of the sky, the ratio never exceeds 1.3 with a maximum of $\Delta b[1+2] = 42.0\%$. There is a strong increase in $\Delta\beta[1+2]$ from $\Delta\beta[1]$ in low SNRs. The majority of the sky is dominated by second-order terms, with $\Delta\beta[2]/\Delta\beta[1]$ ranging from 0.91 to 2.72.

3. $\beta = -0.55$ is where we calculate sky-averaged ratio $\Delta\beta[2]/\Delta\beta[1] \approx 1$ with $\Delta\beta[1] < \Delta\beta[1+2] < 100\%$. Here larger portion of the sky has ratio $\Delta\beta[2]/\Delta\beta[1] < 1$ as shown in (e). A majority (but not all) of the sky-map

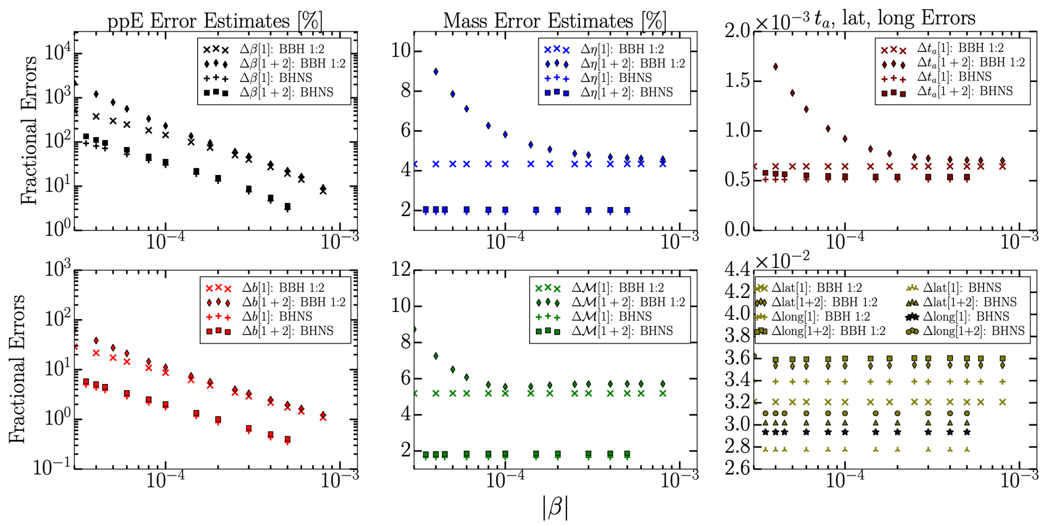

Figure 3.6: Sky-averaged error estimates for the BBH 1:2 and BHNS system. Left column represent calculations of the ppE parameter errors ($\Delta\beta, \Delta b$) for negative β-values, center column are the mass errors ($\Delta\eta, \Delta\mathcal{M}$), and far right are arrival time Δt_a and latitude-longitude (Δlat, Δlong) error estimates. Here latitude-longitude error estimates are not affected by β variation, as was previously presented in the equal-mass system. This study states that $\Delta\beta_{\text{BBH1:2}}[1+2] = 95.2\%$ at $\beta_{\text{BBH1:2}} = -1.8 \times 10^{-4}$ and $\Delta\beta_{\text{BHNS}}[1+2] = 95.3\%$ at $\beta_{\text{BHNS}} = -4.5 \times 10^{-5}$.

has total error falling below 100% after the inclusion of second-orders with sky-averaged error at $\Delta\beta[1+2] \approx 47\%$.

From the known dependence on ρ, quantities displayed in figure 3.5 and Table 3.2 can be easily re-derived for higher or lower SNRs.

Full Parameter Space: Unequal Mass

Here first- and second-order uncertainties $\Delta\vartheta^i$ of a full seven-dimensional parameter space are calculated for the BBH 1:2 and BHNS system. In this case a weak-field $b = -7$ modification is induced, which in our context mimics the non-spinning, even-parity sector of quadratic modified gravity (QMG) and can include specifics like EDGB gravity. Inclusion of QMG modifications is due to β being resolvable by a non-zero mass differences at this PN-order. These modifications manifest through modification of the energy flux as $\beta \propto \zeta_3(1-4\eta)$ [25] and the BHNS binary can also test examples of dipole gravitational radiation, like Brans-Dicke (BD).

Error bounds are presented in figure 3.6. The overall trend of this system's estimates are similar to the results of the equal-mass BBH 1:1 of the previous subsection, with a few exceptions. The first being that the separation between errors $\Delta\beta[1], \Delta b[1]$

and $\Delta\beta[1+2], \Delta b[1+2]$ are not as great as with the PN-order 1.0 modification. In comparison to the previous subsection, the chirp mass errors $\Delta\mathcal{M}$ are roughly the same, yet $\Delta\eta$ estimates are considerably less. Time of arrival errors Δt_a are also less and latitude-longitudinal estimates don't suffer from varying β at first- and second-order.

For the BBH 1:2 system sky contours of ppE and mass error estimates at, respectively, $|\beta| = 1.8 \times 10^{-4}$ and $|\beta| = 3.0 \times 10^{-4}$ are displayed in figures 3.7. In figure 3.7, the mass error estimates (bottom color bars) are plotted since this β-value produces sky-averaged estimate $\Delta\beta[1+2] < 100\%$, with second-order effects in the mass estimates making notable contributions (see figure 3.6). We observe that in such a context second-order effects do not dominate the error budget of $\Delta\eta$ and $\Delta\mathcal{M}$ in this sky-grid. In low-SNR regions, $\Delta\eta[2]/\Delta\eta[1]$ and $\Delta\mathcal{M}[2]/\Delta\mathcal{M}[1]$ are near unity. In these same low-SNR regimes $\Delta\beta[2]/\Delta\beta[1] > 1$ and $\Delta\beta[1+2] > 100\%$, which demonstrates the sky-grid SNR relation to errors accrued on physical parameters due to large error estimates of ppE parameters.

Figure 3.7 also represents a second set of contours generated for $|\beta| = 1.8 \times 10^{-4}$ modifications. Top color bars are representative of ppE parameter error estimates $(\Delta\beta, \Delta b)$ valid for this choice of β. Contours are plotted at this β-value since this simulates the condition that $\Delta\beta[1+2] \approx 100\%$ with $\Delta\beta[1] < 100\%$. Again we observe the volatility in $\Delta\beta[1+2]$ estimates, ranging from 53% to about 250% while remaining strongly correlated to the SNR. One notable feature of this plot is that ratios $\Delta b[2]/\Delta b[1]$ and $\Delta\beta[2]/\Delta\beta[1]$ are relatively close to each other, being approximately equal to each other in regions of high-SNR. This is in contrast to the equal-mass study of the previous subsection and demonstrates the small separation in $\Delta\beta[1]$ and $\Delta\beta[1+2]$ estimates depicted in the left column of figure 3.6, which allows the ratio $\Delta b[2]/\Delta b[1]$ to be comparable to $\Delta\beta[2]/\Delta\beta[1]$. Relations between these quantities depicted in figure 3.7 can be compared to the extrema of the equal-mass BBH system of PN-order 1.0 modifications catalogued in Table 3.2. Similar results come from the BHNS system.

In order to check that the Fisher information matrix did not become singular we systematically explored its eigenvalues. For example figure 3.8 shows scenarios in which the Fisher matrix becomes singular for the seven dimensional study. These values of β were avoided in this analysis.

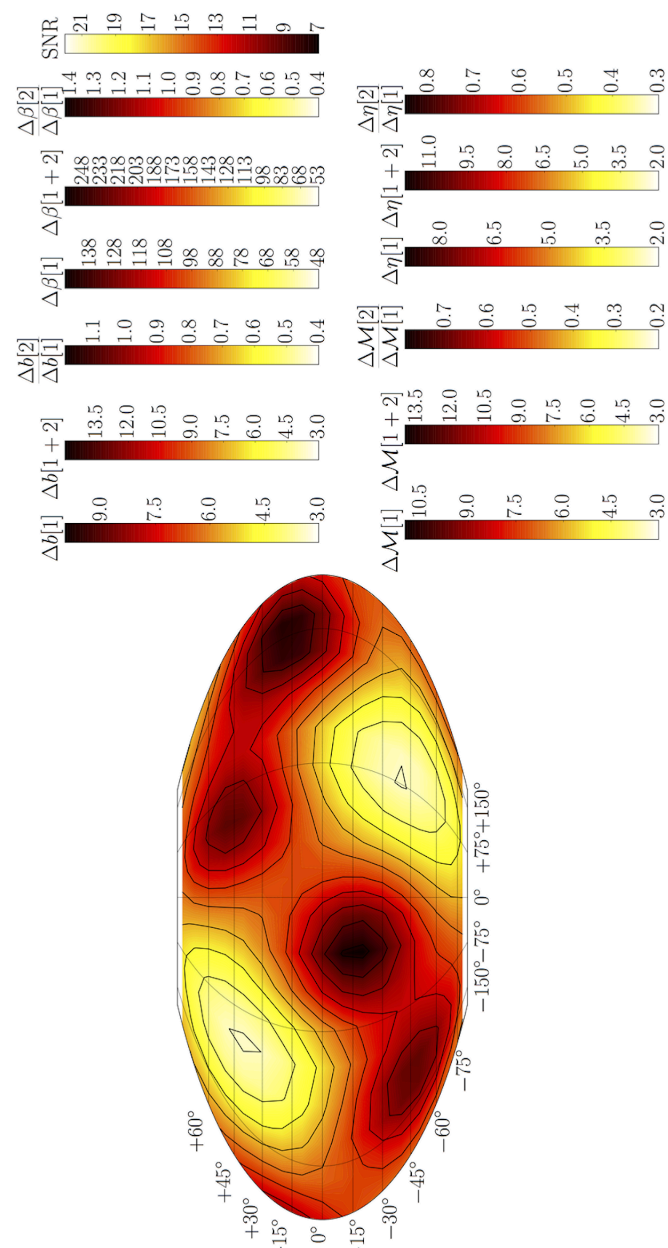

Figure 3.7: Sky-map error estimates of ppE parameters $\Delta\beta$ and Δb and mass parameters $\Delta\eta$ and $\Delta\mathcal{M}$ for the unequal mass BBH 1:2 system. The top color bars for ppE parameters are for $\beta_{\mathrm{BBH1:2}} = -1.8 \times 10^{-4}$ and the mass parameters below that are for $\beta_{\mathrm{BBH1:2}} = -3.0 \times 10^{-4}$ of results in figure 3.6. The SNR color bar is valid for both error estimates. Sky-average estimates provide $\Delta\beta_{\mathrm{BBH1:2}}[1+2] = 95.2\%$, of $\beta_{\mathrm{BBH1:2}} = -1.8 \times 10^{-4}$, and $\Delta\beta_{\mathrm{BBH1:2}}[1+2] = 47.4\%$ at $\beta_{\mathrm{BBH1:2}} = -3.0 \times 10^{-4}$.

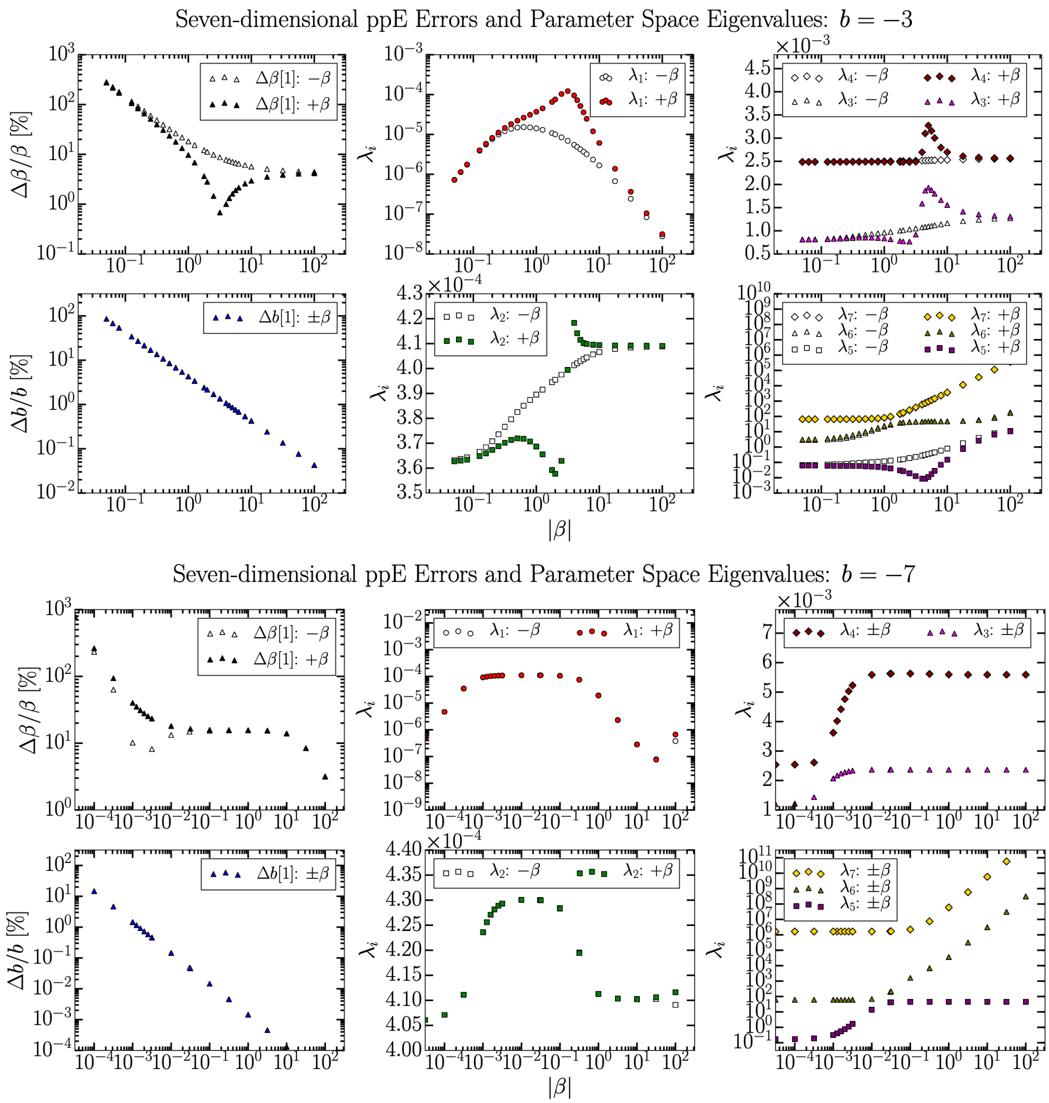

Figure 3.8: First order errors (left panels) and eigenvalues (center and right panels) of the Fisher matrix when computations are extended to the seven dimensional parameter space.

Distinguishability constraint ($\lesssim$ 100% Error)	
$\lambda_{g,\mathrm{LV}} > 3.04 \times 10^{12}$ km	(BBH 1:1)
$\xi_3^{1/4} < 7.17$ km	(BBH 1:2)
$\lvert\alpha_{\mathrm{EDGB}}\rvert^{1/2} < 2.69$ km	(BBH 1:2)
$\xi_3^{1/4} < 9.45$ km	(BHNS)
$\lvert\alpha_{\mathrm{EDGB}}\rvert^{1/2} < 3.55$ km	(BHNS)
$\omega_{\mathrm{BD}} > 12.7(s_{\mathrm{NS}} - 0.5)^2$	(BHNS)

Table 3.3: Seven-dimensional study of the BBH 1:1, 1:2, and BHNS systems with feasible constraints, i.e., computed MSE $\lesssim$ 100%. The first considers PN-order 1.0 modifications and the latter two consider $b = -7$ modifications. Included are the graviton wavelength (or generic Lorentz-violating) dispersion modification and non spinning, even-parity sector models of QMG (EDGB parameter included). Brans-Dicke constraint depends on sensitivity parameter $0.2 \leq s_{\mathrm{NS}} \leq 0.3$.

Application to Explicit Alternative Theories

Since the modification considered in subsection 3.5 occur at PN-order 1.0 in the phase, an analysis can be done from these results for the massive graviton model. Progression of sky-averaged errors for $\Delta\beta[1 + 2]$, calculated from negative β-values, of figure 3.4 imposes a constraint of $|\beta_{\mathrm{MG}}| \leq 0.31$. Existing constraints are $|\beta_{\mathrm{MG,static}}| \leq 0.37$ and $|\beta_{\mathrm{MG,GW}}| \leq 2.89 \times 10^{-2}$, based on current static and dynamical (from GW150914 event) bounds on λ_g (see section 3.3) computed from the BBH 1:1 system at 1100 Mpc. This asymptotic approach thus produces an additional 16.2% constraint on existing static bounds at 1σ. When including second-order terms in error estimation the constraints on λ_g have a fractional increase of 30% from the first-order Fisher matrix approach as calculated in this chapter. Given these results, further constraints on the graviton wavelength λ_g may be possible, even with second-order error terms accounted for in the low-SNR limit of the inspiral stage only. From calculated results the sky-averaged feasible bounds are displayed in Table 3.3.

Bayesian assessments in the ppE framework of unequal mass systems (of 1:2 and 1:3 ratios) with SNR of 20 put constraints at $\lambda_g > 8.8 \times 10^{12}$ km [11]. Other Bayesian studies also conclude that advanced detecters would generally not favor a MG theory over that of GR when λ_g is larger than the most stringent static bounds [12]. From the TIGER method implemented in the testing GR analysis of GW150914, constraints are at $\lambda_g > 10^{13}$ km, when the full inspiral-merger-ringdown signal is used (total SNR of $\rho \sim 24$) [43]. In this respect, our errors impart a more conservative approach to error estimation that still suggest that constraints may still be improved.

An application of seven-dimensional results presented in subsection 3.5 for the BBH 1:2 can also be made. This $b = -7$ modification has $\beta_{\mathrm{QMG}} \propto \zeta_3(1-4\eta)$. In this context the constraint parameter is $\zeta_3 = \xi_3 M^{-4}$ in the non-spinning, even-parity sector of QMG, where $\xi_3 = 16\pi\alpha_{\mathrm{EDGB}}^2$ in EDGB gravity [25]. For the BBH 1:2 system figure 3.6 presents $\Delta\beta[1] = 99.7\%$ at $|\beta| = 1.4{\times}10^{-4}$ and $\Delta\beta[1{+}2] = 95.2\%$ at $|\beta| = 1.8{\times}10^{-4}$. These computations translate to respective inputs in Table 3.3 for ξ_3 and α_{EDGB}. Strongest suggested constraints have, in terms of EDGB parameter, $|\alpha_{\mathrm{EDGB}}|^{1/2} < 1.9$ km and $|\alpha_{\mathrm{EDGB}}|^{1/2} < 9.8$ km [26, 38]. In weak-field tests the Cassini spacecraft has provided $|\alpha_{\mathrm{EDGB}}|^{1/2} < 8.9 \times 10^6$ km (i.e., $\xi_3^{1/4} < 2.4 \times 10^7$ km) [36]. Bayesian results estimate $\xi_3^{1/4} \lesssim 11$ km (or $|\alpha_{\mathrm{EDGB}}|^{1/2} \lesssim 4$ km) at an SNR of 20 [25] which is quoted in Ref. [5] as $\xi_3^{1/4} \lesssim 20$ km for an SNR of 10.

Similar application to QMG and EDGB theories can be done with results of the BHNS system. These constraints are also presented in Table 3.3 and are more stringent than the BBH 1:2 system. With BHNS systems Brans-Dicke can be investigated through $\beta_{\mathrm{BD}} \propto (s_1 - s_2)^2\omega_{\mathrm{BD}}^{-1}$, where constraint parameter is ω_{BD} with $s_{\mathrm{BH}} = 0.5$ for black holes and for neutron stars $0.2 \le s_{\mathrm{NS}} \le 0.3$ [27–30]. Figure 3.6 results indicate $\Delta\beta[1] = 95.3\%$ at $|\beta| = 4.5 \times 10^{-5}$ for the BHNS system. Thus, constraints results in $\omega_{\mathrm{BD}} \ge 1.14$ and $\omega_{\mathrm{BD}} \ge 0.51$ at $s_{\mathrm{NS}} = 0.2$ and $s_{\mathrm{NS}} = 0.3$, respecitvely. Results of the Cassini spacecraft have also established $\omega_{\mathrm{BD}} > 4 \times 10^4$ [37]. In Ref. [13] Fisher estimates placed constants of $\omega_{\mathrm{BD}} > 194$ for a BHNS systems of similar masses.

3.6 Conclusion

In this chapter we implement a frequentist asymptotic expansion method to estimate error bounds on the set of ppE parameters modifying the phase of the inspiral part of low-SNR ($\rho \sim 15-17$) GW transients. Figure 3.9 provides a summary of the main results of this chapter. The bound on the mean-squared error estimates from compact binaries studied is shown. Each mark represents the boundary of the (β, b)-parameter space where the minimum mean-squared error estimates are 100%, with β values below each b-value $>$ 100% and therefore not resolvable. Previous Bayesian studies correspond to the range of exponential ppE parameter: $-11 \le b \le 2$, as compared to the figure 3.9 summary. The fact that for the massive graviton case ($b = -3$) our approach here, which is a more realistic lower limit of the Cramér-Rao Lower Bound for early detections, rules out results that were allowed by a Bayesian study [11], seems to indicate the need of a careful evaluation of the role of the priors.

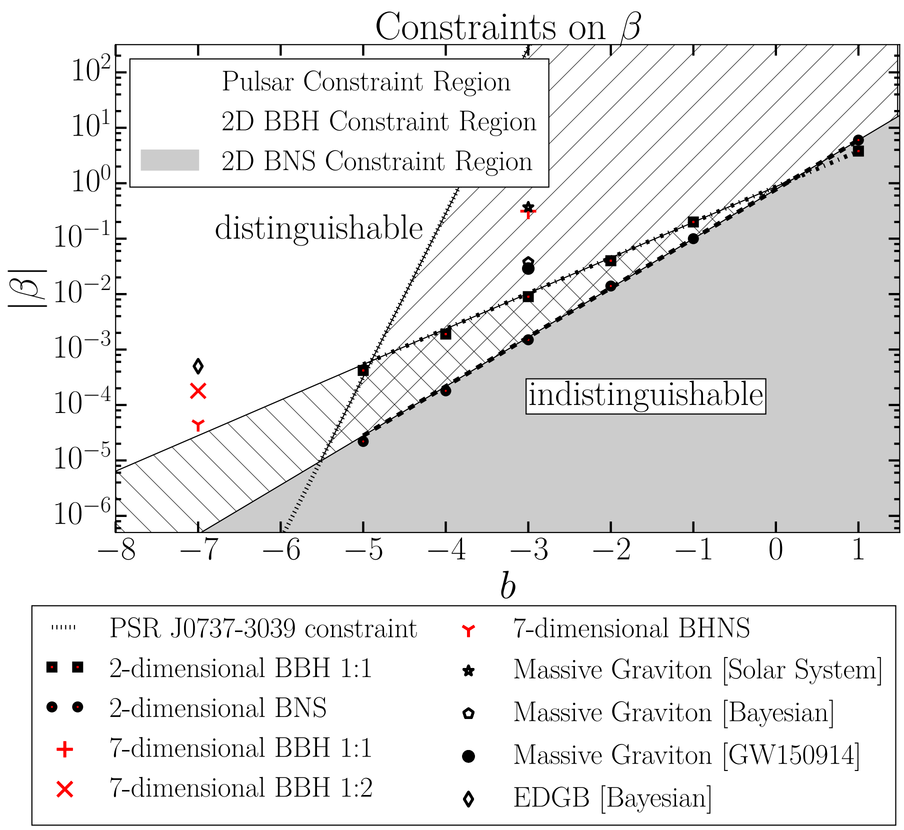

Figure 3.9: Constraints on ppE parameters (β, b). Alongside frequentist mean-squared error $\lesssim 100\%$ estimates are constraints imposed by Bayesian estimates [11], solar system tests [35], binary pulsar measurements [23, 24], and GW150914 event. Regions below each mark/line are where violations cannot be detected based on each respective study. The GR-limit is $\beta = 0$. Our frequentist two-dimensional study considers ppE parameter space (β, b), while seven-dimensional studies includes physical parameters (masses, etc.). See text for discussion.

Results of the higher order asymptotic analysis of the frequentist approach to error estimation states that further constraints can be imposed on existing non-GR theories with the study of the seven-dimensional parameter space (see Table 3.3). This approach does not involve the use of priors. Here the graviton wavelength can be constrained by an additional 16.2% as compared to current static bounds [35]. Yet, these projected constraints do not further bound the graviton wavelength when compared to Bayesian estimates or values imposed by GW150914. Note that although GW150914 provides a constraint of $\lambda_g > 10^{13}$ km, our result holds for a lower SNR of the inspiral stage only. Further studies present the scenario for the weak-field $b = -7$ modification, which can include quadratic modified gravity (QMG) (specifics being EDGB gravity) and Brans-Dicke type modifications (figure 3.6). For the non-spinning, even-party sector of QMG, bounds suggest further constraints are possible as compared to current bounds placed by Bayesian estimates and Cassini constraints. Furthermore, error estimates for modifications at both PN-order 1.0 and the $b = -7$ weak-field follow similar sky-map contours, which are correlated to the SNR patterns (see figures 3.5 and 3.7).

General results show that for successively higher PN-order modifications, set by b, the separation between first- and second-order errors increase (see figures 3.2 and 3.3). Such an effect percolates to the seven-dimensional study. Error bounds also increase as the parameter space is enlarged, where the two-dimensional studies provide overly optimistic error bounds. As constraints on β become tighter in the seven-dimensional studies, the effects of second-order estimates also accrue on physical parameters, namely η, $\mathcal{M}$, t_a, and latitude-longitude parameters (see figures 3.4 and 3.6). Finally, SNR increases translate error estimates as discussed in Ref. [3] (figure 3.2), so all results can be rescaled as a function of the SNR.

Calculations performed in this chapter are for single detection scenarios. With multiple detections the presence of weak, but consistent, violations could be combined to a make a stronger statement about error estimations. Such methods to *resolve* consistent signals were explored in a Bayesian framework in Ref. [9] and it is left for future studies in the frequentist framework. Furthermore, as waveform models advance, for both the inspiral and ppE framework, the application of our maximum likelihood estimator asymptotic expansion could be applied to spinning binaries or to waveforms that include the merger and ringdown phases. This will add insight into additional modified theories mappable into the ppE framework.

References

[1] M. Zanolin, S. Vitale, and N. Makris, PRD **81**, 124048, `10.1103/PhysRevD.81.124048` (2010).

[2] S. Vitale and M. Zanolin, PRD **82**, 124065, `10.1103/PhysRevD.82.124065` (2010).

[3] S. Vitale and M. Zanolin, PRD **84**, 104020, `10.1103/PhysRevD.84.104020` (2011).

[4] N. Yunes and F. Pretorius, PRD **80**, 122003, `10.1103/PhysRevD.80.122003` (2009).

[5] N. Yunes and X. Siemens, LRR **16**, 9, `10.12942/lrr-2013-9` (2013).

[6] K. G. Arun, B. R. Iyer, M. S. S. Qusailah, and B. S. Sathyaprakash, Classical and Quantum Gravity **23**, L37–L43 (2006).

[7] K. G. Arun, B. R. Iyer, M. S. S. Qusailah, and B. S. Sathyaprakash, PRD **74**, 024006, `10.1103/PhysRevD.74.024006` (2006).

[8] C. K. Mishra, K. G. Arun, B. R. Iyer, and B. S. Sathyaprakash, PRD **82**, 064010, `10.1103/PhysRevD.82.064010` (2010).

[9] T. G. F. Li, W. Del Pozzo, S. Vitale, C. Van Den Broeck, M. Agathos, J. Veitch, K. Grover, T. Sidery, R. Sturani, and A. Vecchio, PRD **85**, 082003, `10.1103/PhysRevD.85.082003` (2012).

[10] T. G. F. Li, W. Del Pozzo, S. Vitale, C. Van Den Broeck, M. Agathos, J. Veitch, K. Grover, T. Sidery, R. Sturani, and A. Vecchio, in Journal of physics conference series, Vol. 363, Journal of Physics Conference Series (June 2012).

[11] N. Cornish, L. Sampson, N. Yunes, and F. Pretorius, PRD **84**, 062003, `10.1103/PhysRevD.84.062003` (2011).

[12] W. Del Pozzo, J. Veitch, and A. Vecchio, PRD **83**, 082002, `10.1103/PhysRevD.83.082002` (2011).

[13] C. M. Will, PRD **50**, 6058–6067 (1994).

[14] C. M. Will, PRD **57**, 2061–2068 (1998).

[15] K. G. Arun and C. M. Will, Classical and Quantum Gravity **26**, 155002, `10.1088/0264-9381/26/15/155002` (2009).

[16] D. Keppel and P. Ajith, PRD **82**, 122001, `10.1103/PhysRevD.82.122001` (2010).

[17] S. Mirshekari, N. Yunes, and C. M. Will, PRD **85**, 024041, `10.1103/PhysRevD.85.024041` (2012).

[18] T. A. Apostolatos, PRD **52**, 605–620 (1995).

[19] K. Chatziioannou, N. Yunes, and N. Cornish, PRD **86**, 022004, `10.1103/PhysRevD.86.022004` (2012).

[20] M. Isi, A. J. Weinstein, C. Mead, and M. Pitkin, PRD **91**, 082002, `10.1103/PhysRevD.91.082002` (2015).

[21] M. Vallisneri and N. Yunes, PRD **87**, 102002, `10.1103/PhysRevD.87.102002` (2013).

[22] M. Vallisneri, PRD **77**, 042001, `10.1103/PhysRevD.77.042001` (2008).

[23] N. Yunes and S. A. Hughes, PRD **82**, 082002, `10.1103/PhysRevD.82.082002` (2010).

[24] A. G. Lyne, M. Burgay, M. Kramer, A. Possenti, R. N. Manchester, F. Camilo, M. A. McLaughlin, D. R. Lorimer, N. D'Amico, B. C. Joshi, J. Reynolds, and P. C. C. Freire, Science **303**, 1153–1157 (2004).

[25] K. Yagi, L. C. Stein, N. Yunes, and T. Tanaka, PRD **85**, 064022, `10.1103/PhysRevD.85.064022` (2012).

[26] K. Yagi, PRD **86**, 081504, `10.1103/PhysRevD.86.081504` (2012).

[27] J. Healy, T. Bode, R. Haas, E. Pazos, P. Laguna, D. M. Shoemaker, and N. Yunes, Classical and Quantum Gravity **29**, 232002, `10.1088/0264-9381/29/23/232002` (2012).

[28] S. Mirshekari and C. M. Will, PRD **87**, 084070, `10.1103/PhysRevD.87.084070` (2013).

[29] N. Yunes, P. Pani, and V. Cardoso, PRD **85**, 102003, `10.1103/PhysRevD.85.102003` (2012).

[30] H. W. Zaglauer, ApJ **393**, 685 (1992).

[31] K. Yagi, N. Yunes, and T. Tanaka, PRL **109**, 251105, `10.1103/PhysRevLett.109.251105` (2012).

[32] D. Colladay and V. A. Kostelecký, PRD **58**, 116002, `10.1103/PhysRevD.58.116002` (1998).

[33] V. A. Kostelecký, PRD **69**, 105009, `10.1103/PhysRevD.69.105009` (2004).

[34] V. A. Kostelecký and J. D. Tasson, Physics Letters B **749**, 551–559 (2015).

[35] E. Berti, J. Gair, and A. Sesana, PRD **84**, 101501, `10.1103/PhysRevD.84.101501` (2011).

[36] L. Amendola, C. Charmousis, and S. C. Davis, JCAP **2007**, 004, `10.1088/1475-7516/2007/10/004` (2007).

[37] B. Bertotti, L. Iess, and P. Tortora, Nature **425**, 374–376 (2003).

[38] P. Pani, E. Berti, V. Cardoso, and J. Read, PRD **84**, 104035, `10.1103/PhysRevD.84.104035` (2011).

[39] N. Yunes, K. Yagi, and F. Pretorius, PRD **94**, 084002, `10.1103/PhysRevD.94.084002` (2016).

[40] V. A. Kostelecký and M. Mewes, Physics Letters B **757**, 510–514 (2016).

[41] B. Allen, arXiv e-prints, gr-qc/9607075, gr–qc/9607075 (1996).

[42] B. F. Schutz, Classical and Quantum Gravity **28**, 125023, `10.1088/0264-9381/28/12/125023` (2011).

[43] B. P. Abbott *et al.* (LIGO and Virgo Scientific Collaboration), PRL **116**, 221101, `10.1103/PhysRevLett.116.221101` (2016).

Chapter 4

ACTIVE INTERFEROMETRY WITH MULTIBAND GW ASTRONOMY

The early inspiral of massive stellar-mass black-hole binaries merging in LIGO's sensitivity band will be detectable at low frequencies by the upcoming space mission LISA. LISA will predict, with years of forewarning, the time and frequency with which binaries will be observed by LIGO. We will, therefore, find ourselves in the position of knowing that a binary is about to merge, with the unprecedented opportunity to optimize ground-based operations to increase their scientific payoff. We apply this idea to detections of multiple ringdown modes, or black-hole spectroscopy. Narrowband tunings can boost the detectors' sensitivity at frequencies corresponding to the first subdominant ringdown mode and largely improve our prospects to experimentally test the Kerr nature of astrophysical black holes. We define a new consistency parameter between the different modes, called δGR, and show that, in terms of this measure, optimized configurations have the potential to double the effectiveness of black-hole spectroscopy when compared to standard broadband setups.

The first detections of merging black-hole (BH) binaries by the LIGO ground-based detectors are one of the greatest achievement in modern science. Some of the binary component masses are as large as $\sim 30M_{\odot}$, and unexpectedly exceed those of all previously known stellar-mass BHs [1–4]. These systems might also be visible by the future spaced-based detector LISA, which will soon observe the gravitational-wave (GW) sky in the mHz regime [5]. LISA will measure the early inspiral stages of BH binaries predicting, with years to weeks of forewarning, the time at which the binary will enter the LIGO band [6]. This will allow electromagnetic observers to concentrate on the source's sky location, thus increasing the likelihood of observing counterparts. Multi-band GW observations have the potential to shed light on BH-formation channels [7–13], constrain dipole emission [14], enhance searches and parameter estimation [15, 16], and provide new measurements of the cosmological parameters [17, 18].

Here we explore the possibility of improving the science return of ground-based GW observations by combining LISA forewarnings to active interferometric techniques.

LISA observations of stellar-mass BH binaries at low frequencies can be exploited to prepare detectors on the ground in their most favorable configurations for a targeted measurement. Optimizations can range from the most obvious ones (for instance just ensuring the detectors are operational), to others that require more experimental work, like changing the input optical power, modifying mirror transmissivities and cavity tuning phases, and changing the squeeze factor and angle of the injected squeeze vacuum (see, e.g., [19]). Tuning the optical setup of the interferometer can allow to boost the signal-to-noise ratio (SNR) of specific features of the signal "on-demand" (only at the needed time, only at the needed frequency).

In particular, we apply this line of reasoning to the so-called *black-hole spectroscopy*: testing the nature of BHs through their ringdown modes. Narrowband tunings were previously explored for studying the detectability of neutron-star mergers [20–22] and stochastic backgrounds [23], and are here proposed for BH science for the first time.

The perturbed BH resulting from a merger vibrates at very specific frequencies. These quasi-normal modes of oscillation are damped by GW emission, resulting in the so-called BH ringdown [24, 25]. If BHs are described by the Kerr solution of General Relativity (GR) [26], all these resonant modes are allowed to depend on two quantities only: mass and spin of the perturbed BH [27–29]. This is a consequence of the famous *no-hair theorems*: as two BHs merge, all additional complexities (hair) of the spacetime are dissipated away in GWs, and a Kerr BH is left behind. The detection of frequency and decay time of one quasi-normal mode can therefore be used to infer mass and spin of the post-merger BH. Measurements of each additional mode provide consistency tests of the theory. This is the main idea behind BH spectroscopy: much like atoms' spectral lines can be used to identify nuclear elements and test quantum mechanics, quasi-normal modes can be used to probe the nature of BHs and test GR [30–33]. Despite its elegance, BH spectroscopy turns out to be challenging in practice as it requires loud GW sources and improved data analysis techniques [34–39].

The main idea behind our study is illustrated Fig. 4.1. A GW source like GW150914 emits GWs at ~ 0.1 Hz and is visible by LISA with SNR~ 5. After ~ 10 years, the emission frequency reaches ~ 10 Hz and the source appears in the sensitivity band of LIGO or a future ground-based detector. The excitation amplitude of the dominant quasi-normal mode is ~ 10 times higher than the first subdominant mode. The latter is likely going to be too weak to perform BH spectroscopy. Optimized narrowband

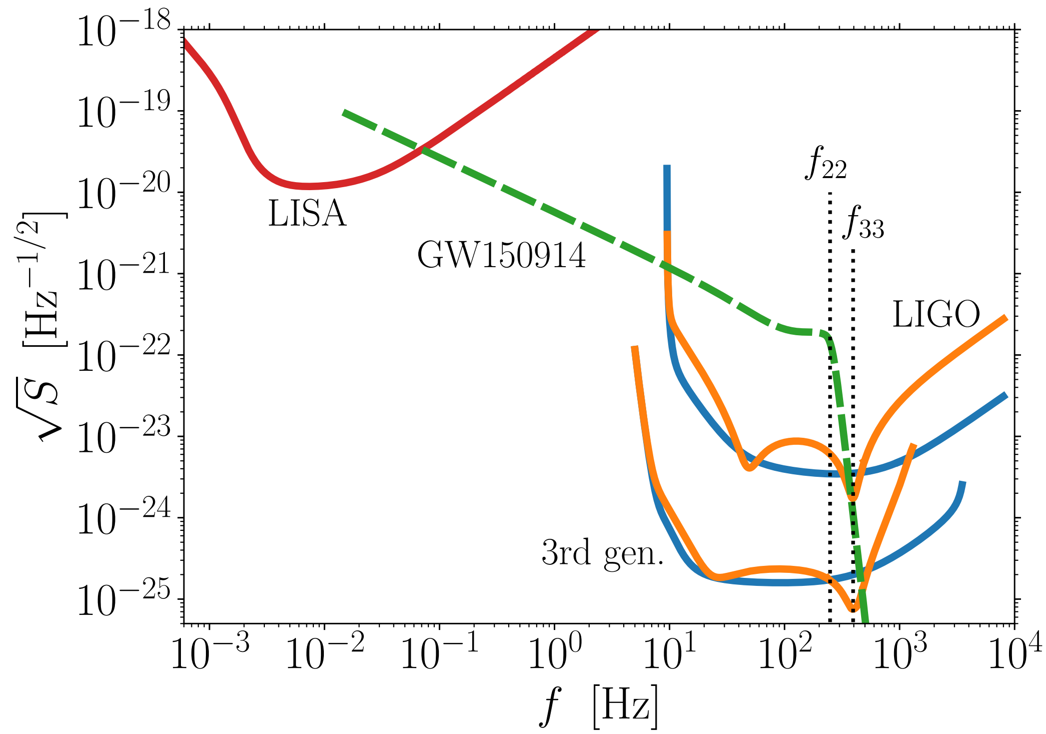

Figure 4.1: GW amplitude $\sqrt{S_h} = 2|\tilde{h}|\sqrt{f}$ of a black-hole binary source similar to GW150914 compared to the noise curves $\sqrt{S_n}$ of LISA [40], LIGO [41], and a planned 3rd-generation detector [42] (both in their broadband configurations and with narrowband tunings). Optimized narrowbanding enhances (decreases) the detector sensitivity around the frequency f_{33} (f_{22}) of the first subdominant (dominant) mode of the BH ringdown. The BH binary waveform is generated using the approximant of [43] with $m_1 + m_2 = 65M_\odot$, $q = 0.8$, $D = 410$ Mpc, $\iota = 150°$ assuming optimal orientation ($\theta = \phi = \psi = 0$).

tunings can boost the detectability of the weaker mode at the expense of the rest of the signal, making BH spectroscopy possible.

This chapter is organized as follows. In Sec. 4.1 and 4.2 we introduce BH spectroscopy and narrowband tunings, respectively. Our results are illustrated in Sec. 4.3. We draw our conclusions in Sec. 4.4. Hereafter, we use geometric units $c = G = 1$.

4.1 Black-hole Spectroscopy

Black-hole Ringdown

Let us consider a perturbed BH with detector-frame mass M and dimensionless spin j. GW emission during ringdown can be described by a superposition of damped sinusoids, labeled by $l \geq 2$, $0 \leq |m| \leq l$ and $n \geq 0$ [44]. For simplicity, we only consider the fundamental overtone $n = 0$.

Each mode is described by its frequency $\omega_{lm} = 2\pi f_{lm}$ and decay time τ_{lm}. The GW strain can be written as [45, 46],

$$
\begin{aligned}
h(t) &= \sum_{l,m>0} B_{lm} e^{-t/\tau_{lm}} \cos\left(\omega_{lm} t + \gamma_{lm}\right) , && (4.1)\\
B_{lm} &= \frac{\alpha_{lm} M}{D} \sqrt{\left(F_+ Y_+^{lm}\right)^2 + \left(F_\times Y_\times^{lm}\right)^2} , && (4.2)\\
\gamma_{lm} &= \phi_{lm} + m\beta + \arctan\left(\frac{F_\times Y_\times^{lm}}{F_+ Y_+^{lm}}\right) , && (4.3)\\
Y_{+,\times}^{lm}(\iota) &= {}_{-2}Y_{lm}(\iota, \beta{=}0) \pm (-1)^l {}_{-2}Y_{l-m}(\iota, \beta{=}0) , && (4.4)
\end{aligned}
$$

where α_{lm} and ϕ_{lm} are the mode amplitudes and phases, D is the luminosity distance to the source, ${}_{-2}Y_{lm}(\iota, \beta)$ are the spin-weighted spherical harmonics, $F_{+,\times}(\theta, \phi, \psi)$ are the single-detector antenna patterns [47]. Note that here M is the mass of the post-merger BH, where the total mass of the binary will be expressed explicitly in component masses $m_1 + m_2$ in this chapter. The angles ι and β describe the orientation of the BH, with ι (β) being the polar (azimuthal) angle of the wave propagation direction measured with respect to the BH spin axis. In the conventions of [48, 49], the frequency-domain strain reads,

$$
\tilde{h}(f) = \sum_{l,m>0} B_{lm} \frac{-\omega_{lm} \sin\gamma_{lm} + (1/\tau_{lm} - i\omega)\cos\gamma_{lm}}{\omega_{lm}^2 - \omega^2 + 1/\tau_{lm}^2 - 2i\omega/\tau_{lm}} , \qquad (4.5)
$$

where $f = \omega/2\pi$ is the GW frequency.

The dominant mode corresponds to l=2, m=2 (hereafter "22"), while the first subdominant is usually l=3, m=3 (hereafter "33"). Other modes might sometimes be stronger than the 33 mode for specific sources. For instance, the 33-mode is suppressed for $q \simeq 1$ or $\sin\iota \simeq 0$ (e.g [36, 50, 51]). Here we perform a simple two-mode analysis considering the 22 and 33 modes only. Strictly speaking, the ringdown modes have angular distributions described by spheriodal, instead of spherical harmonics. However, for the final black-hole spins we consider, the 22 and 33 spin-weighted spherical harmonics have more than 99% overlap with the corresponding spin-weighted spheroidal harmonics [52, 53], which is accurate enough for this study.[1] For simplicity, we restrict ourselves to non-spinning binary BHs with source-frame masses m_1 and m_2; we address the impact of this assumption in

[1] We do note that, for the final black-hole spins we are considering, ${}_{-2}S_{22}$ and ${}_{-2}Y_{32}$ have overlap between 0.05 and 0.1, which does cause the 22 ringdown mode to show up significantly in the spherical-harmonic mode h_{32}. This is nevertheless consistent with the 99% overlap between ${}_{-2}Y_{22}$ and ${}_{-2}S_{22}$, because $\sum_{l'} |\langle {}_{-2}Y_{l'm}|{}_{-2}S_{lm}\rangle|^2 = 1$.

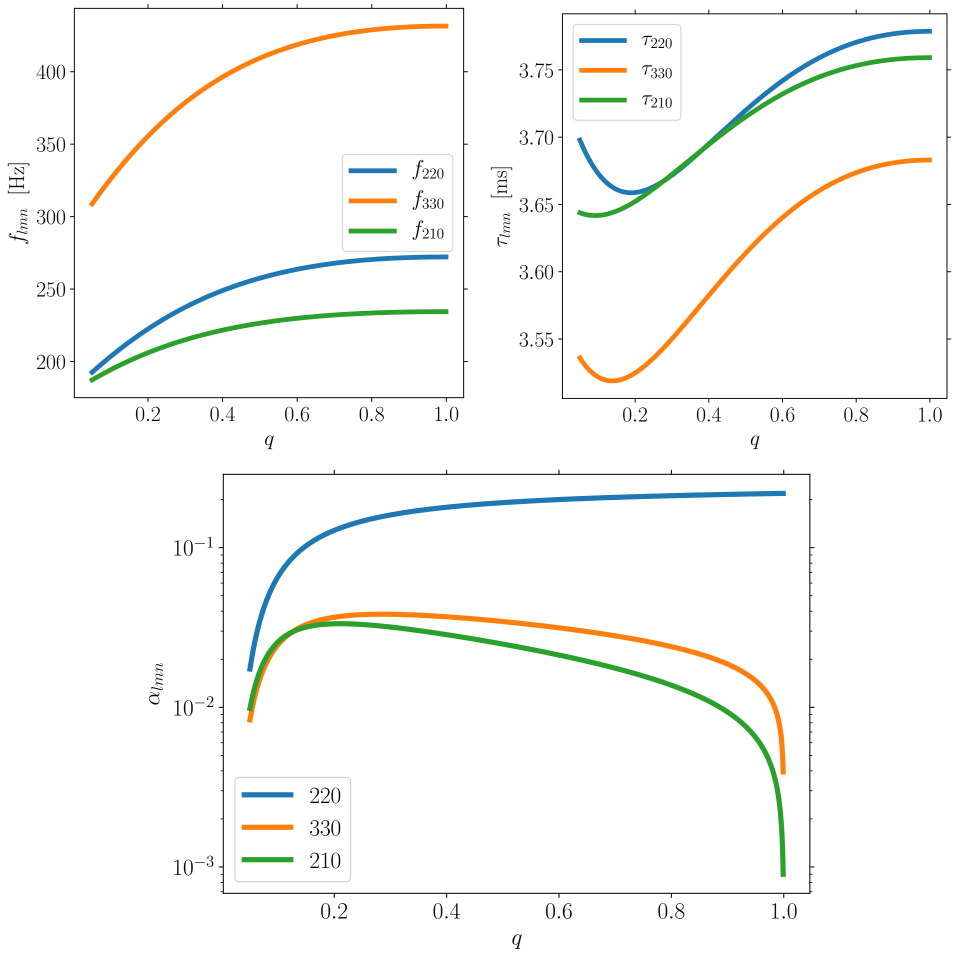

Figure 4.2: Parameters determining the ringdown's features as function of the binary's component mass ratio q, where $m_1+m_2 = 65M_\odot$ is fixed. Considering $n = 0$ overtone the next subdominant modes' frequency, damping time, and amplitude excitation are plotted along with the $l = m = 2$ mode.

Sec. 4.4. Redshifted masses $m_i(1 + z)$ are computed from the luminosity distance D using the Planck cosmology [54]. Mass M and spin j of the post-merger BH are estimated using fits to numerical relativity simulations [55, 56] as implemented in [57]. Quasi-normal frequencies ω_{lm} and decay times τ_{lm} are estimated from [32], where,

$$\begin{aligned} f_{lmn} &= \frac{f_1 + f_2(1-j)^{f_3}}{2\pi M}, \\ \tau_{lmn} &= \frac{q_1 + q_2(1-j)^{q_3}}{\pi f_{lmn}}. \end{aligned} \tag{4.6}$$

Here f_i and q_i are fit parameters. We estimate the excitation amplitudes α_{lm} given the mass ratio $q = m_2/m_1 \leq 1$ of the merging binary using the expressions reported by [46]. Figure 4.2 displays the range of frequencies, damping times, and amplitude excitation as a function of the binary's mass ratio for dominant and next subdominant modes (of fundamental $n = 0$ overtone). These assume the initial binary is composed of non-spinning component masses. BH ringdown parameter estimation has been shown to depend very weakly on the phase offsets ϕ_{lm} [32], which we thus we set to 0 for simplicity (c.f. also [58]).

Waveform Model and GR Test

In BH spectroscopy, one assumes that quasi-normal modes frequencies ω_{lm} and decay times τ_{lm} for different modes depend separately on M and j, and then look for consistencies between the different estimates.[2] Considering the 22 and 33 modes only, one can write the waveform as,

$$h = h_{22}(M_{22}, j_{22}) + h_{33}(M_{33}, j_{33}) \tag{4.7}$$

and use data to estimate the parameters,

$$\boldsymbol{\lambda} \equiv \{M_{22}, j_{22}, M_{33}, j_{33}\}\,. \tag{4.8}$$

Deviations from GR may cause non-zero values of,

$$\epsilon_M \equiv \frac{M_{22} - M_{33}}{(M_{22} + M_{33})/2}\,, \quad \epsilon_j \equiv \frac{j_{22} - j_{33}}{(j_{22} + j_{33})/2}\,. \tag{4.9}$$

We, therefore, seek to maximize our ability to estimate ϵ_M and ϵ_j from the observed data.

Given true values $\bar{\lambda}_i$, each independent noise realization will result in estimates $\tilde{\lambda}_i$ given by,

$$\tilde{\lambda}_i = \bar{\lambda}_i + \delta\lambda_i\,, \tag{4.10}$$

where $\delta\lambda_i$ are random variables driven by noise fluctuations in a way that depends on both the signal and the estimation scheme. Measured values of deviation from GR can be obtained by inserting measured values $\tilde{M}_{22,33}$ and $\tilde{j}_{22,33}$ into Eq. (4.9), resulting in,

$$\tilde{\epsilon}_M = \frac{\tilde{M}_{22} - \tilde{M}_{33}}{(\tilde{M}_{22} + \tilde{M}_{33})/2}\,, \quad \tilde{\epsilon}_j = \frac{\tilde{j}_{22} - \tilde{j}_{33}}{(\tilde{j}_{22} + \tilde{j}_{33})/2}\,. \tag{4.11}$$

At linear order one gets $\tilde{\epsilon}_M = \bar{\epsilon}_M + \delta\epsilon_M$ and $\tilde{\epsilon}_j = \bar{\epsilon}_j + \delta\epsilon_j$, with,

$$\delta\epsilon_M = \frac{\bar{M}_{33}\delta M_{22} - \bar{M}_{22}\delta M_{33}}{(\bar{M}_{22} + \bar{M}_{33})^2/4}\,, \quad \delta\epsilon_j = \frac{\bar{j}_{33}\delta j_{22} - \bar{j}_{22}\delta j_{33}}{(\bar{j}_{22} + \bar{j}_{33})^2/4}\,. \tag{4.12}$$

[2] For simplicity we only vary ω_{lm} and τ_{lm} while keeping α_{lm} fixed to their GR values.

In the absence of any deviations from GR, one has $\bar{M}_{22} = \bar{M}_{33} = \bar{M}$ and $\bar{j}_{22} = \bar{j}_{33} = \bar{j}$, but ϵ_M and ϵ_j will have statistical fluctuations given by,

$$\delta\epsilon_M = \frac{\delta M_{22} - \delta M_{33}}{\bar{M}}\,, \quad \delta\epsilon_j = \frac{\delta j_{22} - \delta j_{33}}{\bar{j}}\,. \tag{4.13}$$

The levels of these fluctuations will quantify our ability to test GR. In fact, Eqs. (4.13) are good approximations to (4.12), as long as fractional deviation from GR is small, i.e., when $\bar{\epsilon}_M \ll 1$, and $\bar{\epsilon}_j \ll 1$.

Estimation Errors

The covariance matrix σ_{ij}, namely the expectation values,

$$\sigma_{ij} \equiv \langle \delta\lambda_i \delta\lambda_j \rangle \tag{4.14}$$

can be bounded by the Fisher information formalism [59] (but see [60]). The conservative bound for the error is given by the inverse of the Fisher Information matrix:

$$\sigma_{ij} = \mathbf{\Gamma}^{-1}_{ij}\,, \quad \mathbf{\Gamma}_{ij} = \left(\frac{\partial \tilde{h}}{\partial \lambda_i}\middle|\frac{\partial \tilde{h}}{\partial \lambda_j}\right), \tag{4.15}$$

where parenthesis indicate the standard noise-weighted inner product.

In our case, the covariance matrix can be broken into blocks,

$$\mathbf{\Gamma}^{-1} = \begin{bmatrix} (\mathbf{\Gamma}^{-1})_{2222} & (\mathbf{\Gamma}^{-1})_{2233} \\ (\mathbf{\Gamma}^{-1})_{3322} & (\mathbf{\Gamma}^{-1})_{3333} \end{bmatrix} \tag{4.16}$$

corresponding to the couples (M_{22}, j_{22}) and (M_{33}, j_{33}). Diagonal block $(\mathbf{\Gamma}^{-1})_{2222}$ correspond to errors when estimating (M_{22}, j_{22}) alone (marginalizing over other uncertainties), the diagonal block $(\mathbf{\Gamma}^{-1})_{3333}$ correspond to errors when estimating (M_{33}, j_{33}) alone (marginalizing over other uncertainties), while the non-diagonal blocks contains error correlations.

From the covariance matrix for $(M_{22}, j_{22}, M_{33}, j_{33})$, one obtains the following expectation values,

$$\langle \delta\epsilon_M^2 \rangle = \frac{\sigma_{M_{22}M_{22}} - 2\sigma_{M_{22}M_{33}} + \sigma_{M_{33}M_{33}}}{\bar{M}^2}\,, \tag{4.17}$$

$$\langle \delta\epsilon_j^2 \rangle = \frac{\sigma_{j_{22}j_{22}} - 2\sigma_{j_{22}j_{33}} + \sigma_{j_{33}j_{33}}}{\bar{j}^2}\,, \tag{4.18}$$

$$\langle \delta\epsilon_M \delta\epsilon_j \rangle = \frac{\sigma_{M_{22}j_{22}} - \sigma_{M_{33}j_{22}} - \sigma_{j_{22}M_{33}} + \sigma_{M_{33}j_{33}}}{\bar{M}\bar{j}}\,. \tag{4.19}$$

which are elements of the covariance matrix of $(\delta\epsilon_M, \delta\epsilon_j)$. For concreteness, we define a scalar figure of merit,

$$\delta\text{GR} = \begin{vmatrix} \langle \delta\epsilon_M^2 \rangle & \langle \delta\epsilon_M \delta\epsilon_j \rangle \\ \langle \delta\epsilon_M \delta\epsilon_j \rangle & \langle \delta\epsilon_j^2 \rangle \end{vmatrix}^{1/4} \tag{4.20}$$

to quantify our ability to test GR. More specifically, δGR measures our statistical error in revealing deviations from GR. One has the strongest possible test of GR when $\delta\text{GR} \to 0$, corresponding to $\mathbf{\Gamma}^{-1} \to \mathbf{0}$, in which case any deviation from GR will be revealed with vanishing statistical error. Large values of δGR would require larger deviations from GR [i.e., larger true values of (ϵ_M, ϵ_j)] in order to be detectable.

Given values of δGR from both a design and an optimized detector configuration, it is useful to define the narrowband gain,

$$\zeta = \frac{\delta\text{GR}^{(\text{Design})} - \delta\text{GR}^{(\text{Optimized})}}{\delta\text{GR}^{(\text{Design})}}, \tag{4.21}$$

where $\zeta = 1$ ($\zeta = 0$) means that the narrowbanding procedure is maximally effective (irrelevant).

Error Correlations Between Modes

We note that 22-33 correlation components of the Fisher information matrix, as well as its inverse, are expected to be small because the two modes are well separated in the frequency domain. In particular, $\partial h(\omega)/\partial M_{22}$ and $\partial h(\omega)/\partial j_{22}$ peak near ω_{22} with widths $\sim 1/\tau_{22}$, while $\partial h(\omega)/\partial M_{33}$ and $\partial h(\omega)/\partial j_{33}$ peak near ω_{33} with widths $\sim 1/\tau_{33}$. For this reason, the pairs $(\delta M_{22}, \delta j_{22})$ and $(\delta M_{33}, \delta j_{33})$ are nearly statistically independent from each other. Estimation error for ϵ_M and ϵ_j can be viewed as (almost) independently contributed from the 22 and 33 modes and summed by quadrature. One has, approximately,

$$\langle \delta\epsilon_M^2 \rangle \approx \frac{\sigma_{M_{22}M_{22}} + \sigma_{M_{33}M_{33}}}{\bar{M}^2}, \tag{4.22}$$

$$\langle \delta\epsilon_j^2 \rangle \approx \frac{\sigma_{j_{22}j_{22}} + \sigma_{j_{33}j_{33}}}{\bar{j}^2}, \tag{4.23}$$

$$\langle \delta\epsilon_M \delta\epsilon_j \rangle \approx \frac{\sigma_{M_{22}j_{22}} + \sigma_{M_{33}j_{33}}}{\bar{M}\bar{j}}. \tag{4.24}$$

In other words, the covariance matrix of $(\delta\epsilon_M, \delta\epsilon_j)$ is approximated by the sum of those of $(\delta M_{22}/\bar{M}, \delta j_{22}/\bar{j})$ and $(\delta M_{33}/\bar{M}, \delta j_{33}/\bar{j})$.

We quantify this claim by calculating values δGR where the off-diagonal sub-matrices $(\boldsymbol{\Gamma}^{-1})_{3322}$ and $(\boldsymbol{\Gamma}^{-1})_{2233}$ are artificially set to zero. For the population of sources studied in Sec. 4.3, and observed by LIGO, the median difference between the two estimates is as small as 1.6% (4.0%) for broadband (narrowband) configurations.

For this reason, some insight can be gained by visualizing the error region in the (M_{22}, j_{22}) and (M_{33}, j_{33}) planes separately (c.f Sec. 4.3): errors in $(\delta\epsilon_M, \delta\epsilon_j)$ are well approximated by the quadrature sum of errors indicated by those regions. We stress however, that correlations are fully included in all values of δGR reported in the rest of this chapter.

4.2 Narrowband Tunings

As an example of a possible narrowband setup, we consider the detuning of the signal-recycling cavity (c.f. [21, 23] where a similar setup was also explored). Second-generation GW detectors make use of signal recycling optical configurations (or resonant side-band extraction) [61–63]. A signal recycling mirror is placed at the dark port of a Fabry-Perot Michelson interferometer, which is the configuration used in first-generation detectors. The transmittance $T_{\rm SRM}$ of this mirror determines the fraction of signal light which is sent back into the arms, possibly with a detuning phase $\phi_{\rm SRM}$,

$$\phi_{\rm SRM} = k l_{\rm SRC} + \frac{\pi}{4}. \tag{4.25}$$

Here $l_{\rm SRC}$ is the total length of the signal recycling cavity and $k = \pi/\lambda$ with a laser of wavelength k. Both these parameters affect the optical resonance properties of the interferometer [61, 62], as well as its optomechanical dynamics [64, 65]. Together with the homodyne readout phase $\phi_{\rm hd}$, $T_{\rm SRM}$ and $\phi_{\rm SRM}$ are responsible for the quantum noise spectrum of the interferometer, allowing for noise suppression near optical and optomechanical resonances [66].

In this chapter, we consider narrowbanding of both LIGO in its design configuration and future 3rd-generation detectors. The LIGO design noise-curve is a finalized experimental setup which allows us to perform a focussed assessment of the impact of narrowbanding onto BH spectroscopy over a large number of sources. However, more sensitive ground-based interferometers are currently being planned and are expected to be operational by the 2030s [42, 67]. Multi-band observations and LISA forewarnings might happen with a network of ground-based detectors perhaps 10 times more sensitive than LIGO.

In order to select the best detuned configuration to perform BH spectroscopy, one needs to choose values of $(T_{\rm SRM}, \phi_{\rm SRM}, \phi_{\rm hd})$ that boost sensitivity around the 33 frequency. For LIGO, we generate 60^3 noise curves with equal spacing in $\phi_{\rm SRM} \in [-0.12\pi, 0.12\pi]$, $T_{\rm SRM} \in [0.001, 0.2]$, and $\phi_{\rm hd} \in [0, \pi]$. This parameter space is capable of capturing the central frequencies of both the 22 and 33 mode for binaries with $q \in [0.2{-}0.9]$ and total masses $m_1 + m_2 \in [20M_\odot{-}100M_\odot]$. Noise curves are generated using pyGWINC [68]. The LIGO design configuration corresponds to $T_{\rm SRM} = 0.2$, $\phi_{\rm SRM} = 0$, and $\phi_{\rm hd} = \pi/2$. The broadband noise curves reported by [41, 69] are reproduced within $\Delta \log S_n / \log S_n \lesssim 0.2\%$ throughout the entire frequency band. For each given source, we select the optimal noise curve that minimizes δGR among those we precomputed. Figure 4.1 illustrates this procedure for an optimally oriented source similar to GW150914 [70]. This narrowband setting corresponds to a noise curve with $\phi_{\rm SRM} \simeq 0.21$, $T_{\rm SRM} \simeq 0.02$ and $\phi_{\rm hd} \simeq 2.24$.

While the design of 3rd-generation detectors still being discussed, it is anticipated that squeezed-vacuum injection will be used. Squeezer and cavity properties need to be optimized together to determine the optimal configuration. Fully tackling this interplay is outside the scope of this chapter. We have nonetheless attempted one of such studies, where *both* the filter cavity for the squeezed vacuum [71, 72] and signal-recycling cavity of the Cosmic Explorer [42] design have been optimized to target the ringdown emission of GW150914 (c.f. Fig. 4.1).

4.3 Results

Boosting Subdominant Modes

Confidence ellipses [73] constructed from $(\mathbf{\Gamma}^{-1})_{2222}$ and $(\mathbf{\Gamma}^{-1})_{3333}$ are shown in Fig. 4.2 for sources similar to GW150914. In the left panel, we consider narrow-banding of a LIGO detector for a source similar to GW150914 at the optimistic distance of $D = 40$ Mpc. This value is consistent with the closest GW source detected so far [74] and correspond to $\sim 1/10$ of the actual distance of GW150914. In the right panel, we consider detuning of a 3rd-generation detector (Cosmic Explorer) for the case of the same source at $D = 400$ Mpc.

The behavior of the ellipses of Fig. 4.2 illustrates the main point of our analysis. In the standard broadband configuration, the 22 mode is observed very well, thus resulting in a small confidence region. At the same time, the 33 mode is observed poorly resulting in a large ellipse. As in the case of current events [75], this is roughly equivalent to a single measurement of M and j based on the 22 mode only, rather

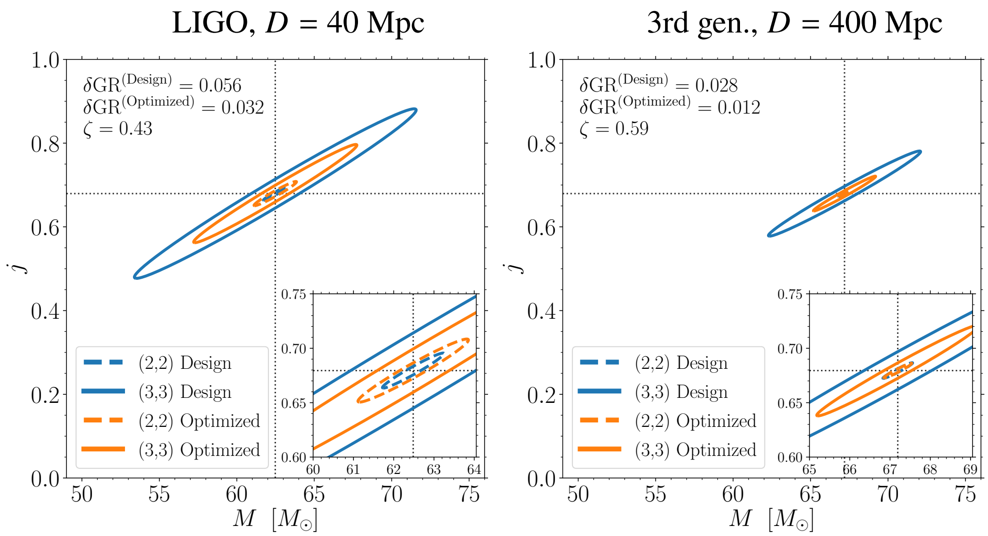

Figure 4.3: 1-σ confidence ellipses for the 22 (dashed) and 33 (solid) modes observed by GW detectors in their designed (blue) and optimized narrowband configuration (orange). In both panels, the source is a perturbed Kerr BH of mass $M = 62.5M_\odot$ and spin $j = 0.68$ (dotted lines), resulting from the merger of a GW150914-like system ($m_1 + m_2 = 65M_\odot$, $q = 0.8$, $\iota = 150°$, $\beta = 0$) assuming optimal orientation ($\theta = \phi = \psi = 0$). The left panel assumes an optimistic luminosity distance $D = 40$ Mpc and the LIGO detector in its design sensitivity. The right panel is generated assuming a 3rd-generation detector optimized for the same system and a realistic luminosity distance $D = 400$ Mpc.

than a test of the theory. Narrowband tunings boost the detectability of the 33 mode, while marginally reducing that of the dominant 22 excitation. Consequently, the two confidence ellipses are more similar to each other, resulting in a more powerful constraint of the Kerr metric.

For a source like GW150914 at 40 Mpc, narrowband tunings in LIGO boost prospects to perform BH spectroscopy from $\delta\mathrm{GR} = 0.056$ to $\delta\mathrm{GR} = 0.032$, thus offering the opportunity to improve constraints on the BH no-hair theorems by $\zeta = 43\%$. The same source at $D = 400$ Mpc observed by a 3rd generation detector will present a higher gain of $\zeta = 59\%$. Rescaling D between the left and right panel of Fig. 4.2 allows us to asses the potential of optimization in future interferometers. In particular, ellipses in the right panel are smaller than those in the left panel because, while the distance was changed from 40 to 400 Mpc, the expected improvement in sensitivity of Cosmic Explorer is more than a factor of 10 compared to LIGO. We obtain a larger gain ζ for 3rd-generation detectors because quantum noise is expected to dominate more over classical sources of noise compared to current interferometers [42]. There is, therefore, more room to take advantage of modifications in optical configurations.

Population Study

We now assess the impact of this procedure as a function of the source properties. We generate a population of sources drawing $\cos\theta$ and $\cos\iota$ uniformly in $[-1, 1]$ and β, ϕ, and ψ uniformly in $[-\pi, \pi]$ with fixed[3] distance $D = 100$ Mpc. Fig. 4.4 shows the median values of δGR as a function of the masses of the merging BHs. The top panel assumes LIGO in its design configuration, the middle panel presents results optimizing the narrowband setup individually for each source, while the gain ζ is shown in the bottom panel.

A few interesting trends are present. First, the best systems to perform BH spectroscopy (i.e. low values of δGR) have intermediate mass ratio $0.3 \lesssim q \lesssim 0.7$. Both ringdown amplitudes α_{22} and α_{33} are suppressed for $q \to 0$, while $\alpha_{22} \gg \alpha_{33}$ for $q \to 1$. Second, tests of GR are weaker (higher δGR) for lower mass systems. These binaries have f_{33} close to the edge of the sensitivity window of the interferometer, thus making mode distinguishability harder. The LISA SNR also increases with the total mass and the mass ratio. In particular, binaries with $m_1 + m_2 \lesssim 40 M_\odot$ are not likely to be associated with confirmed forewarnings (c.f. [13]).

A key point of our findings is illustrated in the gain values ζ reported in the bottom panel of Fig. 4.4. From Eq. (4.21), ζ quantifies the potential improvement in BH spectroscopy achievable with narrowband tunings. Median gains are larger than 25% over the entire parameter space, and individual sources can reach values up to 50%. In particular, higher gains are achieved for large-q systems. This agrees with the expectation that both modes are suppressed at $q \to 0$, while only the 33 mode is suppressed at $q \to 1$. Narrowband tunings shift the detector sensitivity closer to f_{33} at the expense of the 22 mode, and are thus more effective if its excitation is large such that the resulting sensitivity loss can be more easily absorbed.

4.4 Discussion

The possibility of optimizing ground-based operation assumes that LISA observations of the early inspiral accurately predict the ringdown frequencies (in particular f_{33}), thus providing information on *how* ground-based interferometers should be op-

[3] Since δGR is directly proportional to D, results in Fig. 4.4 can be rescaled to different distances. Cosmological effects might push the ringdown frequencies of some high-mass events out of band, thus somewhat decreasing the gain.

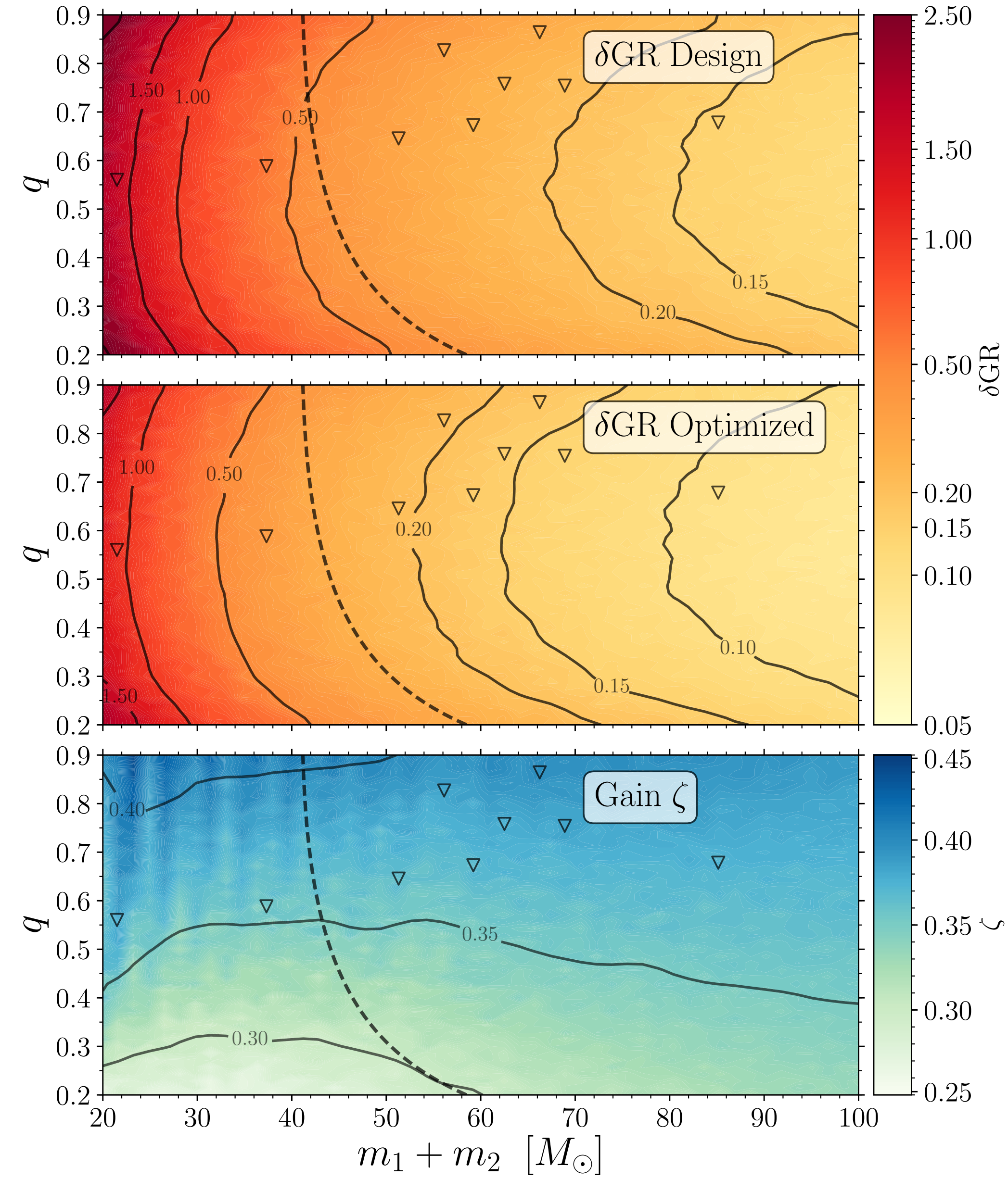

Figure 4.4: Contours for δGR results in the population study. Top and middle panels show median values of δGR for LIGO at design sensitivity and with narrowband tuning, respectively; bottom panel shows the median gain ζ. Data are shown as a function of total mass $m_1 + m_2$ and mass ratio q of the merging binaries; medians are computed over $\theta, \iota, \beta, \phi$, and ψ. The distance is fixed to $D = 100$ Mpc. Binaries to the right of the dashed lines have sky-averaged LISA SNRs greater than 8 (these are computed following [6] using the updated noise curve of [40] and the nominal mission duration $T_{\rm obs} = 4$ yr; the initial frequency is estimated such that the binary merges in $T_{\rm obs}$). Triangles indicate measured LIGO events from GWTC-1 (we show the medians of the posterior distributions from [1]).

timized. We estimate LISA errors on f_{33} as follows. For a given source with chirp mass $\mathcal{M}$ and symmetric mass ratio η, we first estimate f_{33} assuming zero spins (this is our working assumption used above). Inspired by the results reported in Fig. 3 of [6] (computed as in [76]), we model LISA errors as lognormal distributions centered at $\Delta\mathcal{M}/\mathcal{M} = 10^{-6}$, $\Delta\eta/\eta = 6 \times 10^{-3}$ with widths $\sigma = 0.5$. We then calculate f_{33} for a new binary with masses $\mathcal{M} + \Delta\mathcal{M}$ and $\eta + \Delta\eta$ and spins with magnitudes uniform in $[0, 1]$ and isotropic directions. In practice, we are assuming that LISA will not provide any information on the spins. This is a conservative, but realistic, assumption because spins enter at high post-Newtonian order and are going to be very challenging to detect at low frequencies [77]. This procedure is iterated over a population of sources with masses uniformly distributed in $[10, 100]M_\odot$. The median of the errors Δf_{33} is 11 Hz, while the 90th percentile is 46 Hz. For the case of cavity detuning explored here, typical bandwidths are $\gtrsim$ 200 Hz (c.f. Fig. 4.1), sensibly larger than the predicted errors. Therefore, we estimate that the risk of *missing* the source because the detector was detuned in the wrong configuration is very limited. The precision with which LISA will estimate the time of coalescence is at most of $\mathcal{O}(100\,\mathrm{s})$ [6], and should not pose significant challenges in the planning strategy. Moreover, only some of the ground-based instruments of the network could be optimized, while the rest are maintained in their broadband configuration.

Cavity detuning presents significant experimental challenges, regarding both detector characterization and lock acquisition, and might ultimately turn out to be impractical (see [78] for an exploration of these issues on the LIGO 40-m prototype). We note that narrowbanding can also be achieved without detuning by using e.g. twin-recycling [79] or speed-meter [80] configurations; such a possibility is currently being studied to optimize for post-merger signals from neutron-star mergers for future detectors [22]. Beyond targeted narrowbanding around the 33 frequency, optimization can also be achieved by re-configuring future ground-based interferometers in different ways. For the planned 3rd-generation detector Cosmic Explorer [42], the quantum noise is expected to dominate all other noise sources by more than a factor of 2 for frequencies $\gtrsim$ 40 Hz with a chosen bandwidth of 800 Hz. With forewarnings, a less broadband configuration (even without detuning) could be chosen to significantly improve BH spectroscopy. In the case of Einstein Telescope [67], a broad bandwidth is achieved by a xylophone that contains two different interferometers optimized for different frequency ranges. It is conceivable that a strong LISA forewarning might prompt a reconfiguration of the two interferometers to optimize for BH spectroscopy.

Space-based GW observatories like LISA will surely provide exquisite tests of GR with supermassive BH observations [32]. As shown here, they can further be exploited to improve BH spectroscopy in the different regime of lower-mass, higher-curvature BHs observed by LIGO and future ground-based facilities. More generally, forewarnings from space-based detectors will provide the opportunity to configure ground-based instruments to their most favorable configuration to perform targeted measurements and improve their science return.

References

[1] B. P. Abbott *et al.* (LIGO and Virgo Scientific Collaboration), Physical Review X **9**, 031040, `10.1103/PhysRevX.9.031040` (2019).

[2] B. P. Abbott *et al.* (LIGO and Virgo Scientific Collaboration), Physical Review X **11**, 021053, `10.1103/PhysRevX.11.021053` (2021).

[3] B. P. Abbott *et al.* (LIGO and Virgo Scientific Collaboration), arXiv e-prints, arXiv:2108.01045 (2021).

[4] B. P. Abbott *et al.* (LIGO and Virgo Scientific Collaboration), arXiv e-prints, arXiv:2111.03606 (2021).

[5] P. Amaro-Seoane, H. Audley, S. Babak, J. Baker, E. Barausse, P. Bender, E. Berti, P. Binetruy, M. Born, D. Bortoluzzi, J. Camp, C. Caprini, V. Cardoso, M. Colpi, J. Conklin, N. Cornish, C. Cutler, K. Danzmann, R. Dolesi, L. Ferraioli, V. Ferroni, E. Fitzsimons, J. Gair, L. Gesa Bote, D. Giardini, F. Gibert, C. Grimani, H. Halloin, G. Heinzel, T. Hertog, M. Hewitson, K. Holley-Bockelmann, D. Hollington, M. Hueller, H. Inchauspe, P. Jetzer, N. Karnesis, C. Killow, A. Klein, B. Klipstein, N. Korsakova, S. L. Larson, J. Livas, I. Lloro, N. Man, D. Mance, J. Martino, I. Mateos, K. McKenzie, S. T. McWilliams, C. Miller, G. Mueller, G. Nardini, G. Nelemans, M. Nofrarias, A. Petiteau, P. Pivato, E. Plagnol, E. Porter, J. Reiche, D. Robertson, N. Robertson, E. Rossi, G. Russano, B. Schutz, A. Sesana, D. Shoemaker, J. Slutsky, C. F. Sopuerta, T. Sumner, N. Tamanini, I. Thorpe, M. Troebs, M. Vallisneri, A. Vecchio, D. Vetrugno, S. Vitale, M. Volonteri, G. Wanner, H. Ward, P. Wass, W. Weber, J. Ziemer, and P. Zweifel, arXiv e-prints, arXiv:1702.00786 (2017).

[6] A. Sesana, PRL **116**, 231102, `10.1103/PhysRevLett.116.231102` (2016).

[7] A. Nishizawa, E. Berti, A. Klein, and A. Sesana, PRD **94**, 064020, `10.1103/PhysRevD.94.064020` (2016).

[8] K. Breivik, C. L. Rodriguez, S. L. Larson, V. Kalogera, and F. A. Rasio, ApJL **830**, L18, `10.3847/2041-8205/830/1/L18` (2016).

[9] A. Nishizawa, A. Sesana, E. Berti, and A. Klein, MNRAS **465**, 4375–4380 (2017).

[10] X. Chen and P. Amaro-Seoane, ApJL **842**, L2, 10.3847/2041-8213/aa74ce (2017).

[11] K. Inayoshi, N. Tamanini, C. Caprini, and Z. Haiman, PRD **96**, 063014, 10.1103/PhysRevD.96.063014 (2017).

[12] J. Samsing, D. J. D'Orazio, A. Askar, and M. Giersz, (2018).

[13] D. Gerosa, S. Ma, K. W. K. Wong, E. Berti, R. O'Shaughnessy, Y. Chen, and K. Belczynski, (2019).

[14] E. Barausse, N. Yunes, and K. Chamberlain, PRL **116**, 241104, 10.1103/PhysRevLett.116.241104 (2016).

[15] S. Vitale, PRL **117**, 051102, 10.1103/PhysRevLett.117.051102 (2016).

[16] K. W. K. Wong, E. D. Kovetz, C. Cutler, and E. Berti, PRL **121**, 251102, 10.1103/PhysRevLett.121.251102 (2018).

[17] K. Kyutoku and N. Seto, PRD **95**, 083525, 10.1103/PhysRevD.95.083525 (2017).

[18] W. Del Pozzo, A. Sesana, and A. Klein, MNRAS **475**, 3485–3492 (2018).

[19] R. X. Adhikari, Reviews of Modern Physics **86**, 121–151 (2014).

[20] S. A. Hughes, PRD **66**, 102001, 10.1103/PhysRevD.66.102001 (2002).

[21] H. Miao, H. Yang, and D. Martynov, PRD **98**, 044044, 10.1103/PhysRevD.98.044044 (2018).

[22] D. Martynov, H. Miao, H. Yang, F. Hernandez Vivanco, E. Thrane, R. Smith, P. Lasky, W. E. East, R. Adhikari, A. Bauswein, A. Brooks, Y. Chen, T. Corbitt, T. Corbitt, H. Grote, Y. Levin, C. Zhao, and A. Vecchio, (2019).

[23] D. Tao and N. Christensen, CQG **35**, 125002, 10.1088/1361-6382/aac148 (2018).

[24] C. V. Vishveshwara, Nature **227**, 936–938 (1970).

[25] E. Berti, V. Cardoso, and A. O. Starinets, CQG **26**, 163001, 10.1088/0264-9381/26/16/163001 (2009).

[26] R. P. Kerr, PRL **11**, 237–238 (1963).

[27] W. Israel, Comm. Math. Phys. **8**, 245–260 (1968).

[28] B. Carter, PRL **26**, 331–333 (1971).

[29] M. Heusler, *Black hole uniqueness theorems* (1996).

[30] S. Detweiler, ApJ **239**, 292–295 (1980).

[31] O. Dreyer, B. Kelly, B. Krishnan, L. S. Finn, D. Garrison, and R. Lopez-Aleman, CQG **21**, 787–803 (2004).

[32] E. Berti, V. Cardoso, and C. M. Will, PRD **73**, 064030, 10.1103/PhysRevD.73.064030 (2006).

[33] E. Berti, K. Yagi, H. Yang, and N. Yunes, GRG **50**, 49, 10.1007/s10714-018-2372-6 (2018).

[34] E. Berti, A. Sesana, E. Barausse, V. Cardoso, and K. Belczynski, PRL **117**, 101102, 10.1103/PhysRevLett.117.101102 (2016).

[35] A. Maselli, K. D. Kokkotas, and P. Laguna, PRD **95**, 104026, 10.1103/PhysRevD.95.104026 (2017).

[36] V. Baibhav, E. Berti, V. Cardoso, and G. Khanna, PRD **97**, 044048, 10.1103/PhysRevD.97.044048 (2018).

[37] H. Yang, K. Yagi, J. Blackman, L. Lehner, V. Paschalidis, F. Pretorius, and N. Yunes, PRL **118**, 161101, 10.1103/PhysRevLett.118.161101 (2017).

[38] S. Bhagwat, M. Okounkova, S. W. Ballmer, D. A. Brown, M. Giesler, M. A. Scheel, and S. A. Teukolsky, PRD **97**, 104065, 10.1103/PhysRevD.97.104065 (2018).

[39] R. Brito, A. Buonanno, and V. Raymond, PRD **98**, 084038 (2018).

[40] T. Robson, N. Cornish, and C. Liu, (2018).

[41] B. P. Abbott *et al.* (LIGO and Virgo Scientific Collaboration), LRR **19**, 1, 10.1007/lrr-2016-1 (2016).

[42] B. P. Abbott *et al.* (LIGO Scientific Collaboration and Virgo Collaboration), CQG **34**, 044001, 10.1088/1361-6382/aa51f4 (2017).

[43] S. Khan, S. Husa, M. Hannam, F. Ohme, M. Pürrer, X. J. Forteza, and A. Bohé, PRD **93**, 044007, 10.1103/PhysRevD.93.044007 (2016).

[44] S. A. Teukolsky, ApJ **185**, 635–648 (1973).

[45] E. Berti, J. Cardoso, V. Cardoso, and M. Cavaglià, PRD **76**, 104044, 10.1103/PhysRevD.76.104044 (2007).

[46] I. Kamaretsos, M. Hannam, S. Husa, and B. S. Sathyaprakash, PRD **85**, 024018, 10.1103/PhysRevD.85.024018 (2012).

[47] K. S. Thorne, in Three hundred years of gravitation, 330-458 (1987).

[48] F. Echeverria, PRD **40**, 3194–3203 (1989).

[49] L. S. Finn, PRD **46**, 5236–5249 (1992).

[50] L. London, D. Shoemaker, and J. Healy, PRD **90**, 124032, [Erratum: PRD 94 6 069902 (2016)], 10.1103/PhysRevD.90.124032 (2014).

[51] S. Bhagwat, D. A. Brown, and S. W. Ballmer, PRD **94**, 084024, 10.1103/PhysRevD.94.084024 (2016).

[52] E. Berti and A. Klein, PRD **90**, 064012, `10.1103/PhysRevD.90.064012` (2014).

[53] M. Giesler, M. Isi, M. A. Scheel, and S. A. Teukolsky, Physical Review X **9**, 041060, `10.1103/PhysRevX.9.041060` (2019).

[54] P. A. R. Ade *et al.* (Planck Collaboration), A&A **594**, A13, `10.1051/0004-6361/201525830` (2016).

[55] E. Barausse, V. Morozova, and L. Rezzolla, ApJ **758**, 63, `10.1088/0004-637X/758/1/63` (2012).

[56] E. Barausse and L. Rezzolla, ApJL **704**, L40–L44 (2009).

[57] D. Gerosa and M. Kesden, PRD **93**, 124066, `10.1103/PhysRevD.93.124066` (2016).

[58] J. G. Baker, W. D. Boggs, J. Centrella, B. J. Kelly, S. T. McWilliams, and J. R. van Meter, PRD **78**, 044046, `10.1103/PhysRevD.78.044046` (2008).

[59] C. Cutler and É. E. Flanagan, PRD **49**, 2658–2697 (1994).

[60] C. L. Rodriguez, B. Farr, W. M. Farr, and I. Mandel, PRD **88**, 084013, `10.1103/PhysRevD.88.084013` (2013).

[61] B. J. Meers, PRD **38**, 2317–2326 (1988).

[62] G. Heinzel, J. Mizuno, R. Schilling, W. Winkler, A. Rüdiger, and K. Danzmann, Physics Letters A **217**, 305–314 (1996).

[63] G. Vajente, in Advanced interferometers and the search for gravitational waves, 404, 57 (2014).

[64] A. Buonanno and Y. Chen, PRD **65**, 042001, `10.1103/PhysRevD.65.042001` (2002).

[65] A. Buonanno and Y. Chen, PRD **67**, 062002, `10.1103/PhysRevD.67.062002` (2003).

[66] A. Buonanno and Y. Chen, PRD **64**, 042006, `10.1103/PhysRevD.64.042006` (2001).

[67] M. Punturo et al., CQG **27**, 194002, `10.1088/0264-9381/27/19/194002` (2010).

[68] P. Fritschel, D. Coyne, et al., dcc.ligo.org/T010075, git.ligo.org/gwinc/pygwinc.

[69] D. Shoemaker et al., dcc.ligo.org/LIGO-T0900288.

[70] B. P. Abbott *et al.* (LIGO and Virgo Scientific Collaboration), PRL **116**, 061102, `10.1103/PhysRevLett.116.061102` (2016).

[71] J. Harms, Y. Chen, S. Chelkowski, A. Franzen, H. Vahlbruch, K. Danzmann, and R. Schnabel, PRD **68**, 042001, `10.1103/PhysRevD.68.042001` (2003).

[72] A. Buonanno and Y. Chen, PRD **69**, 102004, `10.1103/PhysRevD.69.102004` (2004).

[73] D. Coe, (2009).

[74] B. P. Abbott *et al.* (LIGO and Virgo Scientific Collaboration), PRL **119**, 161101, `10.1103/PhysRevLett.119.161101` (2017).

[75] B. P. Abbott *et al.* (LIGO and Virgo Scientific Collaboration), PRL **116**, 221101, `10.1103/PhysRevLett.116.221101` (2016).

[76] E. Berti, A. Buonanno, and C. M. Will, PRD **71**, 084025, `10.1103/PhysRevD.71.084025` (2005).

[77] A. Mangiagli, A. Klein, A. Sesana, E. Barausse, and M. Colpi, (2018).

[78] R. L. Ward, "Length sensing and control of a prototype advanced interferometric gravitational wave detector", PhD thesis (Caltech, 2010), `http://thesis.library.caltech.edu/5836/`.

[79] A. Thüring, C. Gräf, H. Vahlbruch, M. Mehmet, K. Danzmann, and R. Schnabel, Optics Letters **34**, 824 (2009).

[80] P. Purdue and Y. Chen, PRD **66**, 122004, `10.1103/PhysRevD.66.122004` (2002).

Chapter 5

TESTING GR WITH GW PROPAGATION

Gravitational wave dispersion and propagation has been a longstanding examination of GR since LIGO made the first detection of GWs and has remained a fundamental test in each observation run [1–4]. Comparison tests with EM counterparts have also been integral in binary neutron star systems [5, 6]. Generally, the primary approaches at investigating beyond-GR effects in GW dispersion have fallen into two categories: classical speed propagation [7–9] and effective field theoretical approaches [10, 11]. Both have relied on explicit WKB methods. The first section will discuss these approaches, with emphasis on the classical speed approach as applied to tests of Lorentz symmetry. Primarily, inclusion of anisoptropic coefficients in the dispersion will be investigated. See e.g., [12, 13] for work that also studies coefficients that break isoptropy in GW events, where the model here takes a parameterized approach to such models. Then in Section 5.3 a new approach that does not rely on classical propagation speed or explicit WKB methods will be presented, yet still relies on short wavelength approximations. This new result will be applied to a specific testing model in Ch. 6. Finally, a discussion on polarization dynamics will be discussed.

5.1 Classical Propagation Speed

In this section we work with the non-dissipative coefficients in the dispersion.

Isotropic and Scale-independent Dispersion Relations

A generic dispersion can be written as,

$$\omega^2 = a^2(t)(k^\chi)^2 + \Omega_{\mathrm{bGR}}(k^\mu), \tag{5.1}$$

where we include a beyond-GR dispersing parameter $\Omega_{\mathrm{bGR}}(k^\mu)$ and the GW's wave vector $k^\mu = (\omega, k^\chi, 0, 0)$ propagates radially from the source to the observer on a FRLW background,

$$ds^2 = -dt^2 + a^2(t)d\chi^2. \tag{5.2}$$

In an expanding universe ω and k^χ are not constants, rather due to killing tensor $K_{\mu\nu} = a^2(t)(g_{\mu\nu} + u_\mu u_\nu)$, where $u^\mu = (1, 0, 0, 0)$, the quantity $K_{\mu\nu}k^\mu k^\nu = (a^2(t)k^\chi)^2 = k_\chi^2$ is constant with respect to time t. Two implicit solutions then stem from the dispersion,

$$\begin{aligned} \omega(t;k_\chi) &= +\sqrt{a^2(t)(k^\chi)^2+\Omega_{\mathrm{bGR}}(k^\mu)}, \\ k^\chi(\omega;k_\chi) &= -a^{-1}(t)\sqrt{\omega^2-\Omega_{\mathrm{bGR}}(k^\mu)}, \end{aligned} \tag{5.3}$$

where the sign is chosen according to $\omega > 0$. Note that the form of our dispersion relation here maintains isotropy, and evolves with the age of the universe in a specific way. Some of these assumptions will be relaxed later in this section.

Wavepacket Propagation

Now consider a wave packet emitted radially towards the observer from a source at coordinates (t_e, χ_e) and arriving at (t_a, χ_a). The classical group velocity is given by,

$$v_g(t;k_\chi) = \frac{d\chi}{d\lambda}\frac{d\lambda}{dt} = \frac{k^\chi}{k^t} = \frac{1}{a^2(t)}\frac{k_\chi}{\omega(t;k_\chi)} \tag{5.4}$$

with λ an affine parameter. Now let a wave packet of frequency ω' be emitted from (t'_e, χ'_e) with a second wave packet of frequency ω from (t_e, χ_e), where $t_e = t'_e + \Delta t_e$, $\chi_e = \chi'_e$, and Δt_e is small enough that $a(t)$ doesn't change. For each wave packet integrating over v_g provides,

$$\begin{aligned} \chi'_e &= \int_{t'_e}^{t'_a} dt\, v_g(t;k'_\chi), \\ \chi_e &= \int_{t'_e+\Delta t_e}^{t'_a+\Delta t_a} dt\, v_g(t;k_\chi), \end{aligned} \tag{5.5}$$

where substitutions $t_e = t'_e + \Delta t_e$ and $t_a = t'_a + \Delta t_a$ are made. The second term can be rewritten as,

$$\begin{aligned} \chi_e &= \left(\int_{t'_e}^{t'_a} dt - \int_{t'_e}^{t'_e+\Delta t_e} dt + \int_{t'_a}^{t'_a+\Delta t_a} dt\right) v_g(t;k_\chi) \\ &\approx \int_{t'_e}^{t'_a} dt\, v_g(t;k_\chi) + \Delta t_a v_g(t'_a;k_\chi) - \Delta t_e v_g(t'_e;k_\chi) \end{aligned} \tag{5.6}$$

where the last approximation uses the assumption $a(t)$ does not change much between $\Delta t_{e,a}$ separations. Here the condition $\chi_e = \chi'_e$ gives,

$$\begin{aligned}
\Delta t_a &= \frac{v_g(t'_e; k_\chi)}{v_g(t'_a; k_\chi)}\Delta t_e + \frac{1}{v_g(t'_a; k_\chi)} \int_{t'_e}^{t'_a} dt \, \left(v_g(t; k'_\chi) - v_g(t; k_\chi)\right) \\
&= (1+z)\Delta t_e - \frac{\omega(t'_a; k_\chi)}{k_\chi} \int_{t'_e}^{t'_a} dt \, a^{-2}(t) \left(\frac{k'_\chi}{\omega(t; k'_\chi)} - \frac{k_\chi}{\omega(t; k_\chi)}\right) \qquad (5.7)
\end{aligned}$$

where expressions for v_g and $1+z = a(t_a)/a(t_e) = \omega(t_e)/\omega(t_a)$ have been substituted and the present scale factor defined to be unity $a(t_a) = a_0 = 1$.

Assuming small departures from GR: $\Omega_{\mathrm{bGR}}(k^\mu)/(k^\chi k_\chi)^{1/2} \ll 1$, we can expand around small perturbations of the usual GR result,

$$\begin{aligned}
k_\chi &\approx -\omega(t_a; k_\chi)\left(1 + \delta_{k_\chi}(t; \omega_a)\right), \\
\omega(t; k_\chi) &\approx -\frac{k_\chi}{a(t)}\left(1 + \delta_\omega(t; \omega_a)\right). \qquad (5.8)
\end{aligned}$$

Dimensionless parameters $\delta_{k_\chi}, \delta_\omega$ characterize small deviations from GR. Substituting respective values allows to rewrite this as,

$$\Delta t_a \approx (1+z)\Delta t_e + \int_{t'_e}^{t'_a} dt \, a^{-1}(t) \left(\delta_\omega(t; \omega_a) - \delta_\omega(t; \omega'_a)\right) \qquad (5.9)$$

where in the last approximation we've used the assumption $\delta_\omega \ll 1$.

The shape of a GW signals can be written in terms of an amplitude and phase: $\tilde{h}(f) = \mathcal{A}(f)\exp[i\Psi(f)]$, where for a binary system,

$$\Psi(f) = 2\pi \int_{f_{c,a}}^{f_a} \left(t_a - t_{a,c}\right) d\tilde{f}_a + 2\pi f_a t_{c,a} + \Psi_0 \qquad (5.10)$$

Recognizing that $\Delta t_a = t_a - t_{c,a}$ and substituting (5.9),

$$\begin{aligned}
\Psi(f) &= 2\pi \int_{f_{c,e}}^{f_e} d\tilde{f}_e \Delta t_e + 2\pi \int_{f_{c,a}}^{f_a} d\tilde{f}_a \int_{t'_e}^{t'_a} dt \, a^{-1}(t) \left(\delta_f(t; f_a) - \delta_f(t; f'_a)\right) \\
&\quad + 2\pi f_a t_{c,a} + \Psi_0 \qquad (5.11)
\end{aligned}$$

where in the second expression we redefine the integral as being over the emitted frequencies and use $\delta_\omega(t; \omega) = \delta_f(t; 2\pi f)$. Easing on notation we have,

$$\Psi(f) = \Psi_{\mathrm{GR}}(f) + \Delta\Psi(f), \qquad (5.12)$$

where,

$$\Delta\Psi(f) = \int_{f_c}^{f} d\tilde{f} \int_{t_e}^{t_a} dt\, \frac{2\pi}{a(t)} \left(\delta_f(t;\tilde{f}) - \delta_f(t;f_c)\right) \tag{5.13}$$

Using the above expression we can solve for ω from the (possible) polynomial of the dispersion Eq. (5.1) which requires replacement of $k_\chi \to 2\pi f$ in $\delta_f(t;k_\chi)$ to keep corrections to first-order. This holds true only under the assumption we work to first-order in deviations to the phase: $\delta_\omega(t;\omega_a) = \delta_\omega(t;k_\chi = \omega_a)$. Here we let $\delta_\omega(t;k_\chi) \equiv \epsilon f(t;k_\chi)$, for small ϵ so that we have $\omega \approx \omega_{\mathrm{GR}}(1+\epsilon f(t;k_\chi))$. Performing another expansion $k_\chi \approx k_{\chi,\mathrm{GR}}(1+\epsilon g(\omega_a)) = \omega_a(1+\epsilon g(\omega_a))$ resulting in,

$$\begin{aligned}
\omega &\approx \omega_{\mathrm{GR}}\left(1+\epsilon f\left[t;\omega_a\left(1+\epsilon g\left(\omega_a\right)\right)\right]\right)\\
&\approx \omega_{\mathrm{GR}}\left(1+\epsilon f\left(t;\omega_a\right)\left[1+\epsilon h\left(t;\omega_a\right)\right]\right)\\
&= \omega_{\mathrm{GR}}\left(1+\epsilon f\left(t;\omega_a\right)+O(\epsilon^2)\right)\\
&\approx \omega_{\mathrm{GR}}(1+\delta_\omega(t;\omega_a))
\end{aligned} \tag{5.14}$$

which is to first-order in ϵ and in the second approximation $f\left(t;\omega_a\left(1+\epsilon g\left(\omega_a\right)\right)\right) \approx f\left(t;\omega_a\right)\left(1+\epsilon h\left(t;\omega_a\right)\right)$ is used. Note that above we use functions derived from the appropriate series expansion:

$$f(t;k_\chi) = \left.\frac{\partial\omega}{\partial\epsilon}\right|_{\epsilon=0}, \quad g(\omega_a) = \left.\frac{\partial k_\chi}{\partial\epsilon}\right|_{\epsilon=0}, \quad h(t;\omega_a) = \left.\frac{\partial f(t;k_\chi)}{\partial\epsilon}\right|_{\epsilon=0}. \tag{5.15}$$

As an example we can look at the massive graviton case where the dispersion then is: $\omega^2 = a^{-2}(t)k_\chi^2 + 4\pi^2\lambda_g^{-2}$. Note that the wave vector of the GW can also be written as $k^\chi = 2\pi\lambda_{\mathrm{GW}}^{-1}$,

$$\omega \approx \omega_{\mathrm{GR}}\left(1+\frac{1}{2}a^{-2}(t)\left(\frac{\lambda_{\mathrm{GW}}}{\lambda_g}\right)^2\right) \tag{5.16}$$

where $\omega_{\mathrm{GR}} = a^{-1}(t)k_\chi$ and we recall that $k_\chi = a^2(t)k^\chi = 2\pi a^2(t)\lambda_{\mathrm{GW}}^{-1}$. Here the expansion was done with the assumption $\lambda_{\mathrm{GW}} \ll \lambda_g$, which is valid based on λ_g constraints in the solar system and observed GW wavelengths (this acts as our ϵ expansion length scale).

More General Dispersion Relations

The above massive graviton scenario is a simple case that is valid to zeroth-order in the modified dispersion (5.1). In generalizing we see that we're working in a series expansions of both ω and k^χ. Our goal is to have the dispersion expressed as a series of the wave vector k^χ, i.e., $\omega(k) = k + Q(k)$ where Q is a polynomial in k. Generically this can be expressed on a Chebeyshev polynomial basis with spherical harmonics breaking isotropy,

$$Q(k) = k^s \sum_{nlm} a_{nlm} T_n(k) Y_{lm}(\hat{n}) \tag{5.17}$$

Here the generic dispersion is $\omega^2 = k^2 + \Omega_{\text{bGR}}(\vec{\zeta}; \omega, k) + O(k^p)$ with some cutoff power p. The accumulated phase effects will be expressed as: $\omega(k)D = kD + Q(k)D$ where it can be assumed $\Delta\Psi \lesssim 1 \Rightarrow Q(k) \lesssim 1/D$. Expanding $\Omega_{\text{bGR}}(\omega)$ about $\omega = k$ provides,

$$\Omega_{\text{bGR}}(\omega) = \Omega_{\text{bGR}}(k) + \left.\frac{\partial \Omega_{\text{bGR}}}{\partial \omega}\right|_{\omega=k} (\omega - k) + \cdots \tag{5.18}$$

Here $(\partial\Omega_{\text{bGR}}/\partial\omega)(\omega - k) \sim (\Omega_{\text{bGR}}/\omega)Q(k) \lesssim \Omega_{\text{bGR}}/\omega D$, where higher powers of ω are successfully suppressed terms assuming they arise from higher dynamics of the theory considered. As each successive term in the expansion is reduced a power of ω, coefficients remain at the scale originally suppressed. Thus, leading order in $\Omega_{\text{bGR}}(\omega)$ can be taken as the dominant effect. Here the perturbing deviations from GR can then be taken to be,

$$\omega(k) = \omega_{\text{GR}} \left(1 + \frac{1}{2} k^{-2} \sum_{nlm} a_{nlm} T_n(k) Y_{lm}(\hat{n})\right) \tag{5.19}$$

where each k in the polynomial is assumed to have radial propagation in an FRLW background, so $k \to k_\chi a^{-1}(t) = 2\pi f a^{-1}(t)$. In summary the perturbing, beyond-GR term is,

$$\delta_f(t; f) = \frac{1}{2} k^{-2} \sum_{nlm} a_{nlm} T_n(k) Y_{lm}(\hat{n}) \tag{5.20}$$

where $k = 2\pi f a^{-1}(t)$. The massive graviton is related to the first term a_{000}.

Note that the expansion coefficients a_{lmn} can also be time dependent, but evolves at a cosmological time scale, much longer than the period of the gravitational waves we consider.

5.2 Classical Propagation Speed Summary and Analysis

In the previous section the classical group velocity approach was discussed in detail. Here we summarize the results and consider a toy model investigating a coefficient that breaks isotropy.

Recall, for non-dissipative coefficients the modified waveform can be computed by considering the group velocity of GWs and looking at the difference in arrival time between wave packets emitted with delay Δt_e,

$$\Delta t_a = \Delta t_e(1+z) + \int \frac{dt}{a(t)} \left(\delta_\omega(t;\omega_a) - \delta_\omega(t;\omega'_a)\right). \tag{5.21}$$

Here Δt_a is the delay in arrival of two wave packets, while the dimensionless parameter δ_ω encodes modifications to the dispersion assuming small departures from GR. Also, $a(t)$ is the cosmological expansion parameter, z the redshift, ω_a is the GW frequency at arrival with primed quantities corresponding to the second emitted wave packet. Note that δ_ω comes from the implicit solution of the polynomial of for ω.

This frequency dependent delay Δt_a can be translated into a phase shift. For a waveform $\tilde{h}(f) = A(f)\exp[i\Psi(f)]$, the correction for nondissipative terms will be $\Psi(f) \to \Psi_{\mathrm{GR}}(f) + \Delta\Psi(f)$, where

$$\Delta\Psi(f) = \int_{f_c}^{f} \int_{t_e}^{t_a} dt d\tilde{f} \frac{2\pi}{a(t)} \left(\delta_f(t;\tilde{f}) - \delta_f(t;f_c)\right) \tag{5.22}$$

encapsulates the non-GR effects arising from the modified dispersion, where we have made the substitution $f = \omega/2\pi$ and f_c is the coalescing frequency when considering compact binaries. As a demonstration the left panel of Fig. 5.1 displays an inspiral-merger-ringdown (IMR) waveform with the extra phase shift arising from a modified dispersion of the form $-\omega^2 + |\vec{k}|^2 = -(m_g^2 + \hat{n}\cdot\vec{v})$, with $\hat{n}$ the wave's direction of propagation and $\vec{v}$ an arbitrary vector. The non-GR effects are largely exaggerated. The massive graviton and anisotropic terms are degenerate since they both present dependence $\Delta\Psi \propto D/f$. This exemplifies degeneracies that may exist in our dispersion and can be broken by coherently analyzing multiple detections. The right panel of Fig. 5.1 displays an example of an unnormalized posterior distribution of v_y, the projection of the anisotropic GR-violating term appearing in the modified dispersion with the dashed line marking the injected value. Here, $\hat{x} \equiv$ vernal equinox, $\hat{z} \equiv$ celestial north pole, and $\hat{y} = \hat{z}\times\hat{x}$. How well each component (v_x, v_y, v_z) can be measured depends on the location of the source.

5.3 Propagation in the Characteristic Formalism

In this section a new formalism for modified GW propagation is derived, which is independent of previous methods that use classical (particle) propagation speed

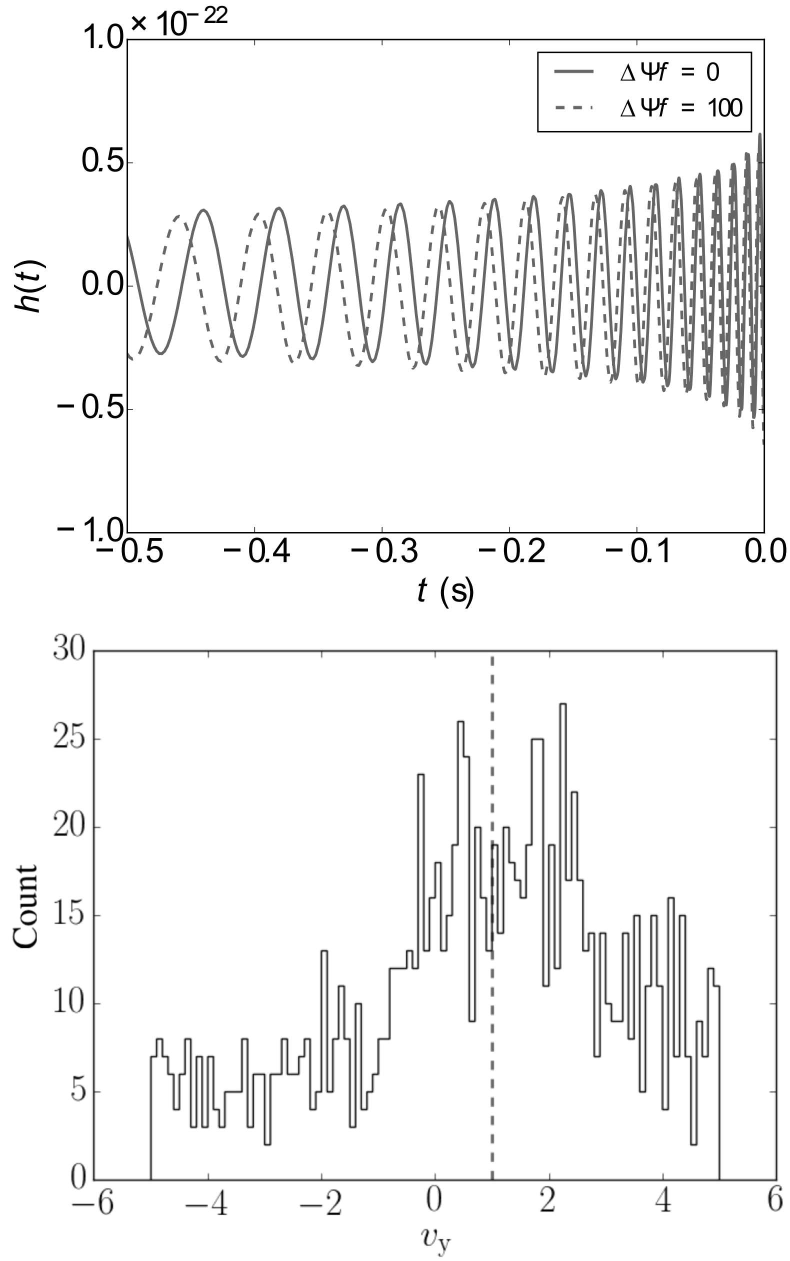

Figure 5.1: Toy model of a beyond-GR dispersion having directional dependence. Top: IMR signal of mock event for our toy model. The solid line represents the GR limit, while the dashed line corresponds to non-GR modifications. Bottom: Unnormalized posteriors for v_y projection for event generated from mock data with IMR PhenomPv2 of no spin assuming Advanced LIGO noise. The results are generated when the source location is known exactly; the distance is set to 410 Mpc.

and explicit WKB techniques. The derived dephasing employs a commonly implemented modified dispersion relation which models the behavior of beyond general relativistic effects like massive graviton and Lorentz violation

Assuming a FLRW spacetime in conformal time ($d\eta = dt/a$) the metric for the formalism with no spatial curvature is,

$$ds^2 = a^2(\eta)\left(-d\eta^2 + dr^2 + r^2(d\theta^2 + \sin^2\theta d\phi^2)\right). \tag{5.23}$$

In previous works [8, 9] the generic dispersion relation,

$$E^2 = p^2 + \sum_\alpha A_\alpha p^\alpha, \tag{5.24}$$

is extensively used in theoretical and observational studies. This can be converted into a wave equation, such that

$$E \rightarrow ia^{-1}\partial_\eta\,, \quad \mathbf{p} \rightarrow -ia^{-1}\partial_j. \tag{5.25}$$

Here the quantity A_α has the dimension of $\omega^{2-\alpha}$ for GW frequency $\omega = 2\pi f$. Note that in this case α is not a spacetime index.

Since this work will only be considering waves that propagate toward the direction of the earth, only the radial direction of propagation will be relevant. In this section, due to symmetry of the dispersion relation, polarization states of gravitational waves are unaffected, and both right- and left-circularly polarized waves propagate the same way. We can therefore use a single Φ to represent the strain of either polarization. The curvature coupling can be further ignored, which is negligible in the short-wavelength situation. The 1-D scalar wave equation can then be written as,

$$\Box\Phi = \sum_\alpha A_\alpha(\eta)\,(-ia^{-1}\partial_r)^\alpha\Phi. \tag{5.26}$$

Expanding the D'Alembertian results in,

$$\frac{1}{\sqrt{-g}}\partial_\mu(\sqrt{-g}g^{\mu\nu}\partial_\nu\Phi) = \sum_\alpha A_\alpha(\eta)(-ia^{-1}\partial_r)^\alpha\Phi. \tag{5.27}$$

Note that $g = -a^8 r^4 \sin^2\theta$. Now Φ can be redefined as,

$$\Psi \equiv ra\Phi, \tag{5.28}$$

which further simplifies the wave equation to,

$$-\partial_\eta^2\Psi + \partial_r^2\Psi = \sum_\alpha A_\alpha(\eta)(-i)^\alpha a^{-\alpha+2}\partial_r^\alpha\Psi. \tag{5.29}$$

Here terms that are powers of $\lambda_{\rm GW}/R_H$ have been ignored, where $\lambda_{\rm GW}$ is the GW wavelength and R_H is the Hubble distance. We have also ignored angular derivatives, which is justified for low-multipole waves propagating at large distances (far greater than the wavelength) in a homogeneous isotropic situation. [1]

In the conformal FRLW metric a transformation to (u, v)-space can then be done via,

$$u = \eta - r\,, \quad v = \eta + r, \tag{5.30}$$

resulting in,

$$\partial_\eta = \partial_u + \partial_v\,, \quad \partial_r = \partial_v - \partial_u\,. \tag{5.31}$$

This transformation immediately results in a simplfied version of Eq. (5.26) in (u, v)-space,

$$\partial_u \partial_v \Psi = -\frac{1}{4}\sum_\alpha A_\alpha(\eta)(-i)^\alpha a^{-\alpha+2}\partial_u^\alpha \Psi, \tag{5.32}$$

which as previously mentioned ignores $\lambda_{\rm GW}/R_H$ to positive powers.

As the waveform propagates in (u, v)-space as depicted in Fig. 5.2 it can be interpreted that its variation along u is much faster than variation along v. Basically, at each v, the dependence of Ψ on u is our gravitational waveform. To find the solution for the frequency domain waveform $\psi(\Omega, v)$ the Fourier representation of the waveform can be used,

$$\Psi(u, v) = \int \frac{d\Omega}{2\pi}\psi(\Omega, v)e^{i\Omega u}, \tag{5.33}$$

that, when inserted in Eq. (5.32), results in,

$$\partial_v \psi = \frac{i}{4}\sum_\alpha A_\alpha(\eta)\Omega^{\alpha-1}a^{-\alpha+2}\psi. \tag{5.34}$$

Here $\psi(\Omega, v)$ is the frequency domain GW (in conformal time) measured by comoving observers at spatial locations along the propagation path. The accumulated phase shift along v from source to observer can be summarized as,

$$\psi(\Omega, v_1) = \psi(\Omega, v_0)\exp\left(i\Delta\phi\right), \tag{5.35}$$

where $v_{0,1}$ are shown in Fig. 5.2. Integrating from $(0, 0)$ to (χ, χ), where χ is the comoving distance from the source to the observer, we will have $v = (\xi, \xi)$,

[1] Although we will later consider inhomogeneous/anisotropic screening, we will ignore gravitational-wave diffraction effects caused by that screening.

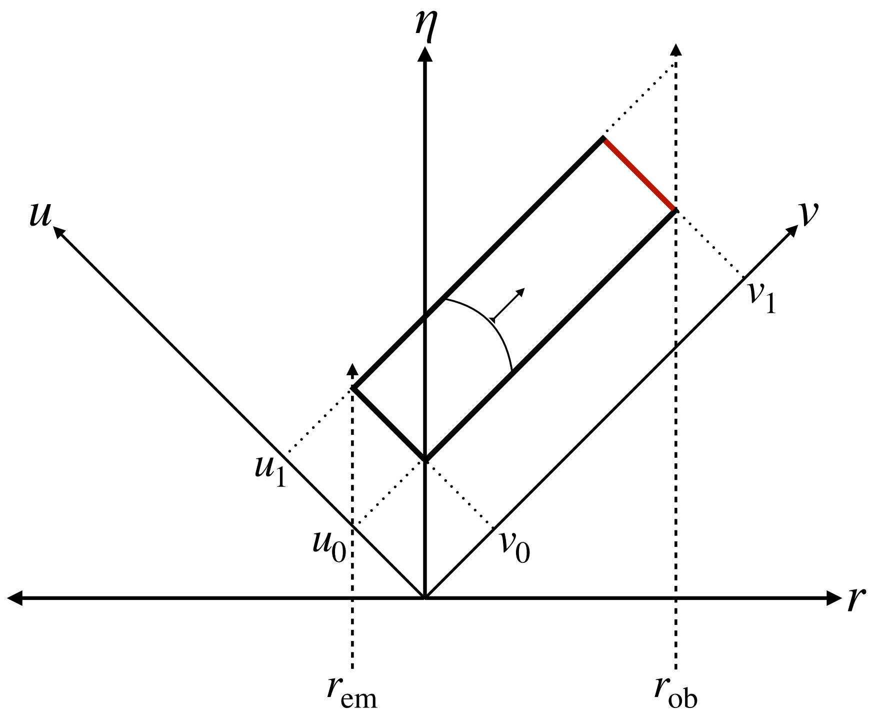

Figure 5.2: Example of (u, v)-space transformation and boundary conditions employed. The GW event is emitted at $r_{\rm em}$ and observed at $r_{\rm obs}$. Rapid variation along u represents the GW signal, whereas the accumulated variation along v represents the dephasing of the GW event.

$0 < \xi < \chi$, and the integral,

$$\Delta\phi = -\sum_{\alpha} \frac{1}{2} \left(\frac{\Omega}{a_0}\right)^{\alpha-1} \int_0^z \frac{A_\alpha(z')(1+z')^{\alpha-2}dz'}{H(z')}. \tag{5.36}$$

In this calculation, we did use $\lambda_{\rm GW}/R_H \ll 1$, but we did not have to use the technique for WKB explicitly. Here we arrived at a phase shift as a function of ω — as if phase velocity were used.

In the above expression a z-dependence was explicitly kept: $A_\alpha(z)$. In this manner a z dependence can be kept depending on what model is used for a weighted redshift in the integral, for example we can choose,

$$A_\alpha(z) = \sum_n A_\alpha^{(n)} (1+z)^n, \tag{5.37}$$

as a potential redshift-weighted model. [2] With this a modified distance measure can be defined, similar to Ref. [8],

$$D_\alpha^{(n)}(z) = (1+z)^{1-\alpha} \int_0^z \frac{(1+z')^{n+\alpha-2}}{H(z')} W(z')dz'. \tag{5.38}$$

[2] In general any reasonable redshift dependence can be chosen for the particular model assumed.

Here $W(z)$ is introduced and acts as a filter where in the usual modified distance $W(z) = 1$ and in the model of two screened galaxies it is a combination of Heaviside functions (see Ref. [9]). The exact model developed here for $W(z)$ will be motivated at the end of this section. We will then have,

$$\Delta\phi = -\frac{1}{2}\sum_{\alpha}\left(\frac{(1+z)\Omega}{a_0}\right)^{\alpha-1}\sum_{n} A_{\alpha}^{(n)} D_{\alpha}^{(n)}(z). \tag{5.39}$$

Let us look at each comoving observer along the path with increasing v. In terms of waveform $h(t, v)$ (ignoring $\lambda_{\rm GW}/R_H$ effects), we can write,

$$h(t, v) = \Psi(t/a, v), \tag{5.40}$$

therefore,

$$h(\omega, v) = \int \Psi\left(t/a(v), v\right) e^{-i\omega t} dt = a(v)\psi\left(a(v)\omega, v\right). \tag{5.41}$$

In this way, the frequency domain additional phase-shift obtained is given by

$$\Delta\phi = -\frac{1}{2}\sum_{\alpha}\left((1+z)\omega\right)^{\alpha-1}\sum_{n} A_{\alpha}^{(n)} D_{\alpha}^{(n)}(z). \tag{5.42}$$

Here $\omega = 2\pi f$ is the GW frequency measured on the ground. This is the phase shift in the otherwise GR waveform,

$$h_{\rm bGR} = h_{\rm GR} e^{i\Delta\phi}. \tag{5.43}$$

Specifically for lowest-order bGR correction ($\alpha = 0, n = 0$), i.e., the redshift-independent graviton mass contribution, the phase shift reduces to,

$$\Delta\phi_{MG} = -\frac{\pi D_0^{(0)}}{\lambda_g^2 (1+z) f}, \tag{5.44}$$

noting $\lambda_g = 2\pi/m$ (recall $\hbar$ and c are set to unity). This is in agreement with previous independent methods [8, 10].

5.4 Polarization Dynamics from Propagation

The analysis in this section has so far ignored polarization dynamics. In the most generic beyond-GR theory up to six polarization states can exist [14]. See figure 5.3 for a breakdown of these polarization states.

One dynamical feature of a GW's polarization is the rotation of its polarization through propagation in a beyond-GR universe, a common example being induced

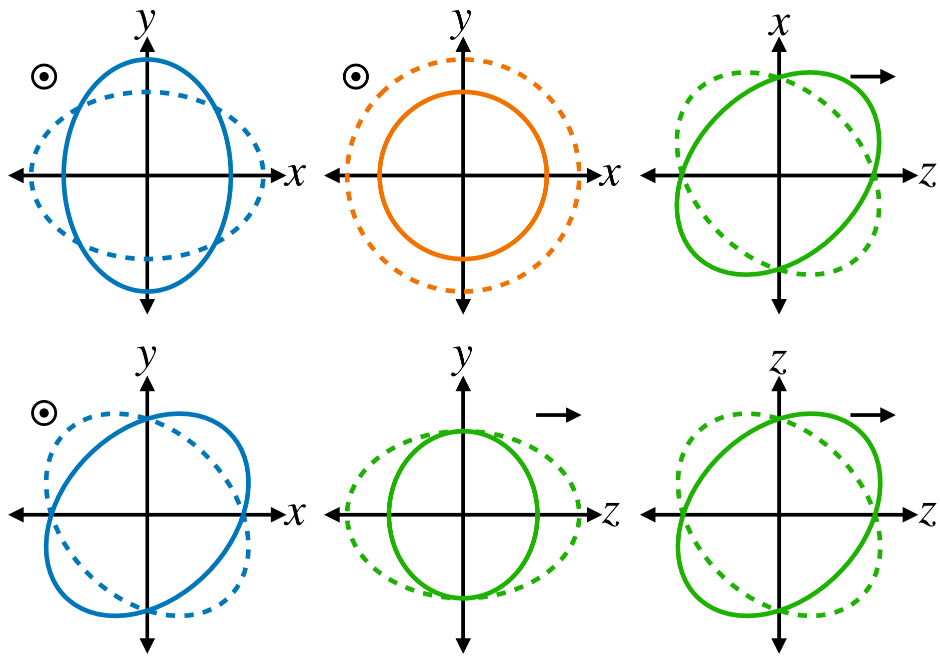

Figure 5.3: Six polarization states that can exist in the most generic beyond-GR theory. A GW propagates in the positive z-direction with transverse waves, e.g., GWs from the GR result, varying in the xy-plane. States are the GR plus-cross polarization (far left in blue), the breathing/longitudinal polarization (middle), and two vector polarizations (far right).

by parity violation [15, 16]. Assuming only two degrees of freedom $(+, \times)$ the TT and Lorenz gauge is assumed with notation suppressed so that $h^a_{\mu\nu}$ and $h^e_{\mu\nu}$ represent the solution for arrival and emission, respectively. Solutions can be expressed as a linear combination of modes as right-handed and left-handedness, i.e., $h^e_{L,R} = h^e_+ \pm h^e_\times$, which holds in both time and Fourier domain. Throughout its propagation the combination will be rotated by an angle $k_{L,R}(\omega)D$ which produces the observed combination $h^a_{L,R} = h^e_{L,R} e^{ik_{L,R}(\omega)D}$ at the detectors. In terms of $(+, \times)$ polarizations we have,

$$\begin{bmatrix} h^a_+ \\ h^a_\times \end{bmatrix} = \begin{bmatrix} u & iv \\ -iv & u \end{bmatrix} \begin{bmatrix} h^e_+ \\ h^e_\times \end{bmatrix} \tag{5.45}$$

where $u = (e^{ik_L(\omega)D} + e^{ik_R(\omega)D})/2$ and $v = (e^{ik_L(\omega)D} - e^{ik_R(\omega)D})/2$ with $k_{L,R}(\omega) \in \mathbb{C}$. When $k_{L,R}(\omega)$ are imaginary attenuation occurs and produces amplitude birefringence and when $k_{L,R}(\omega)$ are real rotational birefringence occurs. For the projection matrix above we have eigenvalues $e^{ik_{L,R}(\omega)D}$ with eigenvectors $(\pm i, 1)$. This is a common result and specific examples are worked out in parity violating theories.

The rotation procedure above occurs with a projection operator mixing the polarization states in some beyond-GR universe following some modified dispersion. One natural approach is to relax the condition of just $+, \times$-polarization and include scenarios when beyond-GR states are present. This has been explored in Ref. [11] in the effective field theory approach to modified propagation with other work considering theories with added degrees of freedom in bigravity [17]. What arises is helicity state oscillation, an analogy to neutrino oscillation. In high-energy physics terminology, this allows the graviton to oscillate between various helicity states, those helicity states being: h_b (helicity-0 breathing mode), h_l (helicity-0 longitudinal mode), h_{v_1,v_2} (helicity-1 vector modes), $h_{+,\times}$ (helicity-2 GR modes).

Now we discuss methods to parameterize these dynamics. Polarization dynamics can be broken generically into several categories with projection operator $\mathcal{T}^{\alpha\beta}_{\ \ \mu\nu}$,

$$h_a^{\alpha\beta} = \left(\mathcal{T}^{\alpha\beta}_{(\text{phys})\mu\nu} + \mathcal{T}^{\alpha\beta}_{(\text{GR})\mu\nu} + \mathcal{T}^{\alpha\beta}_{(\text{bGR})\mu\nu}\right) h^e_{\mu\nu}. \tag{5.46}$$

Recall e is emission and a is arrival. Here $\mathcal{T}^{\alpha\beta}_{(\text{phys})\mu\nu}$ can be the physical nature of the system, e.g., type of source, orientation of the source and/or detector, etc. Operator $\mathcal{T}^{\alpha\beta}_{(\text{GR})\mu\nu}$ encapsulates GR phenomenon like polarization rotation due to galaxy rotation, GW lensing, etc (note when no GR-induced phenomenon is present $\mathcal{T}^{\alpha\beta}_{(\text{GR})\mu\nu} = \delta^\alpha_\mu \delta^\beta_\nu$). Finally, $\mathcal{T}^{\alpha\beta}_{(\text{bGR})\mu\nu}$ are beyond-GR effects such as that induced by parity violation presented in Eq 5.45 or what has been called helicity state mixing. Letting $h_{\mu\nu}$ be plane-wave components of a GW, one can upgrade the GR limit to a generic projection operator by taking into account additional degrees of freedom,

$$\mathcal{T}^{\alpha\beta}_{(\text{bGR})\mu\nu} \propto \sum_p \mathbb{P}^{\alpha\beta}_{(p)\,\mu\nu}, \tag{5.47}$$

where p is summed over possible polarizations (GR and beyond-GR). Next, decompose the modes of the metric perturbations, those corresponding to metric terms in the longitudinal directions, transverse directions, two in orthogonal planes that include the longitudinal directions. The six nonzero terms can be categorized as,

$$(h_{zz}), (h_{xx}, h_{xy}, h_{yx}, h_{yy}), (h_{xz}, h_{yz}).$$

Fluctuations can then be expressed in terms of its polarization tensor,

$$\sum_p \mathbb{P}^{\alpha\beta}_{(p)\,\mu\nu} h^e_{\alpha\beta} \to \sum_p \mathbb{P}^{\alpha\beta}_{(p)\,\mu\nu} e^A_{\alpha\beta} h^e_A \tag{5.48}$$

where for now the emission process only has $+, \times$ polarizations ($e^A_{\alpha\beta}$ is the polarization tensor for the 2-modes $A = +, \times$). This process allows the extraction of a new set of $+, \times$ polarizations resulting from eigenmode coupling between the metric components throughout propagation. Furthermore, to consider additional propagation modes due to generic functions $f^{(p)}_{\mu\nu}(k)$ (as functions of $k(\omega)$), the projection operator results in,

$$\sum_p f^{(p)}_{\mu\nu} e^{ik_{(p)}L} f^{\alpha\beta}_{(p)} e^A_{\alpha\beta} h^e_A, \tag{5.49}$$

with $A = +, \times$. Note that when $e^{ik_{(p)}L} = 1$, then $f^{(p)}_{\mu\nu} f^{\alpha\beta}_{(p)} = \delta^\alpha_\mu \delta^\beta_\nu$. In terms of the arriving signal we can then construct the final result,

$$h^a_{p'} = \frac{1}{2} \sum_{p \neq p'} \sum_A e^{\mu\nu}_{p'} \mathbb{P}^{\alpha\beta}_{(p)\,\mu\nu} e^A_{\alpha\beta} h^e_A \tag{5.50}$$

where $A = +, \times$ and $p, p' = +, \times, b, l, v_1, v_2$ with,

$$\mathbb{P}^{\alpha\beta}_{(p)\,\mu\nu} = f^{(p)}_{\mu\nu} e^{ik_{(p)}L} f^{\alpha\beta}_{(p)} \tag{5.51}$$

Recall that $e^{\mu\nu}_p$ basis of the respective polarization p.

The form (5.50) allows helicity oscillation to occur during propagation via mode couplings and also explicitly sums out to,

$$h^a_{p'} = \frac{1}{2} \sum_{p \neq p'} e^{\mu\nu}_{p'} \left[\left(\mathbb{P}^{11}_{(p)\,\mu\nu} - \mathbb{P}^{22}_{(p)\,\mu\nu} \right) h^e_+ + \left(\mathbb{P}^{12}_{(p)\,\mu\nu} + \mathbb{P}^{21}_{(p)\,\mu\nu} \right) h^e_\times \right]. \tag{5.52}$$

Note that in the GR-limit: $e^{ik_{(p)}L} = 1$, so $f^{(p)}_{\mu\nu} f^{\alpha\beta}_{(p)} = \delta^\alpha_\mu \delta^\beta_\nu$ and equation (5.50) becomes,

$$h^{\mathrm{GR},a}_A = \frac{1}{2} \left[(e^{11}_A - e^{22}_A) h^e_+ + (e^{12}_A + e^{21}_A) h^e_\times \right] \tag{5.53}$$

for the standard choice of $e^{\mu\nu}_p$ with $A = +, \times$.

References

[1] B. P. Abbott *et al.* (LIGO and Virgo Scientific Collaboration), PRL **116**, 221101, `10.1103/PhysRevLett.116.221101` (2016).

[2] B. P. Abbott *et al.* (LIGO Collaboration) (LIGO Scientific Collaboration and Virgo Collaboration), PRD **100**, 104036, `10.1103/PhysRevD.100.104036` (2019).

[3] B. P. Abbott *et al.* (LIGO Collaboration) (LIGO Scientific Collaboration and Virgo Collaboration), PRD **103**, 122002, `10.1103/PhysRevD.103.122002` (2021).

[4] B. P. Abbott *et al.* (LIGO Collaboration), arXiv e-prints, arXiv:2112.06861 (2021).

[5] B. P. Abbott *et al.* (LIGO Collaboration), ApJL **848**, L13, `10.3847/2041-8213/aa920c` (2017).

[6] B. P. Abbott *et al.* (LIGO Scientific Collaboration and Virgo Collaboration), PRL **123**, 011102, `10.1103/PhysRevLett.123.011102` (2019).

[7] C. M. Will, PRD **57**, 2061–2068 (1998).

[8] S. Mirshekari, N. Yunes, and C. M. Will, PRD **85**, 024041, `10.1103/PhysRevD.85.024041` (2012).

[9] S. Perkins and N. Yunes, CQG **36**, 055013, `10.1088/1361-6382/aafce6` (2019).

[10] A. Nishizawa, PRD **97**, 104037, `10.1103/PhysRevD.97.104037` (2018).

[11] J. M. Ezquiaga, W. Hu, M. Lagos, and M.-X. Lin, JCAP **2021**, 048, `10.1088/1475-7516/2021/11/048` (2021).

[12] V. A. Kostelecký and J. D. Tasson, Physics Letters B **749**, 551–559 (2015).

[13] V. A. Kostelecký and M. Mewes, Physics Letters B **757**, 510–514 (2016).

[14] C. M. Will, LRR **17**, 4, `10.12942/lrr-2014-4` (2014).

[15] N. Yunes, R. O'Shaughnessy, B. J. Owen, and S. Alexander, PRD **82**, 064017, `10.1103/PhysRevD.82.064017` (2010).

[16] A. Nishizawa and T. Kobayashi, PRD **98**, 124018, `10.1103/PhysRevD.98.124018` (2018).

[17] T. Narikawa, K. Ueno, H. Tagoshi, T. Tanaka, N. Kanda, and T. Nakamura, PRD **91**, 062007, `10.1103/PhysRevD.91.062007` (2015).

Chapter 6

MODEL TO CONSTRAIN VAINSHTEIN SCREENING IN MASSIVE GRAVITON THEORIES

As the LIGO-Virgo Scientific Collaboration completes analysis of its third observation run, the results conclude general relativity (GR) as the favored theory [1–4]. This is expected as LIGO-Virgo begins to make their first astrophysical discoveries [5–8]. Testing strategies and analysis techniques continue to improve alongside detector upgrades, eventually culminating in third-generation detectors (e.g., Cosmic Explorer [9]) in the 2030s which will initiate precision tests of GR at cosmological scales.

Since first detections of gravitational waves (GWs) a common beyond-GR constraint has been the Compton wavelength associated with a massive carrier for gravitational interactions [10, 11]. Massive graviton constraints through GW observations have been competitive with existing and improved weak-field/solar system tests [10, 12]. For GWs the primary constraint has relied on two approaches in deriving a dispersion to GWs [13–17]. A first approach in deriving the observable signatures in GWs relied on classical propagation speeds and a stationary phase approximation [13]. This approach was further implemented in generic GW dispersion and recently addressed the effect of potentially *screened* regions [14, 18]. Other methods explicitly used WKB techniques in an effective field theory to arrive at the same result [15–17]. Recently similar approaches investigated parameterized phenomenological models and their coupled equations of motion also using a WKB formalism [19].

In Ch. 5 a new method was presented that arrives at a phase shift as a function of GW frequency with a distinct phase velocity approach and without explicit WKB methods. Results are in agreement with previous treatments and methods hold at cosmological scales. Within this characteristic formalism a screening of the graviton mass (suppression of beyond GR effects near matter distributions) is analyzed with Cosmic Explorer as the GW propagates to the observer through multiple galaxies.

Null results in weak-field tests can also be explained by screening in local regimes. See Ref. [20] for discussions on this. Furthermore, even scalar radiation being screened outside the GW source host galaxy has been motivated in some models [21]. In the instance this holds for GWs in various theories of massive graviton the wave would propagate in the radiation regime, obeying GR in the host galaxy, and accumulate a phase shift due to a massive graviton outside the host's screening region. Yet, when within the Vainshtein radii R_{v_i} of galaxy mass distributions the signatures of a massive graviton in the wave's dispersion would again be suppressed. Thus, accounting for screening caused by galaxies located in between the source and the Earth, near the path of the wave, is essential in building an accurate massive graviton model at cosmological scales. In this chapter screening effects are modeled agnostic to the particular massive graviton theory, as long as it incorporates the Vainshtein mechanism necessary for screening [22, 23].

In our simplified model galaxy distributions are assumed to have equal screening (proper distance) radii R_v (see figure 6.1), whereas in specific models the screening radii depends on the galaxy mass [11]. Early work in Ref. [18] considers the GW source host galaxy and the Milky Way as a catalyst for screening regions. For GW sources in our local universe, this screening model is reasonable, as the probability of having multiple galaxies on the path is small for a low redshift source. This condition, however, does not hold for the high-redshift GW sources we expect to observe with third generation GW detectors [24]. Therefore it is important to evaluate graviton mass and galaxy screening signature in the context of a realistic galaxy population model. With the aid of the next generation optical surveys, our understanding of the galaxy distribution in the universe will improve dramatically, allowing for even more fruitful joint studies on GW and matter distribution in the universe [see, e.g., [25–27]]. As optical surveys and GW detection generally target different aspects of astrophysical processes, joint studies open the possibility to break degeneracies within physical models (see e.g., Ref. [28]). In the particular case of graviton mass screening, we show that modeling galaxy distribution partially breaks the degeneracy between graviton mass and screening radius and allows for better constraint on their respective values.

Using characteristic formalism for propagation from Ch. 5 screening is explored in this chapter. Section 6.1 introduces the galaxy population implemented and the model used for massive graviton screening. Section 6.2 presents results in analyzing the screened massive graviton model with Section 6.3 discussing the results and further work. This chapter assumes the metric has signature $(-,+,+,+)$, Greek letters run over spacetime indices, Latin letters run over spatial indices, and geometrized units are used including $\hbar = 1$ unless otherwise specified.

To motivate the $W(z)$ factor in Eq. 5.38, massive graviton theories have had suc-

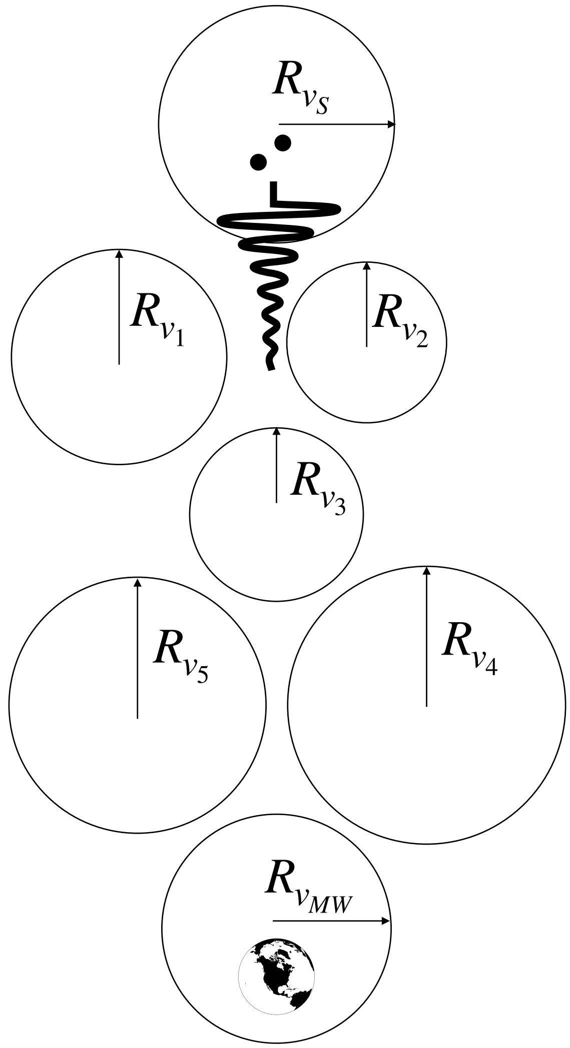

Figure 6.1: Example of screening radii R_{v_i} from multiple matter distributions between source and observer. The source/host galaxy emits a GW signal from a binary merger and the signal propagates in the radiation regime entering multiple screening radii. For CE the matter distributions stem from intermittent galaxies ($i = 1, \ldots, 5$) including the source (S) and observer galaxy (MW). Based on the particular theory R_{v_i} has varying size based on galaxy mass. The analysis employed in this work assumes $R_{v_i} = R_v$ is fixed and the source/observer galaxy excluded for demonstration purposes. See text for discussion.

cessful constraints in weak-field regimes. Yet, these constrained effects could be influenced by corrections to the linear-order GR solutions in the $m_g \to 0$ limit. Here the Vainshtein mechanism rectifies this GR deviation, appearing in various massive graviton theories. [1] Although the Vainshtein mechanism has only been worked out for static, spherically symmetric spacetimes, there remains work to be done. For example, work remains on its behavior with dynamical systems and there exists evidence for its effects on scalar waves propagating near the screening radius [21]. For spherical sources the mechanism to screen the effects of a massive graviton extend out to the Vainshtein radius,

$$R_v = R_s^a \lambda\!\!\!^{-}{}_g^b, \tag{6.1}$$

where a, b are theory dependent, R_s the Schwarzschild radius (of the matter distribution), and $\lambda\!\!\!^{-}$ the reduced Compton wavelength. [2] The $W(z)$ factor accounts for signals following paths displayed in figure 6.1. In this study R_v is fixed to one value for all galaxies analyzed to simplify the analysis, so $W(z)$ can be thought of as a top-hat filter in this study. In general any continuous function can be used, for example other functions can account for the transition stiffness going from inside to outside R_v. Theory specific analytic or numerical forms of $W(z)$ can also be used in such a model. Computational work continues to advance these studies [see, e.g., [29–31]] with additional work looking at cosmic web structures for screening mechanisms [32].

6.1 Multi-galaxy Screening

In this subsection, we discuss details on the galaxy population model and the specific form of the distance measure $D_0^{(0)}$. As mentioned, the redshift integration range covers the unscreened fraction of the graviton propagation path. In this chapter, we model the screening radius in terms of proper distance which along the radial direction is given by, [see, e.g., [33]],

$$\Delta D_p = \int_z^{z+\Delta z} \frac{1}{(1+z')H(z')} dz'. \tag{6.2}$$

[1] The essential concept is that the helicity-0 mode couples to matter both at linear and non-linear orders, where its non-linearities lead to the mechanism that screens the effects in the presence of matter which further evades solar system bounds [11, 23].

[2] $(a, b) = (1/3, 2/3)$ in dRGT/bigravity and $(a, b) = (1/5, 4/5)$ in non-linear Fierz-Pauli [11, 22].

The derivative of the proper distance and $D_0^{(0)}$ with respect to redshift is approximated (in the $\delta z \to 0$ limit),

$$
\begin{aligned}
\frac{dD_p(z_0)}{dz} &\approx \frac{1}{(1+z_0)H(z_0)}, \\
\frac{dD_0^{(0)}(z_0)}{dz} &\approx \frac{1}{(1+z_0)H(z_0)}.
\end{aligned}
\tag{6.3}
$$

In this proof-of-concept model, we model the screening region as spheres centered on each galaxy with a galaxy-independent screening radius, R_v. In Sec. 6.3, we elaborate on the effect of more realistic modeling. Since the screening radius is small compared with cosmological distance, the screening effect on the distance measure is approximated as,

$$
\Delta D_0^{(0)} \approx \frac{dD_0^{(0)}}{dz}\Delta z \approx \Delta D_p. \tag{6.4}
$$

The distance measure can then be explicitly written as,

$$
\begin{aligned}
D_0^{(0)} = (1+z)\int_0^z \frac{(1+z')^{-2}}{H(z')}dz' \\
- 2\sum_i \sqrt{R_v^2 - dr_i^2},
\end{aligned}
\tag{6.5}
$$

where i is the index of screening galaxies and dr_i is the proper distance between the galaxy center and the graviton propagation path. Since we do not consider additional effects on the GW within the screened region, the sum in Eqn. 6.5 does not double-count regions where galaxy screening regions overlap.

To model the galaxy population, we adopt a phenomenological model from local universe observations and numerical simulations. The local universe galaxy number density is given in the form of a modified Schechter function, fitted from SDSS data [34],

$$
\Psi(\sigma_v) = \phi_* \left(\frac{\sigma_v}{\sigma_*}\right)^{\alpha} \exp\left[-\left(\frac{\sigma_v}{\sigma_*}\right)^{\beta}\right] \frac{\beta}{\sigma_v \Gamma(\alpha/\beta)}, \tag{6.6}
$$

where $\phi_* = 8.0 \times 10^{-3} h^3\ \mathrm{Mpc}^{-3}$, $\sigma_* = 161$ km/s, $\alpha = 2.32$ and $\beta = 2.67$. The parameter h is the Hubble parameter. The galaxy population at larger redshift values is given by,

$$
\Psi(\sigma_v, z) = \Psi(\sigma_v, 0)\frac{\Psi_{\mathrm{hyd}}(\sigma_v, z)}{\Psi_{\mathrm{hyd}}(\sigma_v, 0)}, \tag{6.7}
$$

where $\Psi(\sigma_v, 0)$ is the local galaxy population given in Eqn. 6.6, and $\Psi_{\mathrm{hyd}}(\sigma_v, z)$ follows a phenomenological model fitted from the data of the hydrodynamic simulation, Illustris [35]. We further assume that galaxies are isotropically distributed.

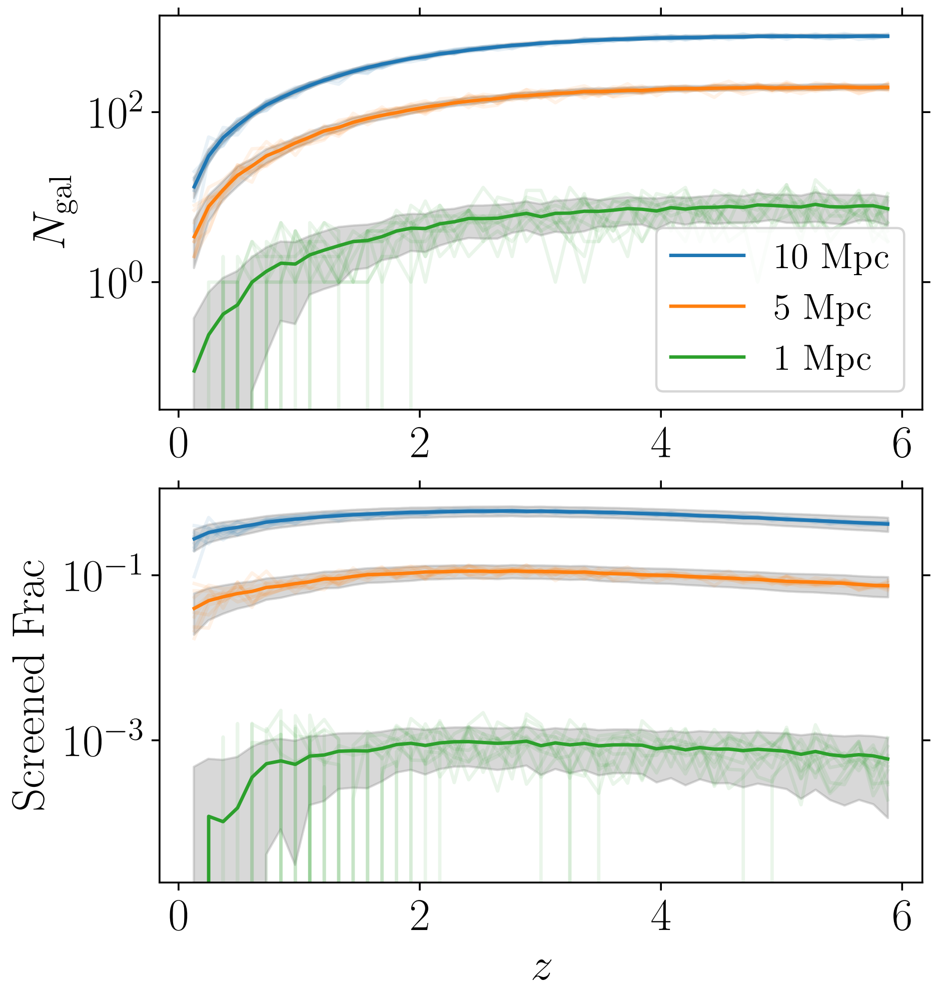

Figure 6.2: Screening under various screening radii. Top: Average number of screening galaxies (regardless of how much screening each does) given various screening radii specified in the legend. The average is taken from 100 galaxy realizations in each case, and several example realizations are shown by the lighter color lines. Shaded grey region represents 1σ errors. Bottom: Corresponding fraction of screened propagation path length. The GW sources redshift starts from $z = 0.13$, therefore the fractions do not all start from 0. Again, shaded grey region represents 1σ errors.

In Fig. 6.2, the top panel shows the average number of screening galaxies from 100 galaxy realizations as a function of GW source redshift for $R_v = 1, 5, 10$ Mpc. The bottom panel shows the screened fraction averaged from these galaxy realizations. While it is unlikely that the screening radius is much larger than a few megaparsecs, we observe that a significant fraction of the propagation path can be screened, especially for large-redshift sources. We observe that sources with redshift around $z \sim 2, 3$ tend to have the largest fraction of path screened. This is closely connected to the galaxy population model, which peaks around $z \sim 2$ and decreases towards larger redshifts [35]. Since the precise mechanism for graviton mass screening is unknown and the range of the screening effect is subject to much uncertainty [see, e.g., [11, 13, 14, 18]], it is crucial to properly account for the galaxy population for a general treatment.

As is discussed, a key advantage of jointly analyzing the graviton-mass-induced phasing for different GW detection events is to break the degeneracy between screening radius and graviton mass. In this section, we give a heuristic argument to support this claim, and we explicitly show it with Markov Chain Monte Carlo simulations (MCMC) in the following section. As Eqn 5.44 evidently shows, the graviton-mass-induced phase depends only on the product $m_g^2 D_0^{(0)}$, and neither factor shows up in other terms of the waveform. It is thus not possible to disentangle their effects from any individual GW detection event. Thankfully, having events at different redshifts in principle resolves this degeneracy issue. As Fig. 6.2 shows, the average screened fraction of the propagation path varies with GW source redshift, which is a result of the redshift evolution of galaxy population. Varying the screening radius effects the propagation path screened fraction, and the extent of this variation is different depending on GW source redshifts. The graviton mass, however, brings proportional effects to all detection events. In this way, jointly analyzing multiple events breaks the degeneracy between these two parameters. Indeed, with the large expected event numbers and redshift reach in third generation GW detectors, we expect the constraining power to improve dramatically.

6.2 Analysis

In this section we show how the GW events observed by Cosmic Explorer can jointly place constraints on the graviton mass and galaxy screening radius and break parameter degeneracy once the graviton mass signature is detected. In subsection 6.2 a covariance matrix is constructed looking at individual events varying input parameters (masses and redshift). Then in subsection 6.2 the multiple events are combined to give a constraint on R_v and m_g with this covariance matrix. To summarize, we estimate the graviton-mass-induced phasing uncertainty from a Fisher matrix analysis. We then use MCMC simulation to sample the detected population and obtain constraints on graviton mass and screening radius. In the following subsections we provide details on each procedure.

Fisher Estimate

The analysis employs the Fisher matrix approach, where the covariance matrix is the inverse of the Fisher matrix: $\mathbf{\Gamma} = (\partial h/\partial\vec{\vartheta}|\partial h/\partial\vec{\vartheta})$. The parentheses are the noise-weighted inner-product with respect to CE. Here the parameter space is $\vec{\vartheta} = \{\mathcal{M}, \eta, d_L, t_c, \phi_c, \bar{m}_g^2\}$, where,

$$\bar{m}_g^2 = D_0^{(0)}/\lambda_g^2, \tag{6.8}$$

and errors are calculated for $\bar{m}_g^2$. A power-law (Salpeter) distribution for the primary mass m_1 is assumed, which is uniform in m_2. Here m_1 is treated as the primary with $m_1 \in (m_{\min}, m_{\max})$ and $m_2 \in (m_{\min}, m_1)$ where $m_{\min} = 5M_\odot$ and $m_1+m_2 \leq 100M_\odot$. The redshift z is sampled from a uniform comoving volume without a specific star formation rate (SFR) assumed.

Note that in general a GW signal from compact binaries has four angles: extrinsic localization polar and azimuthal angles (θ, ϕ) and instrinsic inclination and polarization angles (ι, ψ). Sky-averaging of the angles can be implemented [36]. Here the angular dependence can be encapsulated in the factor $w(\theta, \phi, \psi, \iota)$. In an optimal configuration $(\theta = 0, \iota = 0)$, with ϕ, ψ chosen so that $w = 1$ (optimal). Assuming an orthogonal detector an angle-averaged value of w is,

$$\langle w(\theta, \phi, \psi, \iota)^2 \rangle = \left(\frac{2}{5}\right)^2. \tag{6.9}$$

With an effectively stationary detector, with respect to the signal duration, the sky-averaged SNR and Fisher matrix is then,

$$\rho_{\rm ave} = \frac{2}{5}\rho_{\rm opt}, \tag{6.10}$$

$$\mathbf{\Gamma}_{\rm ave} = \left(\frac{2}{5}\right)^2 \mathbf{\Gamma}_{\rm opt}, \tag{6.11}$$

in comparison to the optimal $(w = 1)$ configuration. The sky-averaged SNR is restricted to a cutoff of 7 for CE.

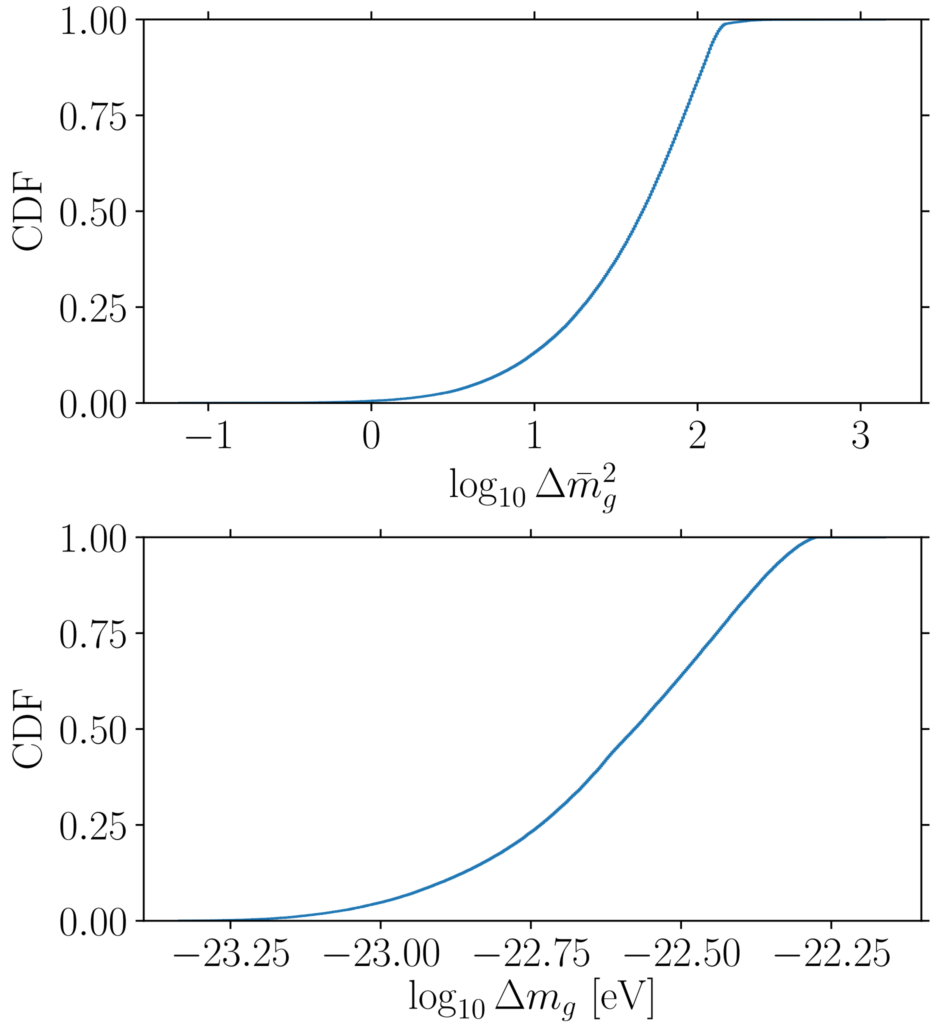

Figure 6.3: Cumulative distribution function (CDF) results of massive graviton error estimates. Top: CDF of error estimates of $\bar{m}_g^2$. Bottom: direct translation to m_g[eV] using the sampled redshift assuming a graviton dispersion of no redshift dependence.

Runs are completed for 5.5×10^4 calculations with median error for $\bar{m}_g^2$ of 46.53, which samples to a maximum redshift of $z = 30$. [3] Performing computations to $\sim 10^6$ runs produces a median error for $\bar{m}_g^2$ of 47.17, where the means and standard deviations also vary at $\sim 1\%$. To perform the MCMC computations in this section for redshift dependence the smaller sampling size is thus used for speed and efficiency. Top panel in Fig. 6.3 are the errors $\Delta\bar{m}_g^2$. The bottom panel is the quick translation to m_g [eV], where for now the sampled z is used to calculate $D_0^{(0)}$ assuming no redshift dependence.

MCMC Constraints

Estimated error for Eq. (6.8) can be used to constrain R_v and the graviton mass, given the covariance matrix constructed for parameter space $\vec{\vartheta} = \{\mathcal{M}, \eta, d_L, t_c, \phi_c, \bar{m}_g^2\}$. In this subsection we describe the MCMC simulation for constraining the galaxy screening radius and the graviton mass. The simulation is implemented using the Python package `emcee` [37]. In each step, we evaluate the log likelihood for the two-parameter hypothesis, defined by the screening radius R_v and the graviton mass, $\log_{10} m_g^2$. We adopt the χ^2 statistic such that the log likelihood is given as,

$$\ln \mathcal{L} = \frac{1}{2}(\mathbf{d} - \mathbf{s})^T \mathbf{C}(\mathbf{d} - \mathbf{s}), \tag{6.12}$$

where $\mathbf{C}$ is the covariance matrix; since we assume that the measurement of different GW events are uncorrelated, $\mathbf{C}$ is diagonal and its diagonal elements are the estimated variance of $\overline{m}_g^2$ from the Fisher matrix calculation. The template vector, $\mathbf{s}$ and the data vector, $\mathbf{d}$ are given as,

$$\begin{aligned} \mathbf{s}(R_v, m_g) &\equiv \{\overline{m}_{g,i}^2 | i = 1, 2, 3, ..., N_{\rm GW}\}, \\ \mathbf{d} &= \mathbf{s}(R_{v,0}, m_{g,0}) + \mathbf{n}, \\ \mathbf{n} &= \{\sigma_{\overline{m}_{g,i}^2} \mathcal{N} | i = 1, 2, 3, ..., N_{\rm GW}\}, \end{aligned} \tag{6.13}$$

where $N_{\rm GW}$ is the number of GW events, $\mathbf{n}$ is the noise vector and $\mathcal{N}$ is drawn from a standard normal distribution. Note that the dependence of $\mathbf{s}$ on the source redshift and galaxy realization is encoded in Eqs. (6.5) and (5.44). The true graviton mass and screening radius is given by $(R_{v,0}, m_{g,0})$. In other words, the log likelihood sums over all events included in the analysis.

Since we do not input real detector noise data, we marginalize over its realizations by resampling the standard normal distribution $\mathcal{N}$ for all events at each step in the

[3] The distribution for z slowly decreases when no SFR is assumed, sampling out to $z = 30$ computes sources with SNR<7 for CE.

MCMC. The template, i.e., induced dephasing for each event sample, is determined by the graviton mass, the screening radius and the particular galaxy realization. Specifically, we generate a galaxy realization and compute the total unscreened path length for a given screening radius via Eqn. 6.5. The $\overline{m}_g^2$ is then calculated using Eqn. 6.8. Since it is unlikely that we have a precise galaxy atlas out to high redshift, we marginalize over the galaxy realization and resample for every GW event at each MCMC step. For each realization, we compute the average number of galaxies within the "tube" screening region connecting the GW source and the observer at each redshift slice. We then populate this region with galaxies via Poisson sampling. The unscreened propagation distance is calculated using Eqn. 6.5.

For simplicity, we adopt flat priors for R_v and $\log_{10} m_g^2$ and limit the range to,

$$0 \leq R_v\ [\mathrm{Mpc}] \leq 15, \ -48 \leq \log_{10} m_g^2\ [\mathrm{eV}^2] \leq -43. \tag{6.14}$$

The upper limit on R_v is chosen such that the propagation path for most sources would be mostly screened, in which case the graviton mass is not able to produce observable phase shifts. The graviton mass prior is set in reference to Ref. [13], where a similar order-of-magnitude constraint is obtained for detection by LISA.

We perform a null-signal test by setting $\mathbf{s}(R_{v,0}, m_{g,0})$ in the data vector to be $\mathbf{0}$, and plot the MCMC sample contours using the Python library `seaborn` [38] in Fig. 6.4. For this test, we simulate the constraining power of 5000 GW events. For computational efficiency, we first randomly draw a population of 200 GW events with redshift $z < 6$. To compensate for the smaller event number, we scale down the phase uncertainty by $\sqrt{5000/200}$ from the Fisher matrix calculation [see, e.g., [39, 40]]. In applying the scaling argument, we assume that these 200 events are representative of the detected population, and additional events would add "similar" information. We observe that the null-signal case mostly rules out the parameter space with large m_g and small R_v, since such parameters lead to large phase shifts. The contour shape highlights the degeneracy that more screen regions can compensate for the increased phase shift per unscreened path length. From this sample, we may read off that the 2σ upper limit on the graviton mass value is roughly $\log_{10} m_g^2 = -46.7$ [eV]^2, given the null graviton mass detection for 5000 GW events up to $z = 6$. As CE is expected to detect $O(10^5)$ events [40, 41], this upper limit can be expected to tighten by a factor of 10.

We then demonstrate that, once the signature of graviton mass is detected, it is possible to estimate both the screening radius and the graviton mass under the framework

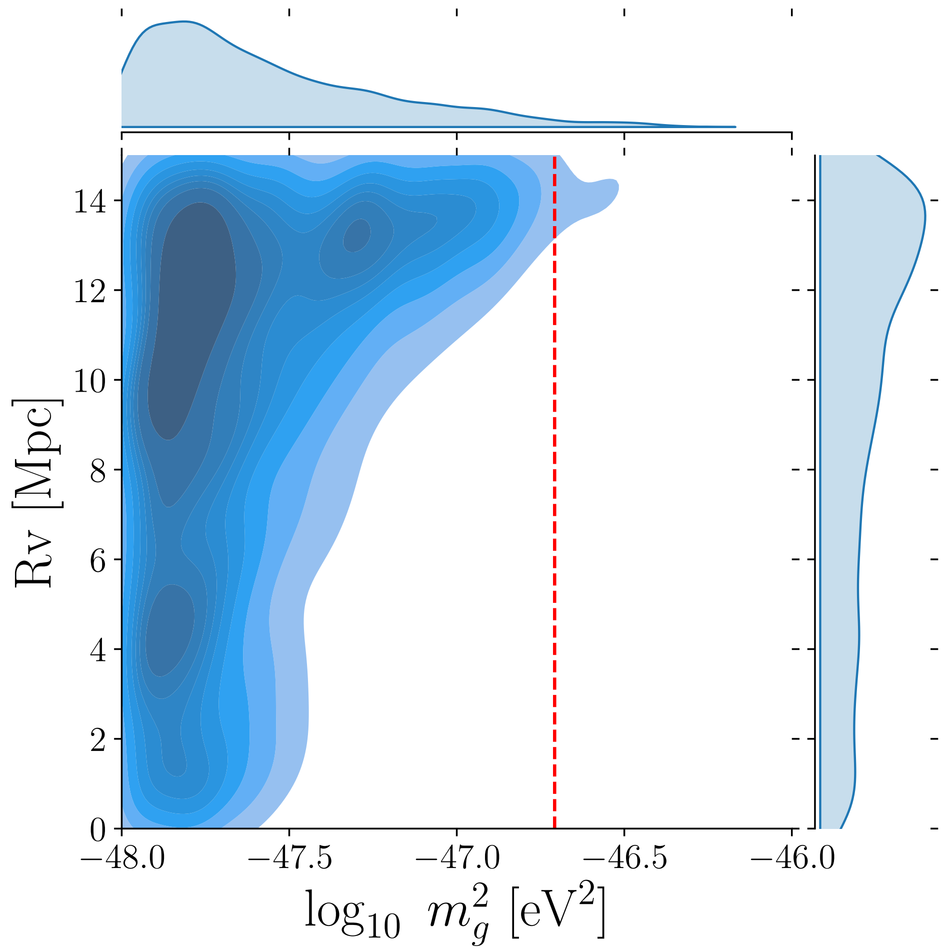

Figure 6.4: MCMC sample contours for null signal. The red line marks the 2σ confidence value at $\log_{10} m_g^2 \approx -46.7$ $[\mathrm{eV}]^2$. As expected, a null signal cannot simultaneously constrain the graviton mass and the screening radius. Nonetheless, the allowed range of screening radius decreases with increasing graviton mass, as expected.

of the multiple galaxy screening model. To this end, we perform a set of injection tests with parameter values $(R_v\ [\mathrm{Mpc}], \log_{10} m_g^2\ [\mathrm{eV}^2]) = (3, -46), (5, -45.5)$ and $(7, -45)$. In each injection run, we randomly draw 150 detection events from the source population and jointly analyze them. For each MCMC step, we resample the galaxy position realization as in the null signal test. The MCMC sample density isoproportion contours are shown in Fig. 6.5; for example, within the largest contour is 90% of the MCMC samples, and the smaller contours represent 60% and 30% respectively.

In the case where $(R_v\ [\mathrm{Mpc}], \log_{10} m_g^2\ [\mathrm{eV}^2]) = (3, -46)$, the induced phase shift is

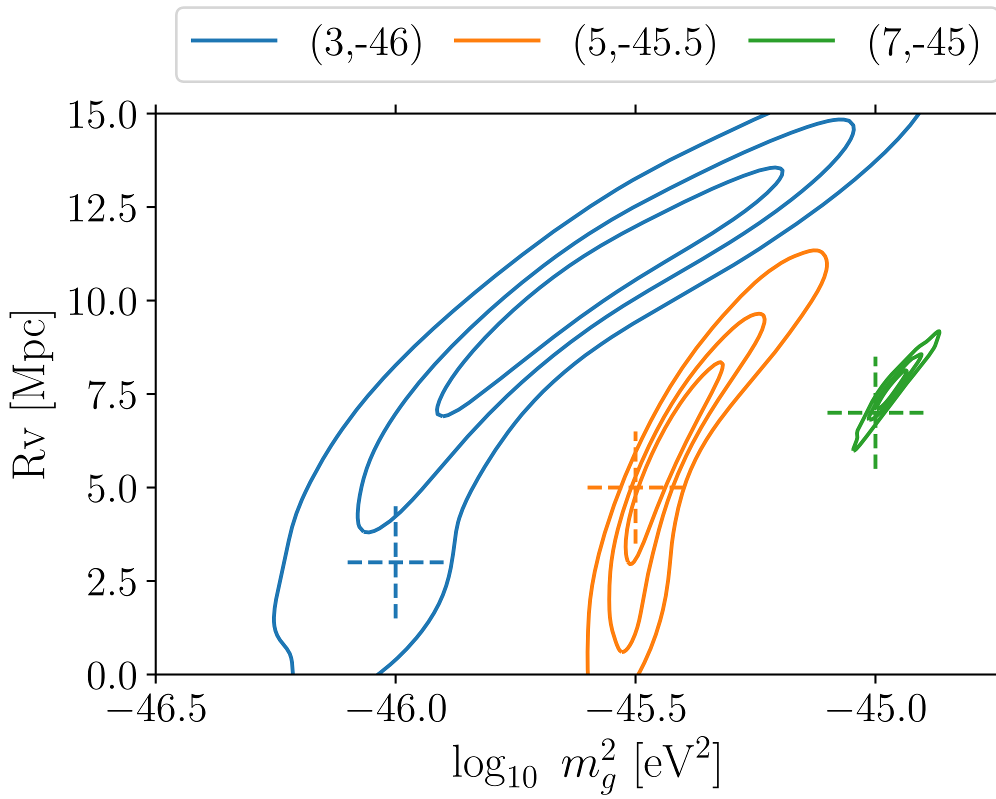

Figure 6.5: MCMC sample contours with injected graviton mass signal. The contours mark isoproportions of the sample density, within which are 90%, 60% and 30% of the samples. The injected signal parameter values (R_v [Mpc], $\log_{10} m_g^2$ [eV^2]) are shown in the legend, and they are marked with dashed crosses in the figure. For each injection test, 150 GW sources were randomly drawn from the population distribution and jointly analyzed.

too small for parameter estimation given the size of the GW source population; we obtain only a joint constraint on R_v and m_g without breaking the degeneracy. With louder signals, we observe that the samples converge to the true value more sharply.

While this population size is smaller than what is expected for CE, it is computationally inexpensive and already suffices to demonstrate that accounting for the multiple screening galaxy model gives simultaneous constraints on graviton mass and galaxy screening. With $O(10^5)$ events, we expect that the uncertainty reduces by $O(10)$ from the same scaling argument as before.

6.3 Discussion

A characterization of a newly derived dispersion relation is presented using a phase velocity approach. Constraints on the graviton mass incorporating a screening model, based on current galaxy models, is placed. In particular, we account for the possibility that the graviton propagation path is screened by multiple galaxies. This is performed by incorporating realistic galaxy population models in the screening templates. For this proof-of-concept study we adopt several simplifying assumptions. In this section we discuss each premise and the potential impact of more sophisticated modeling.

First, the underlying analysis relied on the Fisher matrix approach, which is a lower-bound estimator with higher-order contributions in the error appearing in low-SNR events [42]. A specific star formation rate was not assumed which gives high-redshift GW signals that resulted in a median SNR of 26 for CE with a power-law mass distribution (42 for a log-uniform mass distribution). Specific formation rates for particular galaxy models will lead to signals peaking at lower redshifts, boosting the median SNR. As a trade-off to higher SNRs at a lower redshift the extent of dephasing will also be impacted given a shorter propagation path, so the low-SNR study encapsulates possible offsets. A full study of the second-order contributions to the error estimate is beyond the scope of this study and can be better addressed through other analysis techniques. Directional dependence is also essential in both the SNR and galaxy distributions a GW will propagate through. The sky-averaged model considered here can also be further expanded on, but for the purposes of demonstrating screening with realistic galaxy distributions the method is sufficient.

Although the screening model implemented is able to demonstrate the multiple-galaxy screening effect, it can be elaborated on in order to give more accurate predictions. This calls for specific massive graviton theories to be further developed in dynamical spacetimes and conditions of the Vainshtein screening process manifesting in GW propagation, similar to scalar radiation [21]. Here we assumed that the screening radius is galaxy independent. Since there is yet to be a strongly preferred theoretical model for graviton mass screening, this simplest model is sufficient for qualitatively characterizing the main effects. Depending on specific theory requirements, it is straightforward to change the fixed R_v into, for example, a parameterized function. Furthermore, the current screening model is a top-hat filter. In reality, it is possible that the graviton mass screening is connected to properties of the galaxy and does not have a sharply defined border. To reflect such dependence, it is neccessary to consider a screening profile, as well as possible effects on the GW when it passes through the screened region.

Finally, the galaxy population modeling can be enhanced by incorporating spatial galaxy distribution power spectrum [see, e.g., [43–45]]. In the isotropic model, the spread of screened fraction for GW sources at the same redshift can be largely attributed to Poissonian shot noise on the number of intervening galaxies. If we could measure the statistical fluctuation of the screened fraction for sources at various redshifts, the excess power beyond shot noise could indicate the galaxy distribution power spectrum at the scale of the screening radius. Conceptually, it is similar to the study in Ref.[46–48], in which GW detection provides a unique probing opportunity to the background cosmological environment. While we expect the galaxy clustering around the screening scale to be small, the expected large number of high SNR events for the third generation GW detector might allow for such precise constraints [see, e.g., [40, 49]]. We defer the aforementioned improvements to future studies.

References

[1] B. P. Abbott *et al.* (LIGO Scientific Collaboration and Virgo Collaboration), PRL **123**, 011102, `10.1103/PhysRevLett.123.011102` (2019).

[2] B. P. Abbott *et al.* (LIGO Collaboration) (LIGO Scientific Collaboration and Virgo Collaboration), PRD **100**, 104036, `10.1103/PhysRevD.100.104036` (2019).

[3] B. P. Abbott *et al.* (LIGO Collaboration) (LIGO Scientific Collaboration and Virgo Collaboration), PRD **103**, 122002, `10.1103/PhysRevD.103.122002` (2021).

[4] B. P. Abbott *et al.* (LIGO Collaboration), arXiv e-prints, arXiv:2112.06861 (2021).

[5] B. P. Abbott *et al.* (LIGO Collaboration) (LIGO Scientific Collaboration and Virgo Collaboration), PRX **9**, 031040, `10.1103/PhysRevX.9.031040` (2019).

[6] B. P. Abbott *et al.* (LIGO Scientific Collaboration and Virgo Collaboration), PRX **11**, 021053, `10.1103/PhysRevX.11.021053` (2021).

[7] B. P. Abbott *et al.* (LIGO Collaboration) (LIGO Scientific Collaboration and Virgo Collaboration), ApJL **915**, L5, `10.3847/2041-8213/ac082e` (2021).

[8] B. P. Abbott *et al.* (LIGO and Virgo Scientific Collaboration), arXiv e-prints, arXiv:2108.01045 (2021).

[9] B. P. Abbott *et al.* (LIGO Scientific Collaboration and Virgo Collaboration), CQG **34**, 044001, `10.1088/1361-6382/aa51f4` (2017).

[10] C. M. Will, LRR **17**, 4, `10.12942/lrr-2014-4` (2014).

[11] C. de Rham, LRR **17**, 7, `10.12942/lrr-2014-7` (2014).

[12] C. M. Will, CQG **35**, 17LT01, `10.1088/1361-6382/aad13c` (2018).

[13] C. M. Will, PRD **57**, 2061–2068 (1998).

[14] S. Mirshekari, N. Yunes, and C. M. Will, PRD **85**, 024041, 10.1103/PhysRevD.85.024041 (2012).

[15] A. Riazuelo and J.-P. Uzan, PRD **62**, 083506, 10.1103/PhysRevD.62.083506 (2000).

[16] I. D. Saltas, I. Sawicki, L. Amendola, and M. Kunz, PRL **113**, 191101, 10.1103/PhysRevLett.113.191101 (2014).

[17] A. Nishizawa, PRD **97**, 104037, 10.1103/PhysRevD.97.104037 (2018).

[18] S. Perkins and N. Yunes, CQG **36**, 055013, 10.1088/1361-6382/aafce6 (2019).

[19] J. M. Ezquiaga, W. Hu, M. Lagos, and M.-X. Lin, JCAP **2021**, 048, 10.1088/1475-7516/2021/11/048 (2021).

[20] K. Hinterbichler, Reviews of Modern Physics **84**, 671–710 (2012).

[21] F. Dar, C. de Rham, J. Tate Deskins, J. Giblin John T., and A. J. Tolley, CQG **36**, 025008, 10.1088/1361-6382/aaf5e8 (2019).

[22] E. Babichev and C. Deffayet, CQG **30**, 184001, 10.1088/0264-9381/30/18/184001 (2013).

[23] A. I. Vainshtein, Physics Letters B **39**, 393–394 (1972).

[24] D. Reitze, R. X. Adhikari, S. Ballmer, B. Barish, L. Barsotti, G. Billingsley, D. A. Brown, Y. Chen, D. Coyne, R. Eisenstein, M. Evans, P. Fritschel, E. D. Hall, A. Lazzarini, G. Lovelace, J. Read, B. S. Sathyaprakash, D. Shoemaker, J. Smith, C. Torrie, S. Vitale, R. Weiss, C. Wipf, and M. Zucker, in Bulletin of the american astronomical society, Vol. 51 (Sept. 2019).

[25] O. Doré, J. Bock, M. Ashby, P. Capak, A. Cooray, R. de Putter, T. Eifler, N. Flagey, Y. Gong, S. Habib, K. Heitmann, C. Hirata, W.-S. Jeong, R. Katti, P. Korngut, E. Krause, D.-H. Lee, D. Masters, P. Mauskopf, G. Melnick, B. Mennesson, H. Nguyen, K. Öberg, A. Pullen, A. Raccanelli, R. Smith, Y.-S. Song, V. Tolls, S. Unwin, T. Venumadhav, M. Viero, M. Werner, and M. Zemcov, arXiv e-prints, arXiv:1412.4872 (2014).

[26] W. Percival, M. Balogh, D. Bond, J. Bovy, R. Carlberg, S. Chapman, P. Cote, N. Cowan, S. Fabbro, L. Ferrarese, S. Gwyn, R. Hlozek, M. Hudson, J. Hutchings, J. Kavelaars, D. Lang, A. McConnachie, A. Muzzin, L. Parker, C. Pritchet, M. Sawicki, D. Schade, D. Scott, K. Smith, K. Spekkens, J. Taylor, and C. Willott, in Canadian long range plan for astronomy and astrophysics white papers, Vol. 2020 (Oct. 2019).

[27] J. Rhodes, D. Alonso, B. Ansarinejad, R. Armstrong, J. Asorey, A. Avelino, J. Blazek, F. J. Castander, R. R. Chary, X. Chen, A. Choi, D. Clowe, J. Cohen-Tanugi, J. Comparat, R. A. C. Croft, O. Doré, S. Escoffier, R. Foley, P. Fosalba, D. Gruen, N. Gupta, L. Guzzo, A. J. Hawken, S. Hemmati, K. Heitmann, L. Hernquist, C. Heymans, C. M. Hirata, H. Hoekstra, D. Huterer, I. T. Iliev, B. Jain, S. W. Jha, R. E. Keeley, A. Kiessling, T. Kitching, A. Koekemoer, S. M. Koushiappas, E. D. Kovetz, J. Kruk, B. L'Huillier, O. Lahav, P. Lemos, A. d. l. Macorra, A. P. Malagón, R. Mandelbaum, D. Masters, M. McQuinn, P. Melchior, H. Miyatake, J. A. Newman, R. Nichol, G. Niz, P. O'Connor, M. Penna-Lima, W. J. Percival, S. Perlmutter, A. Pisani, M. Rigault, G. Rossi, M. Schmittfull, R. Schuhmann, D. Scolnic, M. Sereno, H. Shan, M. Shirasaki, S. Simon, A. Slosar, D. Spergel, S. Sridhar, M. Takada, M. A. Troxel, Y. Wang, D. Weinberg, N. Yoshida, Y. Zhang, and LSST Dark Energy Science Collaboration, BAAS **51**, 201 (2019).

[28] J.-Z. Qi, S.-J. Jin, X.-L. Fan, J.-F. Zhang, and X. Zhang, arXiv e-prints, arXiv:2102.01292 (2021).

[29] H. A. Winther and P. G. Ferreira, PRD **92**, 064005, `10.1103/PhysRevD.92.064005` (2015).

[30] B. Li, G.-B. Zhao, and K. Koyama, JCAP **2013**, 023, `10.1088/1475-7516/2013/05/023` (2013).

[31] F. Schmidt, PRD **81**, 103002, `10.1103/PhysRevD.81.103002` (2010).

[32] B. Falck, K. Koyama, and G.-B. Zhao, JCAP **2015**, 049, `10.1088/1475-7516/2015/07/049` (2015).

[33] D. W. Hogg, arXiv e-prints, astro-ph/9905116, astro–ph/9905116 (1999).

[34] Y.-Y. Choi, C. Park, and M. S. Vogeley, ApJ **658**, 884–897 (2007).

[35] P. Torrey, S. Wellons, F. Machado, B. Griffen, D. Nelson, V. Rodriguez-Gomez, R. McKinnon, A. Pillepich, C.-P. Ma, M. Vogelsberger, V. Springel, and L. Hernquist, MNRAS **454**, 2770–2786 (2015).

[36] B. S. Sathyaprakash and B. F. Schutz, LRR **12**, 2, `10.12942/lrr-2009-2` (2009).

[37] D. Foreman-Mackey, A. Conley, W. Meierjurgen Farr, D. W. Hogg, D. Lang, P. Marshall, A. Price-Whelan, J. Sanders, and J. Zuntz, *emcee: The MCMC Hammer*, Mar. 2013.

[38] M. Waskom, The Journal of Open Source Software **6**, 3021, `10.21105/joss.03021` (2021).

[39] C. J. Moore, D. P. Mihaylov, A. Lasenby, and G. Gilmore, PRL **119**, 261102, `10.1103/PhysRevLett.119.261102` (2017).

[40] Y. Wang, K. Pardo, T.-C. Chang, and O. Doré, PRD **103**, 084007, `10.1103/PhysRevD.103.084007` (2021).

[41] F. Xu, J. M. Ezquiaga, and D. E. Holz, arXiv e-prints, arXiv:2105.14390 (2021).

[42] R. Tso and M. Zanolin, PRD **93**, 124033, `10.1103/PhysRevD.93.124033` (2016).

[43] L. Legrand, C. Hernández-Monteagudo, M. Douspis, N. Aghanim, and R. E. Angulo, A&A **646**, A109, `10.1051/0004-6361/202039049` (2021).

[44] A. Nicola, D. Alonso, J. Sánchez, A. Slosar, H. Awan, A. Broussard, J. Dunkley, E. Gawiser, Z. Gomes, R. Mandelbaum, H. Miyatake, J. A. Newman, I. Sevilla-Noarbe, S. Skinner, and E. L. Wagoner, JCAP **2020**, 044, `10.1088/1475-7516/2020/03/044` (2020).

[45] M. Tegmark, A. J. S. Hamilton, and Y. Xu, MNRAS **335**, 887–908 (2002).

[46] H. G. Choi, C. Park, and S. Jung, PRD **104**, 063001, `10.1103/PhysRevD.104.063001` (2021).

[47] M. Inamori and T. Suyama, ApJL **918**, L30, `10.3847/2041-8213/ac2142` (2021).

[48] A. Sonnenfeld and M. Cautun, A&A **651**, A18, `10.1051/0004-6361/202140549` (2021).

[49] L. Yang, S. Wu, K. Liao, X. Ding, Z. You, Z. Cao, M. Biesiada, and Z.-H. Zhu, MNRAS **509**, 3772–3778 (2022).

Chapter 7

CONCLUSION

This thesis explores methods to probe fundamental features of gravitational waves (GWs) across its spectrum and propagation. GR has passed all tests to date. The theory holds true in both slow-moving, weak-field regimes and the dynamical, strong-field regime. Work accomplished in thesis has aimed to develop new precision tests of GR with GWs. Below summarizes results obtained and includes references to published results.

7.1 Summary

The analysis method in this work relies heavily on the Fisher information matrix approach. So, in Ch. 3 an extended analysis taking into account higher-order asymptotic contributions to error estimation of low-SNR GW transients was performed using the ppE framework [1, 2]. This work quantified the limitation of the Fisher information approach. A subset of the analysis considered GW dispersion due to non-GR effects for the inspiral of black hole and neutron star binaries.

Leveraging signals spanning the GW spectrum Ch. 4 uses the predictive power of the very early inspiral of a stellar-mass black hole binary, detectable in LISA's frequency range, to actively optimize ground-based detectors to enhance tests of GR [3]. Further work on rates assessments of GW events in the millihertz, decihertz, and kilohertz range was accomplished at the Kavli Summer Program in Astrophysics (results are unpublished). A current publication is being prepared that explores prospects of testing GR with a newly proposed decihertz detector called TianGO. This will add to the mission of multi-band GW astronomy. Both results are discussed in Ch. 1 and 2.

To assess propagation, Ch. 5 explores a model that was developed taking into account anisotropic Lorentz-violating coefficients with an initial assessment of polarization dynamics [4]. Select parameterized models were implemented in LIGO's existing testing GR infrastructure for consideration in a method's paper for future analysis. Further developments, e.g., reduced order modeling, were deemed necessary to perform parameter estimation within a reasonable timescale. Additional work in propagation tests performed the first testing GR analysis of a binary NS event [5]. I performed initial assessment with members of the LIGO Scientific Collaboration to determine if higher-order contributions to tests of Lorentz invariance were feasible within electromagnetic-GW comparison tests. The lack of information for the frequency at peak GW energy emission (or "peak frequency") caused results to be inconclusive. Remaining work concentrated on the paper writing process.

Finally, Ch. 6 investigated potential massive graviton modifications to the GW dispersion relation as a function of redshift and sky-location, which also takes into account the Vainshtein screening mechanism. This mechanism screens the effects of a massive graviton, as predicted in certain beyond-GR theories [6, 7]. These theories agree with GR when tested at local scales within matter distributions, such as galaxies, thus satisfying solar system constraints. At larger scales, and outside matter distributions, modifications are introduced in the propagation of GWs. Therefore, as a GW propagates from its source to us, beyond-GR effects will be suppressed as the wave travels inside the host galaxy, the observer galaxy, and every galaxy in between. Previous work on this topic either neglected this screening effect completely [8], or modeled only the host and the observer galaxy (effectively filtering the signal with Heaviside functions) [9]. Our approach is different because it accounts for all intervening galaxies between the host and the detector using next generation optical surveys [see, e.g., [10–12]], which allows us to break degeneracies between the screening radius and graviton mass. Further enhancements in this galaxy population model can also incorporate spatial galaxy distribution power spectrum [see, e.g., [13–15]]. This work is currently in the process of being published.

7.2 Future Work

Although work on the massive graviton Vainshtein screening mechanism is a big step forward, the approach currently misses theory-specific features that will play a role in observations. Further work can be performed to extend the approach to include transition stiffness and the distribution of galaxies in the Universe. In particular, one can use analytical and numerical methods to extend the top-hat filtering process to account for the curvature of the transition between a screened and an unscreened region of spacetime. Despite progress made in this area, there remains much work to be done [16–18]. The transition stiffness depends on the specific theory of gravity considered, a study of a few examples can be performed in, e.g., massive gravity and bigravity [7, 19]. Furthermore, one can model the number and type of galaxies in between a GW source and Earth through curvature distributions derived from cosmic web structures over large distances making use of the vast number of sources [20, 21]. Such a study will lead to the objective of investigating the screening process outside spherical symmetry. The Vainshtein mechanism has been worked out in detail for only static and spherically symmetric spacetimes [7], but binary BH mergers are dynamical and not spherically symmetric. Future work can extend the study of screening to more generic spacetime backgrounds. This extension involves numerical techniques at investigating spatial and temporal dependence of the screening process. Computing resources in semi-analytical and numerical relativity are well suited to address this objective.

Using models of non-spherically symmetric screening, N-body developments [22], and analytic calculations, a model can be created to fully encapsulate the screening stiffness and cosmic structure of screening regions. This idea leads to a need to parameterize screening mechanisms in beyond-GR theories. Ultimately the parameterized model will be theory dependent, so recipes to generate parameterized models for classes of theories can be laid out. These efforts are important as advanced GW detectors are upgraded to their expected, final design sensitivity, and as they push even beyond that sensitivity in the route toward third-generation detectors. Given a particular modified theory, such as massive gravity [7], a transition stiffness can be determined for a galaxy cluster, and obtain a screening distribution of the galaxies, which will enable many further studies. With this process developed, a mapping to the ppE framework with the screening ("top-hat" filter) model currently being prepared for publication will lay the foundations to develop testing strategies to test the Vainshtein mechanism. As groups prepare for the inaugural observation run of Cosmic Explorer [23], a testing strategy with newly developed analysis techniques can be initiated. This will lay the foundation of probing screening mechanisms with next-generation detectors in the era of precision tests of GR.

References

[1] R. Tso and M. Zanolin, PRD **93**, 124033, `10.1103/PhysRevD.93.124033` (2016).

[2] N. Yunes and F. Pretorius, PRD **80**, 122003, `10.1103/PhysRevD.80.122003` (2009).

[3] R. Tso, D. Gerosa, and Y. Chen, PRD **99**, 124043, `10.1103/PhysRevD.99.124043` (2019).

[4] R. Tso, M. Isi, Y. Chen, and L. Stein, arXiv e-prints, arXiv:1608.01284 (2016).

[5] B. P. Abbott *et al.* (LIGO Scientific Collaboration and Virgo Collaboration), PRL **123**, 011102, `10.1103/PhysRevLett.123.011102` (2019).

[6] A. I. Vainshtein, PLB **39**, 393–394 (1972).

[7] C. de Rham, LRR **17**, 7, `10.12942/lrr-2014-7` (2014).

[8] C. M. Will, LRR **17**, 4, `10.12942/lrr-2014-4` (2014).

[9] S. Perkins and N. Yunes, CQG **36**, 055013, `10.1088/1361-6382/aafce6` (2019).

[10] O. Doré, J. Bock, M. Ashby, P. Capak, A. Cooray, R. de Putter, T. Eifler, N. Flagey, Y. Gong, S. Habib, K. Heitmann, C. Hirata, W.-S. Jeong, R. Katti, P. Korngut, E. Krause, D.-H. Lee, D. Masters, P. Mauskopf, G. Melnick, B. Mennesson, H. Nguyen, K. Öberg, A. Pullen, A. Raccanelli, R. Smith, Y.-S. Song, V. Tolls, S. Unwin, T. Venumadhav, M. Viero, M. Werner, and M. Zemcov, arXiv e-prints, arXiv:1412.4872 (2014).

[11] W. Percival, M. Balogh, D. Bond, J. Bovy, R. Carlberg, S. Chapman, P. Cote, N. Cowan, S. Fabbro, L. Ferrarese, S. Gwyn, R. Hlozek, M. Hudson, J. Hutchings, J. Kavelaars, D. Lang, A. McConnachie, A. Muzzin, L. Parker, C. Pritchet, M. Sawicki, D. Schade, D. Scott, K. Smith, K. Spekkens, J. Taylor, and C. Willott, in Canadian long range plan for astronomy and astrophysics white papers, Vol. 2020 (Oct. 2019).

[12] J. Rhodes, D. Alonso, B. Ansarinejad, R. Armstrong, J. Asorey, A. Avelino, J. Blazek, F. J. Castander, R. R. Chary, X. Chen, A. Choi, D. Clowe, J. Cohen-Tanugi, J. Comparat, R. A. C. Croft, O. Doré, S. Escoffier, R. Foley, P. Fosalba, D. Gruen, N. Gupta, L. Guzzo, A. J. Hawken, S. Hemmati, K. Heitmann, L. Hernquist, C. Heymans, C. M. Hirata, H. Hoekstra, D. Huterer, I. T. Iliev, B. Jain, S. W. Jha, R. E. Keeley, A. Kiessling, T. Kitching, A. Koekemoer, S. M. Koushiappas, E. D. Kovetz, J. Kruk, B. L'Huillier, O. Lahav, P. Lemos, A. d. l. Macorra, A. P. Malagón, R. Mandelbaum, D. Masters, M. McQuinn, P. Melchior, H. Miyatake, J. A. Newman, R. Nichol, G. Niz, P. O'Connor, M. Penna-Lima, W. J. Percival, S. Perlmutter, A. Pisani, M. Rigault, G. Rossi, M. Schmittfull, R. Schuhmann, D. Scolnic, M. Sereno, H. Shan, M. Shirasaki, S. Simon, A. Slosar, D. Spergel, S. Sridhar, M. Takada, M. A. Troxel, Y. Wang, D. Weinberg, N. Yoshida, Y. Zhang, and LSST Dark Energy Science Collaboration, BAAS **51**, 201 (2019).

[13] L. Legrand, C. Hernández-Monteagudo, M. Douspis, N. Aghanim, and R. E. Angulo, A&A **646**, A109, `10.1051/0004-6361/202039049` (2021).

[14] A. Nicola, D. Alonso, J. Sánchez, A. Slosar, H. Awan, A. Broussard, J. Dunkley, E. Gawiser, Z. Gomes, R. Mandelbaum, H. Miyatake, J. A. Newman, I. Sevilla-Noarbe, S. Skinner, and E. L. Wagoner, JCAP **2020**, 044, `10.1088/1475-7516/2020/03/044` (2020).

[15] M. Tegmark, A. J. S. Hamilton, and Y. Xu, MNRAS **335**, 887–908 (2002).

[16] H. A. Winther and P. G. Ferreira, PRD **92**, 064005, `10.1103/PhysRevD.92.064005` (2015).

[17] B. Li, G.-B. Zhao, and K. Koyama, JCAP **2013**, 023, `10.1088/1475-7516/2013/05/023` (2013).

[18] F. Schmidt, PRD **81**, 103002, `10.1103/PhysRevD.81.103002` (2010).

[19] E. Babichev and C. Deffayet, CQG **30**, 184001, `10.1088/0264-9381/30/18/184001` (2013).

[20] Y. Wang, K. Pardo, T.-C. Chang, and O. Doré, PRD **103**, 084007, `10.1103/PhysRevD.103.084007` (2021).

[21] F. Xu, J. M. Ezquiaga, and D. E. Holz, arXiv e-prints, arXiv:2105.14390 (2021).

[22] H. A. Winther, F. Schmidt, A. Barreira, C. Arnold, S. Bose, C. Llinares, M. Baldi, B. Falck, W. A. Hellwing, K. Koyama, B. Li, D. F. Mota, E. Puchwein, R. E. Smith, and G.-B. Zhao, MNRAS **454**, 4208–4234 (2015).

[23] D. Reitze, R. X. Adhikari, S. Ballmer, B. Barish, L. Barsotti, G. Billingsley, D. A. Brown, Y. Chen, D. Coyne, R. Eisenstein, M. Evans, P. Fritschel, E. D. Hall, A. Lazzarini, G. Lovelace, J. Read, B. S. Sathyaprakash, D. Shoemaker, J. Smith, C. Torrie, S. Vitale, R. Weiss, C. Wipf, and M. Zucker, in Bulletin of the american astronomical society, Vol. 51 (Sept. 2019).